



# Master Thesis

**Extended Higgs sector explored at a Muon Collider**

carried out under the supervision of

Univ.Lektor Dipl.-Ing. Dr.techn. Helmut Eberl
and
Univ.Prof. Dipl.-Phys. Dr.rer.nat. Jochen Schieck

Institute for High Energy Physics
Austrian Academy of Sciences
and
Vienna University of Technology

for the academic degree of

**'Diplom-Ingenieur/in'**

as part of the studies

**'Masterstudium Technische Physik - 066 461'**

by

**Leonardo Bellinato Giacomelli BSc**
Matr. nr. 11734021

23. August 2023

**Author** _____ **Supervisor** _____
*(signature)* *(signature)*

**Affidavit**

I declare that I have authored this thesis independently, that I have not used other than the declared sources/resources, and that I have explicitly indicated all material which has been quoted either literally or by content from the sources used. The text document uploaded to TISS (TU Wien) is identical to the present master‘s thesis.

23. August 2023

**Author** _____

*(signature)*

*'Misurate ciò che è misurabile e rendete misurabile ciò che non lo è'*

Galileo Galilei[1]

[1]Translation: 'Measure what is measurable, and make measurable what is not.' [1]

**Abstract**

In this work we explore the phenomenology of various non-supersymmetric Two Higgs Doublet Models (THDM) with real input parameters for a future Muon Collider. In particular we study Type-I, Type-II, lepton-specific and flipped THDMs by investigating resonances caused by the neutral Higgs bosons $H^0$ and $A^0$, taking $h^0$ as the discovered Higgs boson at LHC in 2012. In contrast to an $e^+e^-$ collider, the large muon Yukawa coupling enables an efficient s-channel neutral Higgs boson exchange. Therefore, we calculate and study in detail the total cross section for the production processes $\mu^-\mu^+ \to t\bar{t}$, $\mu^-\mu^+ \to b\bar{b}$, $\mu^-\mu^+ \to \tau^-\tau^+$, and $\mu^-\mu^+ \to h^0h^0$ as a function of the THDM input parameters $m_{H^0}, m_{A^0}, m_{H^\pm}, \tan\beta, \sin\alpha, \lambda_5$. We further calculate all $H^0$ and $A^0$ tree-level decay widths in order to get the relevant branching ratios (BR) and also the total widths necessary for the Breit-Wigner propagators of $H^0$ and $A^0$. In this study we consider all theoretical bounds, e.g. unitarity, global minimum, vacuum stability and oblique parameters bounds, as well as all relevant experimental bounds. We derive the theoretical bounds from first principles and then perform a systematic numerical scan to find allowed parameter sets. With these sets we perform a detailed numerical study of the $H^0$ and $A^0$ resonances in the production processes $\mu^-\mu^+ \to t\bar{t}, b\bar{b}, \tau^-\tau^+, h^0h^0$ and discuss the results.

## Zusammenfassung

In dieser Arbeit untersuchen wir die Phänomenologie verschiedener nicht-supersymmetrischer Two Higgs Doublet Models (THDM) mit reellen Eingabeparametern für einen zukünftigen Müon-Beschleuniger. Insbesondere erforschen wir die Typ-I-, Typ-II-, leptonenspezifischen und flipped THDMs, wobei wir annehmen, dass $h^0$ das am LHC 2012 entdeckte Higgs Boson ist. Im Gegensatz zu einem $e^+e^-$-Beschleuniger ermöglicht die große Müon-Yukawakopplung einen effizienten S-Kanal Austausch von neutralen Higgs Bosonen. Daher berechnen und untersuchen wir im Detail den totalen Wirkungsquerschnitt für die Produktionsprozesse $\mu^-\mu^+ \to t\bar{t}$, $\mu^-\mu^+ \to b\bar{b}$, $\mu^-\mu^+ \to \tau^-\tau^+$ und $\mu^-\mu^+ \to h^0h^0$ als Funktion der THDM Eingabeparameter $m_{H^0}, m_{A^0}, m_{H^\pm}, \tan\beta, \sin\alpha, \lambda_5$. Des Weiteren berechnen wir alle $H^0$- und $A^0$-Zerfallsbreiten auf tree-level, um die relevanten branching ratios (BR) sowie die für die Breit-Wigner Propagatoren von $H^0$ und $A^0$ erforderlichen Gesamtbreiten zu erhalten. In unserer Studie berücksichtigen wir alle theoretischen Grenzen, wie Unitarität, globales Minimum, Vakuumstabilität und Oblique Parametergrenzen, sowie alle relevanten experimentellen Grenzen. Wir leiten die theoretischen Grenzen von Grund auf her und führen dann einen systematischen numerischen Scan durch, um erlaubte Parameterpunkte zu finden. Mit diesen Parametern führen wir dann eine detaillierte numerische Untersuchung der $H^0$- und $A^0$-Resonanzen in den Produktionsprozessen $\mu^-\mu^+ \to t\bar{t}, b\bar{b}, \tau^-\tau^+, h^0h^0$ durch und diskutieren die erhaltenen Ergebnisse.

# Contents

# LIST OF ABBREVIATIONS

**SM** Standard Model of particle physics

**THDM** Two Higgs Doublet Model

**FCNC** Flavor changing neutral currents

**EV** Eigenvalues

$t_\beta = \tan(\beta)$

$s_\beta = \sin(\beta)$

$c_\beta = \cos(\beta)$

$s_{\beta-\alpha} = \sin(\beta - \alpha)$

$c_{\beta-\alpha} = \cos(\beta - \alpha)$

$s_{2\beta} = \sin(2\beta)$

$c_{2\beta} = \cos(2\beta)$

$\lambda_{ijk} = \lambda_i + \lambda_j + \lambda_k$

$\lambda_{ij}^{\pm} = \lambda_i \pm \lambda_j$

$s_w = \sin(\theta_W)$ (Weinberg angle)

$c_w = \cos(\theta_W)$ (Weinberg angle)

$\bar{s}_w = \sin(\theta_W)(m_{Z^0})$

$\bar{c}_w = \cos(\theta_W)(m_{Z^0})$

$\bar{\alpha} = \frac{\bar{g}^2 \bar{s_Z}^2}{4\pi}$

We note that in the literature multiple notations are used for the Higgs doublets. In this work we use two different notations based on the notation used in the corresponding literature. We identify: $\phi_i^{\pm} \equiv \omega_i^{\pm}$, $\phi_i \equiv h_i$ and $a_i \equiv z_i$.

# Introduction

Muon colliders (MC) have emerged as a promising avenue in the quest for advancing particle physics research. The exceptional properties of muons, such as their higher mass and reduced synchrotron radiation, make them attractive candidates for constructing a new generation of high-energy colliders [2–5]. This thesis delves into the intriguing prospect of constructing a Muon Collider and its specific relevance in the context of THDMs. As an extension of the Standard Model, THDMs introduce an additional Higgs doublet, enriching the particle landscape with four additional scalar Higgs bosons $H^0$, $A^0$ and $H^\pm$. With the potential to achieve higher energies and luminosities, a Muon Collider becomes a powerful tool to study the properties and interactions of additional Higgs bosons, providing crucial insights into the nature of particle masses and the electroweak symmetry breaking mechanism. By exploring the unique capabilities of Muon Colliders in the context of THDMs, this research contributes to the pursuit of new frontiers in particle physics and potential avenues for discovering new physics phenomena.

Similar studies have been published on the resonant behavior of heavy Higgs bosons in the context of a future Muon Collider. However, they are all in the context of supersymmetric models. E.g. in [6] the pair production of stops, sbottoms, staus and tau-sneutrinos at a MC is discussed. In particular, the authors investigate the sfermion production near $\sqrt{S} = m_{H^0}$ and $\sqrt{S} = m_{A^0}$, within the Minimal Supersymmetric Standard Model. Furthermore, in [7] the authors show that a MC would be ideally suited for the study of the heavy $H^0$ and $A^0$ Higgs bosons. They argue that this is because of the large muon Yukawa coupling and a width-to-mass ratio far larger than the expected Muon Collider beam-energy resolution. This study is within a representative Natural Supersymmetry model. Even though, similarly to this work, these studies explore the resonant behavior of the $H^0$ and $A^0$ Higgs bosons at a MC, no detailed study has been published on the resonant behavior of the heavy neutral Higgs bosons within the THDM and more broadly within the four specific THDMs that we consider.

In this work we explore the research potential of such a MC in the context of various non-supersymmetric Two Higgs Doublet Models (THDM) with real input parameters. In particular we study the Type-I, Type-II, lepton-specific and flipped THDMs. We do so by investigating resonances caused by the $H^0$ and $A^0$ neutral Higgs bosons. Moreover, throughout the work we assume that the $h^0$ Higgs boson, is the Higgs boson discovered at the LHC (CERN) in 2012. Differently to an $e^+e^-$ collider, a Muon Collider enables an efficient s-channel neutral Higgs boson exchange. This is due to the large muon Yukawa coupling. Therefore, we study in detail the total cross section for the production processes

$\mu^-\mu^+ \to t\bar{t}$, $\mu^-\mu^+ \to b\bar{b}$, $\mu^-\mu^+ \to \tau^-\tau^+$, and $\mu^-\mu^+ \to h^0h^0$ as a function of the THDM input parameters $m_{H^0}, m_{A^0}, m_{H^\pm}, \tan\beta, \sin\alpha, \lambda_5$. We derive the matrix elements for the various channels and then analytically integrate them with the help of *Mathematica*. Moreover, we check the results with the *FeynArts* (FA) and *FormCalc* (FC) packages [8, 9]. We choose various production channels because the different parameter sets allowed by all theoretical and experimental bounds, produce resonances which might only be detectable in a specific channel. Moreover, the different models have different Yukawa couplings to the Higgs bosons, and thus produce resonances which might only be observed in a specific model for a certain parameter set.

Furthermore, we calculate all $H^0$ and $A^0$ tree-level decay widths in order to get the relevant branching ratios (BR) and also the total widths necessary for the Breit-Wigner propagators of $H^0$ and $A^0$, used to study resonances. We calculate the BRs and total widths analytically and check the results with the help of the *2HDMC* [10] and FA/FC packages.

In this study we consider all theoretical bounds, e.g. unitarity, global minimum, vacuum stability and oblique parameters bounds, as well as all relevant experimental bounds. We derive the theoretical bounds from first principles, comparing them with previous works (see e.g. [11–14]). Furthermore, with these theoretical bounds we perform a numerical scan for finding allowed parameter sets. We then use these allowed sets to perform an in depth numerical study of the $H^0$ and $A^0$ resonances in the production processes $\mu^-\mu^+ \to t\bar{t}, b\bar{b}, \tau^-\tau^+, h^0h^0$ and discuss the results.

The work is structured as follows: in Chapter 1 we introduce the relevant theoretical background, with special focus on the various THDMs under investigation. In Chapter 2 we present the calculations of all $H^0$ and $A^0$ tree-level decay widths. Chapter 3 is dedicated to the derivation of all theoretical bounds and the numerical scan we perform to find the allowed parameter sets. In Chapter 4 we present the current experimental bounds, mainly coming from the LHC searches for additional scalar particles. In Chapter 5 we present the derivation of the formulas for the total cross sections, for the various channels we investigate, as well as a general Breit-Wigner formula that can be used to calculate the total cross section for a certain scattering channel with internal on-shell particles, especially when they have small decay widths compared to their masses. Moreover, we give the definition of the forward-backward asymmetry. In Chapter 6 we present a detailed numerical analysis of the resonances for the $H^0$ and $A^0$ Higgs bosons in the four THD models we investigate. We conclude the work by giving an outlook on further studies.

# Chapter 1

# Theoretical background

In this Chapter we introduce the main theoretical concepts used and explored in this work. It is by no means intended to be exhaustive, and we would therefore refer the reader to [15],[11], [16], [17], [18] and [19] for further information and insights into the topics discussed.

## 1.1 Higgs-Kibble mechanism

In this Section we introduce the general theoretical concepts underlying the Higgs Boson mechanism. In particular we highlight the ideas of global and local symmetry breaking as well as their physical consequences, i.e. the existence of massive particles in the SM. We closely follow the lecture notes [20, 21].

### 1.1.1 Global symmetry breaking

The Higgs-Kibble mechanism relies on the idea of spontaneous symmetry breaking. The main idea behind spontaneous symmetry breaking, is that a Lagrangian $\mathcal{L}$ is invariant under a certain symmetry, but not its ground state. Consider e.g. a Lagrangian invariant under U(1) symmetry and renormalizable. Its most general form would be

$$\mathcal{L} = \left(\partial^{\mu}\phi\right)\left(\partial_{\mu}\phi_{*}\right) - \mu^{2}\phi^{*}\phi - \lambda\left(\phi\phi^{*}\right)^{2} . \tag{1.1}$$

All other terms of higher order in the field $\phi$ are either not renormalizable or not invariant. In order to obtain the ground state of the system, we have to compute the minimum of the Hamiltonian $\mathcal{H} = T - V$

$$\mathcal{H} = \dot{\phi}^{*}\frac{\partial\mathcal{L}}{\partial\dot{\phi}^{*}} + \dot{\phi}\frac{\partial\mathcal{L}}{\partial\dot{\phi}} - \mathcal{L} = \dot{\phi}^{*}\dot{\phi} + \left(\vec{\partial}\phi^{*}\right)\left(\vec{\partial}\phi\right) + V(\phi) . \tag{1.2}$$

The first two terms are positive. Therefore the minimum has to lie in the potential $V(\phi)$. Moreover, in order for the potential to be bounded from below, $\lambda > 0$ must always be

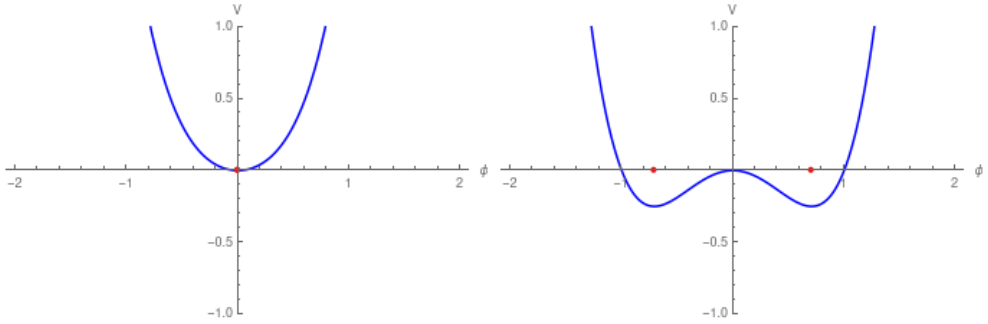


(a) (b)

Figure 1.1: Higgs potential $V(\phi)$ for $\lambda = 1$, $\mu^2 = 1$ (a), and $\mu^2 = -1$ (b). The red point shows the $\phi_0$ value of the minimum for the unbroken and broken symmetry scenario.

satisfied. The minimum of the potential $V(\phi)$ has two solutions depending on the sign of the parameter $\mu^2$.

The first solution $\mu^2 \geq 0$ has the minimum in the origin, $\phi_0 = 0$ ('vacuum' state). The second solution $\mu^2 < 0$, instead has an infinite number of ground states at a radius of

$$r = \sqrt{\frac{-\mu^2}{2\lambda}} := \frac{v}{\sqrt{2}}\,, \tag{1.3}$$

where $v$ is generally referred to as the vacuum expectation value (vev). Since the potential is rotationally symmetric for both cases, the minimum in the second case is a circle. However, in nature only one state is realized. We fix $\phi_0 = r$ at the real axis. For this state $\phi_0$, the symmetry is broken. To interpret the meaning of this symmetry breaking and the phenomenology of the model, we make an expansion around the minimum

$$\phi(x) = \frac{1}{\sqrt{2}}(v + \phi'(x))\,. \tag{1.4}$$

Clearly, $\phi'(x) = 0$ when $\phi(x) = \phi_0$. $\phi'(x)$ is a complex field. We therefore can write its real and imaginary part explicitly as $\phi'(x) = \psi(x) + i\chi(x)$. It follows that

$$\phi(x) = \frac{1}{\sqrt{2}}(v + \psi(x) + i\chi(x))\,. \tag{1.5}$$

We can now substitute this expression for the field back into the Lagrangian $\mathcal{L}$, and obtain

$$\mathcal{L}(\phi) = \frac{1}{2}\left(\partial_\mu\psi\right)^2 + \frac{1}{2}\left(\partial_\mu\chi\right)^2 - \frac{1}{2}\left(2\lambda v^2\right)\psi^2 - \lambda v\psi\left(\psi^2 + \chi^2\right) - \frac{\lambda}{4}\left(\psi^2 + \chi^2\right)^2\,. \tag{1.6}$$

This Lagrangian describes two interacting particles with their masses $m_\psi = 2\lambda v^2$ and $m_\chi = 0$. The appearance of massless particles due to spontaneous symmetry breaking is summarised in the Goldstone Theorem.

**Goldstone theorem:** Massless particles (called "Goldstone particles") appear when a symmetry is spontaneously broken. The number of these particles is given by the number of broken generators of the symmetry group.

### 1.1.2 Local symmetry breaking

Consider again the model described by the Lagrangian $\mathcal{L}$. However, $\mathcal{L}$ should now be invariant under a local U(1) symmetry group. From QED we know that the Lagrangian is locally U(1) invariant, only after introducing the so-called covariant derivative $\partial_\mu \to D_\mu$ and the photon field $A_\mu$. The Lagrangian then takes the form

$$\mathcal{L} = -\frac{1}{4}F_{\mu\nu}F^{\mu\nu} + \left(D^\mu\phi\right)^\dagger \left(D_\mu\phi\right) - V\left(\phi^\dagger\phi\right) \tag{1.7}$$

$$= -\frac{1}{4}F_{\mu\nu}F^{\mu\nu} + \left(\partial^\mu + ieA^\mu\right)\phi\left(\partial_\mu - ieA_\mu\right)\phi^* - \mu^2\phi\phi^* - \lambda\left(\phi\phi^*\right)^2 , \tag{1.8}$$

where $\mathcal{L}$ is invariant under

$$\phi \to e^{i\theta(x)}\phi(x) , \tag{1.9}$$

$$A_\mu \to A_\mu(x) - \frac{1}{e}\partial_\mu\theta(x) . \tag{1.10}$$

As in the case of a global U(1) symmetry, $\lambda > 0$ must hold in order for the potential $V(\phi)$ to be bounded from below, and the parameter $\mu^2$ can be either positive or negative. In the case $\mu^2 > 0$, we obtain a Lagrangian that describes a charged scalar field, i.e. electrodynamics, whereas in the case of $\mu^2 < 0$, we observe spontaneous symmetry breaking. We can now use again the expansion around the minimum

$$\phi(x) = \frac{1}{\sqrt{2}}(v + \psi(x) + i\chi(x)) . \tag{1.11}$$

By inserting this expression back into the Lagrangian, we obtain

$$\mathcal{L} = -\frac{1}{4}F_{\mu\nu}F^{\mu\nu} + \frac{1}{2}\left(\partial_\mu\psi\right)^2 + \frac{1}{2}\left(\partial_\mu\chi\right)^2 + \frac{1}{2}e^2v^2A_\mu A^\mu + \sqrt{2}evA_\mu\partial^\mu\chi + \mu^2\psi^2 + ... \tag{1.12}$$

This Lagrangian produces the mass spectrum

$$m_\psi^2 = -2\mu^2 , \tag{1.13}$$

$$m_\chi^2 = 0 , \tag{1.14}$$

$$m_A^2 = e^2v^2 . \tag{1.15}$$

However, the term $\propto A_\mu\partial^\mu\chi$ generates some issues. This can be easily seen by counting the degrees of freedom before and after symmetry breaking. In particular, the Lagrangian

(1.7) has 2 degrees of freedom from the massless photon field $A_\mu$ and two from the complex field $\phi$, whereas the Lagrangian (1.12) has two degrees of freedom due to the fields $\psi$ and $\chi$ as well as three coming from the now massive $A_\mu$ field. This in turn means that spontaneous symmetry breaking generates an extra degree of freedom that is not realized in nature (non-physical particle). In order to obtain the physical mass spectrum, we use the gauge invariance ($\phi \to e^{i\theta(x)}\phi$) of the Lagrangian $\mathcal{L}(\phi, \phi^*, A_\mu)$. More specifically, we choose the so-called unitarity gauge

$$\theta(x) = -\frac{\chi(x)}{v} \,. \tag{1.16}$$

Moreover, we rewrite the complex field $\phi$ as

$$\phi = \frac{1}{\sqrt{2}} (v + \psi)\, e^{\frac{i\chi}{v}} \,. \tag{1.17}$$

It follows that the U(1) transformation takes in this physical gauge the form

$$\phi \to \phi' = U\phi = \frac{1}{\sqrt{2}} (v + \psi) \,, \tag{1.18}$$

where the Higgs ghost is rotated away and $\psi$ denotes the physical Higgs field. Finally, we arrive at the physical mass spectrum by inserting this expression for the field into the Lagrangian (1.12)

$$\begin{aligned} \mathcal{L} = &-\frac{1}{4} F'_{\mu\nu} F'^{\mu\nu} + \frac{1}{2} (\partial_\mu \psi)(\partial^\mu \psi) + \frac{1}{2} e^2 v^2 A'_\mu A'^\mu + \sqrt{2} e A'^2_\mu \psi (2v + \psi) \\ &- \frac{1}{2}\psi^2 (3\lambda v^2 + \mu^2) - \lambda v \psi^3 - \frac{1}{4}\lambda \psi^4 \,. \end{aligned} \tag{1.19}$$

We can now read off the mass spectrum to be

$$m_\psi^2 = 2\lambda v^2 \,, \tag{1.20}$$

$$m_A = ev \,. \tag{1.21}$$

The field $\chi$ does not appear anymore. It was eliminated through the unitarity gauge transformation. From this analysis we can infer that the Goldstone particle $\chi$ indeed does not correspond to any physical particle. Moreover, in the unitarity gauge, no nonphysical particles (often called ghosts) appear. The degree of freedom "given away" by the field $\chi$ is absorbed into the longitudinal component of the photon field $A_\mu$. The $\psi$ field instead, is the famous Higgs boson $h^0_{\mathrm{SM}}$.

## 1.2 The Two Higgs Doublet Model

The Two Higgs Doublet Model (THDM) is a simple extension of the Standard Model (SM). As the name suggests, in the THDM a second $SU(2)_L$ Higgs doublet is introduced.

The model predicts the existence of three neutral Higgs bosons ($h^0_{SM}, H^0$ and $A^0$) as well as two simply charged Higgs bosons $H^\pm$. This model can be both CP-violating and CP-conserving. In the latter, the Higgs bosons can be classified into the CP-even ($h^0_{SM}, H^0$) states and CP-odd state ($A^0$).

Moreover, the introduction of a second Higgs doublet, leads in general to tree-level flavour changing currents (FCNC). These are mediated by the neutral Higgs bosons. However, by imposing a $Z_2$ discrete symmetry, the FCNC disappear. The $Z_2$ symmetry can be introduced in several different forms. These are captured by a plethora of different THDMs, such as Type-I THDM, Type-II THDM, flipped THDM, lepton-specific THDM and inert THDM. Moreover, in the aligned THDM, where the Yukawa-coupling matrices of the two Higgs doublets are assumed to be proportional to each other, the tree-level FCNC is absent as well. Due a certain type of symmetry, in the Branco-Grimus-Lavoura THDM [22], the FCNC is naturally suppressed by the off-diagonal elements of the CKM matrix.

This simple extension of the SM provides a very rich phenomenology and is also realized in the Minimal Supersymmetric Standard Model (MSSM) as Type-II, as well as effectively in extensions of the MSSM. Various THDMs, such as the ones mentioned above, have been investigated in great detail. E.g. the lepton-specific THDM is used to explain the g-2 anomaly, whereas in the inert THDM, a dark matter (DM) candidate might be realized as the lightest component of the inert Higgs doublet field. DM candidates are also provided by other THDMs, provided that an additional field, protected by a new symmetry, is added [11]. In these models the scalar fields provide a portal between the SM and the DM sectors.

In the following part of the Section we closely follow the review paper by L. Wang et al. [11].

### 1.2.1 General scalar potential

The general scalar potential of a THDM is given by

$$\begin{aligned} V = {} & m_{11}^2(\Phi_1^\dagger\Phi_1) + m_{22}^2(\Phi_2^\dagger\Phi_2) - m_{12}^2(\Phi_1^\dagger\Phi_2 + h.c.) + \frac{\lambda_1}{2}(\Phi_1^\dagger\Phi_1)^2 + \frac{\lambda_2}{2}(\Phi_2^\dagger\Phi_2)^2 \\ & + \lambda_3(\Phi_1^\dagger\Phi_1)(\Phi_2^\dagger\Phi_2) + \lambda_4(\Phi_1^\dagger\Phi_2)(\Phi_2^\dagger\Phi_1) \\ & + \left[\frac{\lambda_5}{2}(\Phi_1^\dagger\Phi_2)^2 + \lambda_6(\Phi_1^\dagger\Phi_1)(\Phi_1^\dagger\Phi_2) + \lambda_7(\Phi_2^\dagger\Phi_2)(\Phi_1^\dagger\Phi_2) + h.c.\right], \end{aligned} \tag{1.22}$$

where

$$\Phi_1 = \begin{pmatrix} \phi_1^+ \\ v_1 + \frac{1}{\sqrt{2}}(\phi_1 + ia_1) \end{pmatrix}, \tag{1.23}$$

$$\Phi_2 = \begin{pmatrix} \phi_2^+ \\ v_2 + \frac{1}{\sqrt{2}}(\phi_2 + ia_2) \end{pmatrix}, \tag{1.24}$$

are the complex Higgs doublets, both with hypercharge $Y = 1$. In this work we restrict ourselves to the CP-conserving models in which all parameters $\lambda_i$ with $i \in [1, 7]$, $m_{11}^2$, $m_{22}^2$ and $m_{12}^2$ are real, and the vacuum expectation values are real as well with $v^2 = v_1^2 + v_2^2 = (246\ \text{GeV})^2$.

### 1.2.2 Type-I, Type-II, lepton-specific and flipped THDMs

By introducing a $Z_2$ symmetry ($\Phi_i \to \pm\Phi_i$, with $\Phi_i$ a scalar doublet) we effectively eliminate FCNCs. In particular the parameters $\lambda_6$ and $\lambda_7$ are absent in (1.51), whereas the soft breaking term $m_{12}^2$ is still present. The $Z_2$ charge assignments are shown in Table 1.1.

| Model | $\Phi_2$ | $\Phi_1$ | $u_R^i$ | $d_R^i$ | $e_R^i$ |
|---|---|---|---|---|---|
| Type I | + | - | + | + | + |
| Type II | + | - | + | - | - |
| Lepton-specific | + | - | + | + | - |
| Flipped | + | - | + | - | + |

Table 1.1: The $Z_2$ charge assignments for the four types of THDMs without FCNC. All other fields not present in the Table are even under the imposed $Z_2$ symmetry.

The mass parameters $m_{11}^2$, $m_{22}^2$, appearing in the potential (1.51), can be determined by the potential minimization conditions at $(v_1, v_2)$:

$$\left.\frac{\partial V}{\partial \Phi_1^\dagger}\right|_{\Phi_{1,0}} = 0\,, \tag{1.25}$$

$$\left.\frac{\partial V}{\partial \Phi_2^\dagger}\right|_{\Phi_{2,0}} = 0\,, \tag{1.26}$$

where we have defined

$$\Phi_{1,0} = \frac{1}{\sqrt{2}}\begin{pmatrix}0\\ v_1\end{pmatrix}\,, \tag{1.27}$$

$$\Phi_{2,0} = \frac{1}{\sqrt{2}}\begin{pmatrix}0\\ v_2\end{pmatrix}\,, \tag{1.28}$$

to be the fields evaluated at the minimum. The two equations with the derivatives (1.25) and (1.26) can be rewritten in terms of the mass parameters $m_{11}^2$ and $m_{22}^2$ as a function of the vacuum expectation values, $m_{12}^2$ and the parameters $\lambda_i$:

$$m_{11}^2 = \frac{-\lambda_1 v_1^3 - \lambda_3 v_1 v_2^2 - \lambda_4 v_1 v_2^2 - \lambda_5 v_1 v_2^2 + 2m_{12}^2 v_2}{2v_1}\,, \tag{1.29}$$

$$m_{22}^2 = \frac{-\lambda_2 v_2^3 - \lambda_3 v_1^2 v_2 - \lambda_4 v_1^2 v_2 - \lambda_5 v_1^2 v_2 + 2m_{12}^2 v_1}{2v_2}\,. \tag{1.30}$$

With the definitions and shorthand notations $\tan\beta = \frac{v_2}{v_1} := t_\beta$, $\cos\beta := c_\beta$, $\sin\beta := s_\beta$, $\lambda_{ijk} := \lambda_i + \lambda_j + \lambda_k$ and $v_1^2 + v_2^2 = v^2$, we can simplify (1.29) and (1.30) to obtain

$$m_{11}^2 = m_{12}^2 t_\beta - \frac{1}{2}v^2\left(\lambda_1 c_\beta^2 + \lambda_{345} s_\beta^2\right) , \tag{1.31}$$

$$m_{22}^2 = m_{12}^2 \frac{1}{t_\beta} - \frac{1}{2}v^2\left(\lambda_2 s_\beta^2 + \lambda_{345} c_\beta^2\right) . \tag{1.32}$$

Moreover, from the potential (1.51), with $\lambda_6 = \lambda_7 = 0$, we obtain the mass matrices of the Higgs fields

$$\begin{pmatrix}\phi_1 & \phi_2\end{pmatrix}\begin{pmatrix} m_{12}^2 t_\beta + \lambda_1 v^2 c_\beta^2 & -m_{12}^2 + \frac{\lambda_{345}}{2}v^2 s_{2\beta} \\ -m_{12}^2 + \frac{\lambda_{345}}{2}v^2 s_{2\beta} & m_{12}^2/t_\beta + \lambda_2 v^2 s_\beta^2 \end{pmatrix}\begin{pmatrix}\phi_1 \\ \phi_2\end{pmatrix} , \tag{1.33}$$

$$\begin{pmatrix}a_1 & a_2\end{pmatrix}\left[m_{12}^2 - \frac{1}{2}\lambda_5 v^2 s_{2\beta}\right]\begin{pmatrix} t_\beta & -1 \\ -1 & 1/t_\beta \end{pmatrix}\begin{pmatrix}a_1 \\ a_2\end{pmatrix} , \tag{1.34}$$

$$\begin{pmatrix}\phi_1^+ & \phi_2^+\end{pmatrix}\left[m_{12}^2 - \frac{1}{4}(\lambda_4 + \lambda_5) v^2 s_{2\beta}\right]\begin{pmatrix} t_\beta & -1 \\ -1 & 1/t_\beta \end{pmatrix}\begin{pmatrix}\phi_1^- \\ \phi_2^-\end{pmatrix} . \tag{1.35}$$

From the original fields we can obtain the mass eigenstates by the rotation matrices

$$\begin{pmatrix}H^0 \\ h^0\end{pmatrix} = \begin{pmatrix}\cos\alpha & \sin\alpha \\ -\sin\alpha & \cos\alpha\end{pmatrix}\begin{pmatrix}\phi_1 \\ \phi_2\end{pmatrix} , \tag{1.36}$$

$$\begin{pmatrix}G^0 \\ A^0\end{pmatrix} = \begin{pmatrix}\cos\beta & \sin\beta \\ -\sin\beta & \cos\beta\end{pmatrix}\begin{pmatrix}a_1 \\ a_2\end{pmatrix} , \tag{1.37}$$

$$\begin{pmatrix}G^\pm \\ H^\pm\end{pmatrix} = \begin{pmatrix}\cos\beta & \sin\beta \\ -\sin\beta & \cos\beta\end{pmatrix}\begin{pmatrix}\phi_1^\pm \\ \phi_2^\pm\end{pmatrix} . \tag{1.38}$$

Here $G^0$ and $G^\pm$ are the Goldstone bosons which are absorbed by the $W^\pm$ and $Z^0$ bosons as their longitudinal components. In conclusion, five physical states remain: the two CP-even states $h^0$ and $H^0$, the neutral pseudo-scalar $A$ and a pair of simply charged scalars $H^\pm$. The masses of the bosons can be obtained by diagonalization of the mass matrices (1.33),(1.34) and (1.35). The eigenvalues obtained from diagonalization are then the masses of the bosons. The first matrix gives the masses of the CP-even states $h^0$ and $H^0$. They are given by

$$m_{H^0,h^0}^2 = \frac{1}{2}\left(x_{11}^2 + x_{22}^2 \pm \sqrt{\left(x_{11}^2 - x_{22}^2\right)^2 + 4\left(x_{12}^2\right)^2}\right) , \tag{1.39}$$

where $x_{ij}$ are the entries of the matrix (1.33). For the second matrix (1.34), we find the first eigenvalue to be equal to zero, i.e the Goldstone boson, and a second eigenvalue which gives the mass of the CP-odd Boson $A$

$$m_{A^0}^2 = \frac{m_{12}^2}{s_\beta c_\beta} - \lambda_5 v^2 . \tag{1.40}$$

The third matrix (1.35) has the same structure as (1.34). It also has the first eigenvalue equal to zero, i.e. the mass of the second Goldstone boson $G^{\pm}$, and a second eigenvalue which gives the mass of the simply charged $H^{\pm}$ boson

$$m^2_{H^{\pm}} = \frac{m^2_{12}}{s_\beta c_\beta} - \frac{1}{2}\left(\lambda_4 + \lambda_5\right) v^2 \,. \tag{1.41}$$

The gauge-kinetic part of the Lagrangian $\mathcal{L}$ describing a THDM is given by

$$\mathcal{L}_g = \left(D^\mu \Phi_1\right)^\dagger \left(D_\mu \Phi_1\right) + \left(D^\mu \Phi_2\right)^\dagger \left(D_\mu \Phi_2\right) \,. \tag{1.42}$$

From this part of the Lagrangian $\mathcal{L}$ we can derive the couplings ($\{h^0, H^0, A^0\}VV$) of the three neutral Higgs bosons to the gauge bosons $V = Z^0, W^{\pm}$

$$\begin{aligned} \mathcal{L}_g \supset & \frac{g^2 + g'^2}{8} v^2 Z Z \left(1 + 2\frac{h^0}{v} y^V_{h^0} + 2\frac{H^0}{v} y^V_{H^0}\right) \\ & + \frac{g^2}{4} v^2 W^+ W^- \left(1 + 2\frac{h^0}{v} y^V_{h^0} + 2\frac{H^0}{v} y^V_{H^0}\right), \end{aligned} \tag{1.43}$$

where we use the definitions $y^V_h = \sin\left(\beta - \alpha\right) := s_{\beta-\alpha}$ and $y^V_H = \cos\left(\beta - \alpha\right) := c_{\beta-\alpha}$. According to the different charge assignments in Tab.1.1, there are four different models with Yukawa interactions:

$$-\mathcal{L} = Y_{u2}\, \overline{Q}_L\, \tilde{\Phi}_2\, u_R + Y_{d2}\, \overline{Q}_L\, \Phi_2\, d_R + Y_{\ell 2}\, \overline{L}_L\, \Phi_2\, e_R + \text{h.c. (Type-I)}, \tag{1.44}$$

$$-\mathcal{L} = Y_{u2}\, \overline{Q}_L\, \tilde{\Phi}_2\, u_R + Y_{d1}\, \overline{Q}_L\, \Phi_1\, d_R + Y_{\ell 1}\, \overline{L}_L\, \Phi_1\, e_R + \text{h.c. (Type-II)}, \tag{1.45}$$

$$-\mathcal{L} = Y_{u2}\, \overline{Q}_L\, \tilde{\Phi}_2\, u_R + Y_{d1}\, \overline{Q}_L\, \Phi_2\, d_R + Y_{\ell 1}\, \overline{L}_L\, \Phi_1\, e_R + \text{h.c. (lepton-specific)}, \tag{1.46}$$

$$-\mathcal{L} = Y_{u2}\, \overline{Q}_L\, \tilde{\Phi}_2\, u_R + Y_{d1}\, \overline{Q}_L\, \Phi_1\, d_R + Y_{\ell 1}\, \overline{L}_L\, \Phi_2\, e_R + \text{h.c. (flipped)}, \tag{1.47}$$

where $Q^T_L = (u_L\,, d_L)$, $L^T_L = (\nu_L\,, l_L)$, $\widetilde{\Phi}_{1,2} = i\tau_2 \Phi^*_{1,2}$, and $Y_{u2}$, $Y_{d1,2}$ and $Y_{\ell 1,2}$ are $3 \times 3$ matrices in family space. We derive the Yukawa couplings to the fermions from

$$\begin{aligned} -\mathcal{L}_Y \;=\; & \frac{m_f}{v}\, y^f_{h^0}\, h^0 \bar{f} f + \frac{m_f}{v}\, y^f_{H^0}\, H^0 \bar{f} f \\ & -i\frac{m_u}{v}\kappa_u\, A^0 \bar{u}\gamma_5 u + i\frac{m_d}{v}\kappa_d\, A^0 \bar{d}\gamma_5 d + i\frac{m_\ell}{v}\kappa_\ell\, A^0 \bar{\ell}\gamma_5 \ell \\ & + \left( H^+\, \bar{u}\, V_{\text{CKM}}\, (\frac{\sqrt{2} m_d}{v}\kappa_d P_R - \frac{\sqrt{2} m_u}{v}\kappa_u P_L) d + h.c. \right) \\ & + \left( \frac{\sqrt{2} m_\ell}{v}\kappa_\ell H^+\, \bar{\nu} P_R e + h.c. \right), \end{aligned} \tag{1.48}$$

where $y^f_h = \sin(\beta - \alpha) + \cos(\beta - \alpha)\kappa_f$ and $y^f_H = \cos(\beta - \alpha) - \sin(\beta - \alpha)\kappa_f$. The values of $\kappa_u$, $\kappa_d$ and $\kappa_\ell$ for the four models are shown in Table 1.2.

| | Type-I | Type-II | lepton-specific | flipped |
|---|---|---|---|---|
| $\kappa_u$ | $1/t_\beta$ | $1/t_\beta$ | $1/t_\beta$ | $1/t_\beta$ |
| $\kappa_d$ | $1/t_\beta$ | $-t_\beta$ | $1/t_\beta$ | $-t_\beta$ |
| $\kappa_\ell$ | $1/t_\beta$ | $-t_\beta$ | $-t_\beta$ | $1/t_\beta$ |

Table 1.2: The $\kappa_u$, $\kappa_d$, and $\kappa_\ell$ for the four types of THDMs.

### 1.2.3 Inert THDM

For completeness we also briefly discuss the inert THDM. In this model we impose an exact $Z_2$ symmetry and assume that it remains after the potential is minimized. We take the SM fields to be even under this symmetry whereas the second doublet $\Phi_2$ is taken to be odd

$$\Phi_1 = \begin{pmatrix} G^+ \\ \frac{1}{\sqrt{2}}(v + h + iG) \end{pmatrix}, \tag{1.49}$$

$$\Phi_2 = \begin{pmatrix} H^+ \\ \frac{1}{\sqrt{2}}(H + iA) \end{pmatrix}, \tag{1.50}$$

In this model the $\Phi_1$ doublet has an expectation value $v = 246$ GeV and $\Phi_2$ has no vacuum expectation value. The scalar potential in (1.51) thus reduces to

$$\begin{aligned} V = {} & m_{11}^2(\Phi_1^\dagger\Phi_1) + m_{22}^2(\Phi_2^\dagger\Phi_2) + \frac{\lambda_1}{2}(\Phi_1^\dagger\Phi_1)^2 + \frac{\lambda_2}{2}(\Phi_2^\dagger\Phi_2)^2 \\ & + \lambda_3(\Phi_1^\dagger\Phi_1)(\Phi_2^\dagger\Phi_2) + \lambda_4(\Phi_1^\dagger\Phi_2)(\Phi_2^\dagger\Phi_1) \\ & + \left[\frac{\lambda_5}{2}(\Phi_1^\dagger\Phi_2)^2 + h.c.\right] . \end{aligned} \tag{1.51}$$

In analogy to Section 1.2.2, we obtain the mass parameter $m_{11}^2$, by the potential minimization conditions, to be

$$m_{11}^2 = -\frac{1}{2}\lambda_1 v^2 . \tag{1.52}$$

We note that $m_{22}^2$ is not fixed due to its vev equal to zero. Moreover, the fields $A$ and $H^\pm$ have mass eigenstates

$$m_A^2 = m_{H^\pm}^2 + \frac{1}{2}(\lambda_4 - \lambda_5)\, v^2 , \tag{1.53}$$

$$m_{H^\pm}^2 = m_{22}^2 + \frac{\lambda_3}{2} v^2 . \tag{1.54}$$

In the inert THDM no mixing between the two CP-even states $h$ and $H$ is allowed, and their masses are given by

$$m_h^2 = \lambda_1 v^2 := (125\ \text{GeV})^2 , \tag{1.55}$$

$$m_H^2 = m_A^2 + \lambda_5 v^2 . \tag{1.56}$$

The fermion masses can be derived from the Yukawa interaction terms in the Lagrangian $\mathcal{L}$. More specifically by their interactions with the doublet $\Phi_1$

$$-\mathcal{L} = y_u \bar{Q}_L \tilde{\Phi}_1 u_R + y_d \bar{Q}_L \Phi_1 d_R + y_1 \bar{L}_L \Phi_1 e_R + h.c., \tag{1.57}$$

where $y_u$, $y_d$ and $y_l$ are 3x3 matrices in family space. The exact $Z_2$ symmetry imposed, causes the doublet $\Phi_2$ to not have any Yukawa interactions with fermions. Moreover, the lightest neutral field $H$ or $A$, is stable and can thus be considered a dark matter (DM) candidate. We also note that if right-handed neutrinos were introduced, the $\Phi_2$ doublet could interact with them, giving rise to the neutrino masses via one loop diagrams with DM [23].

## 1.3 Breit-Wigner resonance

The propagator for a scalar particle is given in momentum space by

$$\frac{i}{q^2 - m^2}\,. \tag{1.58}$$

It is evident that when the center of mass energy $\sqrt{S}$ (i.e. the transferred momentum $q^2$ for s-channel scatterings) is equal to the mass of the boson mediating the scattering, the term diverges to infinity. This is because the propagator does not account for the fact that these bosons are unstable particles. There are multiple ways of deriving a propagator that accounts for a decaying state. Here, we derive it from the time dependence of the wave function for a decaying state [19]. If the particle were stable, the time dependence in the rest frame of the particle would be given by

$$\psi \propto e^{-imt}\,. \tag{1.59}$$

In order to account for the instability, we introduce the total decay rate $\Gamma = \frac{1}{\tau}$, such that

$$\psi \propto e^{-imt} e^{-\Gamma \frac{t}{2}}\,. \tag{1.60}$$

The probability density then decays as

$$\psi\psi^* = e^{-\frac{t}{\tau}}\,. \tag{1.61}$$

We can introduce this exponential decay by replacing

$$m \to m - i\frac{\Gamma}{2}\,. \tag{1.62}$$

Since $\Gamma \ll m$ for the observed particles, the propagator reduces to

$$\frac{1}{q^2 - m_i^2} \to \frac{1}{q^2 - m_i^2 + i m_i \Gamma_i}\,, \tag{1.63}$$

with i being the boson flavour appearing in the respective matrix element. The squared propagator appearing in the cross section $\sigma$ then becomes

$$\sigma \propto |M|^2 \propto \left| \frac{1}{S - m_i^2 + im_i\Gamma_i} \right|^2 = \frac{1}{(S - m_i^2)^2 + m_i^2\Gamma_i^2} \,. \tag{1.64}$$

This form of the propagator is generally called the Breit-Wigner form and the dependence on the center of mass energy S is referred to as Breit-Wigner resonance.

In the case of interference terms appearing in the matrix element of the studied scattering process, only the real part of the interference matrix element must be taken. The real part of the Breit-Wigner propagator can be obtained by simultaneously multiplying and dividing by the conjugate of the propagator and then simplifying the expression

$$\frac{1}{q^2 - m_i^2 + im_i\Gamma_i} \left( \frac{\frac{1}{q^2 - m_i^2 - im_i\Gamma_i}}{\frac{1}{q^2 - m_i^2 - im_i\Gamma_i}} \right) = \tag{1.65}$$
$$\frac{(q^2 - m_i^2 - im_i\Gamma_i)}{(q^2 - m_i^2)^2 + m_i^2\Gamma_i^2} \,.$$

The real part is then given by

$$\frac{(q^2 - m_i^2)}{(q^2 - m_i^2)^2 + m_i^2\Gamma_i^2} \,. \tag{1.66}$$

In conclusion, we can compute the matrix elements for the studied scattering processes and then substitute the propagators with (1.64) or (1.65). This allows us to study resonances with finite cross sections $\sigma$ for all $\sqrt{S}$.

# Chapter 2

# Total decay widths $\Gamma$

In order to explore the $H^0$ and $A^0$ Higgs bosons resonances, we introduce the Breit-Wigner form as presented in Section 1.3. Thus, we need to compute the total decay widths of the $H^0$ and $A^0$ Higgs bosons. Moreover, we compute the partial decay widths, to compute the branching ratios (BRs) of $H^0$ and $A^0$ decaying into the investigated production channels, for each allowed parameter set. This enables us to quantify the possibility of seeing a resonance at a future Muon Collider experiment for each parameter point.

All partial decay width formulas are checked analytically with [24] and FA/FC[1] [8, 9], numerically with FA/FC and the *2HDMC* package [10]. Furthermore, we make use of the optical theorem [25]

$$\Gamma = \frac{\Im(\Sigma(m^2))}{m}\,, \tag{2.1}$$

where $\Sigma(m^2)$ is the self-energy of a scalar particle. We cross-checked this formula with FA/FC and our own analytical results for the partial decay widths.

The general form for the decay width $\Gamma$ is given by [20]

$$d\Gamma = \frac{1}{2m}\overline{|M|}^2 \mathrm{dLips}\,, \tag{2.2}$$

where dLips is the Lorentz-invariant phase space. All the decay channels that we investigate in this study are two-body decays. Therefore, we insert the two-particle phase space

$$\mathrm{dLips}_2 = \frac{1}{8\pi}\frac{\sqrt{\lambda(m^2, m_1^2, m_2^2)}}{m^2}\,, \tag{2.3}$$

to obtain the total decay width

$$\Gamma = \frac{\sqrt{\lambda(m^2, m_1^2, m_2^2)}}{16\pi m^3}\overline{|M|}^2\,, \tag{2.4}$$

[1]We enlarged the given FA/FC code from only considering the Type-II THDM to include all four THDMs explored in this work.

where $\lambda(m^2, m_1^2, m_2^2)$ denotes the Källén function, defined as

$$\lambda(x, y, z) = x^2 + y^2 + z^2 - 2xy - 2xz - 2yz. \tag{2.5}$$

Throughout the section we identify the up-type quarks with $u_i = \{u, c, t\}$, the down-type quarks with $d_i = \{d, s, b\}$ and the three generations of charged leptons with $l_i = \{e, \mu, \tau\}$.

## 2.1 Total decay width of $H^0$

In this subsection we show the decay widths of the $H^0$ Higgs boson. As an example we show the derivation of the decay width $\Gamma_{H^0} \to u\bar{u}$ explicitly and then list the remaining results for the decay widths into the Higgs bosons, down quarks, leptons and gauge bosons.

### 2.1.1 $\Gamma_{H^0} \to u\bar{u}$

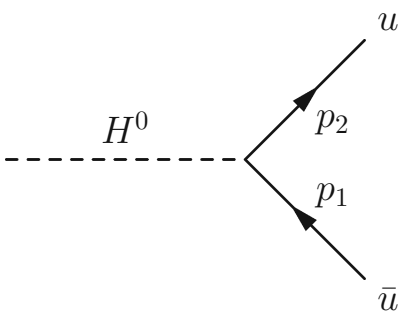


Figure 2.1: Feynman diagram of the decay $H^0 \to u\bar{u}$ in the THDM. All momenta are in time direction from left to right.

The couplings to the three up-type quark pairs differ only in their mass. Therefore, we can compute the decay width for e.g. the top quark and then substitute the mass to obtain the remaining up and charm quarks. Since the $H^0$ Higgs boson is a scalar, the matrix element is only given by the coupling to the up-type quarks and the spinors of the outgoing quarks

$$M_t = -i\frac{2m_t s_\alpha}{2m_w s_w s_\beta}\bar{u}(p_1)v(p_2). \tag{2.6}$$

Here we have introduced the notation $s_w := \sin(\theta_w)$ (we will use this notation throughout the work). Momentum conservation is given by $p = p_1 + p_2$. We compute the matrix element squared with the help of the trace technique [20]. In particular by using the known formulas

$$\sum u\bar{u} = \not{p} + m \tag{2.7}$$

$$\sum v\bar{v} = \not{p} - m \tag{2.8}$$

we obtain

$$\overline{|M_t|}^2 = c^2 \sum_s \bar{u}(p_1)v(p_2)\bar{v}(p_2)u(p_1) \tag{2.9}$$

$$= c^2 Tr\{(\not{p}_1 + m_t)(\not{p}_2 - m_t)\} \tag{2.10}$$

$$= c^2 4\left(p_1 \cdot p_2 - m_t^2\right) , \tag{2.11}$$

where we have defined

$$c^2 := \frac{e^2 m_t^2 s_\alpha^2}{4 m_w^2 s_w^2 s_\beta^2}. \tag{2.12}$$

From the definition of the Mandelstam variable $S := (p_1+p_2)^2$, we can derive an expression for the inner product between the two outgoing momenta in (2.9)

$$S := (p_1 + p_2)^2 = 2m_t^2 + 2p_1 \cdot p_2. \tag{2.13}$$

Solving for the inner product of the momenta and setting the $H^0$ Higgs boson on-shell, we obtain

$$\overline{|M_t|}^2 = 2c^2\left(m_{H^0}^2 - 4m_t^2\right). \tag{2.14}$$

After inserting the expression for the matrix element squared (2.14) into the general expression for the total decay width (2.4), we obtain

$$\Gamma_{H^0 \to u\bar{u}} = \frac{m_{H^0}\left(1 - \frac{4m_{u_i}^2}{m_{H^0}^2}\right)^{3/2}\left(e^2 m_{u_i}^2 N_c s_\alpha^2\right)}{(32\pi)\left(m_w^2 s_\beta^2 s_w^2\right)}, \tag{2.15}$$

where we have multiplied each width by $N_c = 3$ which accounts for the color charge of the quarks and added the widths of all three quarks together.

### 2.1.2 List of all possible decay widths

Here we list all possible decay widths of the neutral $H^0$ Higgs boson:

$$\Gamma_{H^0 \to u_i\bar{u}_i} = \sum_{i=1}^{3} \frac{m_{H^0}\left(1 - \frac{4m_{u_i}^2}{m_{H^0}^2}\right)^{3/2}\left(e^2 m_{u_i}^2 N_c s_\alpha^2\right)}{(32\pi)\left(m_w^2 s_\beta^2 s_w^2\right)}, \tag{2.16}$$

$$\Gamma_{H^0 \to d_i\bar{d}_i} = \sum_{i=1}^{3} \frac{1}{32\pi}(1 - 4\frac{m_{d_i}^2}{m_{H^0}^2})^{\frac{3}{2}} m_{H^0} \frac{e^2 m_{d_i}^2 c_\alpha^2 N_c}{m_w^2 s_w^2 c_\beta^2}, \tag{2.17}$$

$$\Gamma_{H^0 \to l_i^- l_i^+} = \sum_{i=1}^{3} \frac{1}{32\pi}(1 - 4\frac{m_{l_i}^2}{m_{H^0}^2})^{\frac{3}{2}} m_{H^0} \frac{e^2 m_{l_i}^2 c_\alpha^2}{m_w^2 s_w^2 c_\beta^2}, \tag{2.18}$$

$$\Gamma_{H^0\to h^0h^0} = \frac{c^2_{\beta-\alpha}e^2 m_{h^0}\sqrt{1-\frac{4m^2_{h^0}}{m^2_{H^0}}}\left(s_{2\alpha}\left(2m^2_{h^0}+m^2_{H^0}\right)-\frac{\lambda_5 m^2_w s^2_w(3s_{2\alpha}-s_{2\beta})}{2\pi\alpha}\right)^2}{128\pi m_{H^0}m^2_w s^2_{2\beta}s^2_w}, \tag{2.19}$$

$$\Gamma_{H^0\to A^0A^0} = \frac{e^2 m_{A^0}\sqrt{1-\frac{4m^2_{A^0}}{m^2_{H^0}}}\left(\frac{s_{\alpha-\beta}\left(2m^2_{H^0}-\frac{\lambda_5 m^2_w s^2_w}{\pi\alpha}\right)}{s_{2\beta}}-c_{\beta-\alpha}\left(m^2_{H^0}-2m^2_{A^0}\right)\right)^2}{128\pi m_{H^0}m^2_w s^2_w}, \tag{2.20}$$

$$\Gamma_{H^0\to Z^0A^0} = \frac{g^2 s^2_{\beta-\alpha}}{64\pi m^3_{H^0}}\lambda^{\frac{3}{2}}(m^2_{H^0},m^2_{Z^0},m^2_{A^0})\frac{1}{m^2_w}, \tag{2.21}$$

$$\Gamma_{H^0\to Z^0Z^0} = \frac{g^2 c^2_{\beta-\alpha}}{128\pi m_{H^0}m^2_Z c^2_w}\left(1-\frac{4m^2_{Z^0}}{m^2_{H^0}}\right)^{\frac{1}{2}}(12m^4_Z+m^4_{H^0}-4m^2_{H^0}m^2_Z), \tag{2.22}$$

$$\Gamma_{H^0\to W^\pm H^\mp} = \frac{g^2 s^2_{\beta-\alpha}}{64\pi m^2_w m^3_{H^0}}\lambda^{\frac{3}{2}}(m^2_{H^0},m^2_w,m^2_{H^\pm}), \tag{2.23}$$

$$\Gamma_{H^0\to W^+W^-} = \frac{e^2 c^2_{\beta-\alpha}}{64\pi s^2_w m^2_w m_{H^0}}\sqrt{1-\frac{4m^2_w}{m^2_{H^0}}}\left(-4m^2_{H^0}m^2_w+m^4_{H^0}+12m^4_w\right), \tag{2.24}$$

$$\Gamma_{H^0\to H^+H^-} = \frac{1}{16\pi m_{H^0}}\left(1-4\frac{m^2_H}{m^2_{H^0}}\right)^{\frac{1}{2}}\frac{e^2}{4m^2_w s^2_w} \left(c_{\beta-\alpha}(2m^2_H-m^2_{H^0})+\frac{s_{\beta+\alpha}}{s_{2\beta}}(2m^2_{H^0}-\frac{4\lambda_5 m^2_w s^2_w}{e^2})\right)^2. \tag{2.25}$$

## 2.2 Total decay width $A^0$

In this Subsection we show the decay widths for the CP-odd $A^0$ Higgs boson. We show as an example the derivation of the decay width $\Gamma_{A^0\to Z^0h^0}$ explicitly and then list the remaining results for the decay widths into the Higgs bosons, down quarks, leptons and gauge bosons.

### 2.2.1 $\Gamma_{A^0\to Zh^0}$

The coupling for the vertex $A^0 \to Zh^0$ is given by

$$C(A^0,Z,h^0) = \frac{ec_{\beta-\alpha}}{2c_w s_w} := c, \tag{2.26}$$

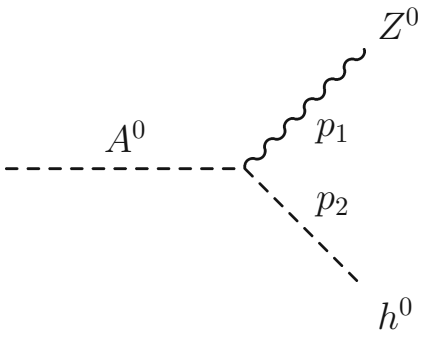


Figure 2.2: Feynman diagram of the decay $A^0 \to Z^0 h^0$ in the THDM. All momenta are in time direction from left to right.

and momentum conservation is given by $p = p_1 + p_2$. In this decay we have two scalars, and therefore only the polarization vector $\epsilon^\mu(p_1)$ of the $Z^0$ boson appears in the matrix element,

$$M_{Z^0 h^0} = \frac{e c_{\beta-\alpha}}{2 c_w s_w} \epsilon^\mu(p_1)(p - p_2)_\mu. \tag{2.27}$$

Using

$$\sum_{\lambda=-1,0,1} \epsilon^\mu(p_1,\lambda)\epsilon^{*\nu}(p_1,\lambda) = -g^{\mu\nu} + \frac{p^\mu p^\nu}{m_V^2}\,, \tag{2.28}$$

we now can compute the matrix element squared

$$\overline{|M_{Zh^0}|}^2 = c^2 \epsilon^\mu(p_1)(p-p_2)_\mu \epsilon^{*\nu}(p_1)(p-p_2)_\nu \tag{2.29}$$

$$= c^2 \left( \frac{p_1^\mu p_1^\nu}{m_Z^2} - g^{\mu\nu} \right) (p-p_2)_\mu (p-p_2)_\nu \tag{2.30}$$

$$= c^2 \frac{\lambda(m_{A^0}^2, m_Z^2, m_{h^0}^2)}{m_{h^0}^2}. \tag{2.31}$$

Now we can insert the matrix element squared in (2.4) and obtain

$$\Gamma_{A^0 \to Z^0 h^0} = \frac{c_{\beta-\alpha}^2 g^2 \lambda\left(m_{A^0}^2, m_{H^0}^2, m_{Z^0}^2\right)^{\frac{3}{2}}}{64\pi c_w^2 m_{A^0}^3 m_{Z^0}^2}\,. \tag{2.32}$$

### 2.2.2 List of all possible decay widths

Here we list all possible decay widths of the neutral $A^0$ Higgs boson:

$$\Gamma_{A^0 \to u_i \bar{u}_i} = \sum_{i=1}^{3} \frac{g^2 m_{A^0} m_{u_i}^2 N_c \sqrt{1 - \frac{4m_{u_i}^2}{m_{A^0}^2}}}{(8\pi)\,(4m_w^2)\,t_\beta^2}\,, \tag{2.33}$$

$$\Gamma_{A^0\to d_i\bar{d}_i} = \sum_{i=1}^{3} \frac{g^2 m_{A^0} m_{d_i}^2 N_c Y_3^2 \sqrt{1-\frac{4m_{d_i}^2}{m_{A^0}}}}{(8\pi)\,(4m_w^2)}\,, \tag{2.34}$$

$$\Gamma_{A^0\to l_i^- l_i^+} = \sum_{i=1}^{3} \frac{m_{A^0}\left(1-\frac{4m_{l_i}^2}{m_{A^0}^2}\right)^2 \left(2e^2 m_{A^0}^2 m_{l_i}^2 Y_3^2\right)}{\left(16\pi m_{A^0}^2\right)\left(4m_w^2 s_w^2\right)}\,, \tag{2.35}$$

$$\Gamma_{A^0\to Z^0 h^0} = \frac{\left(c_{\beta-\alpha}^2 g^2\right)\lambda\left(m_{A^0}^2, m_{H^0}^2, m_{Z^0}^2\right)^{\frac{3}{2}}}{64\pi c_w^2 m_{A^0}^3 m_{Z^0}^2}\,, \tag{2.36}$$

$$\Gamma_{A^0\to Z^0 H^0} = \frac{\left(g^2 s_{\beta-\alpha}^2\right)\lambda\left(m_{A^0}^2, m_{H^0}^2, m_{Z^0}^2\right)^{\frac{3}{2}}}{\left(64\pi m_{H^0}^3\right) m_w^2}\,, \tag{2.37}$$

$$\Gamma_{A^0\to W^\pm H^\pm} = \frac{2g^2\lambda\left(m_{A^0}^2, m_{H^\pm}^2, m_w^2\right)^3}{64\pi m_{A^0}^3 m_w^2}\,. \tag{2.38}$$

# Chapter 3

# Theoretical bounds

In this chapter we derive the theoretical bounds which restrict the THDM parameter space $(m_{H^0}, m_{A^0}, m_{H^\pm}, \tan\beta, \sin\alpha, \lambda_5)$. In particular we derive from first principles the bounds: vacuum stability, unitarity and oblique parameters (S,T,U). Moreover, we include a bound which ensures that the vacuum we are in, is the vacuum corresponding to the global minimum of the THDM potential (3.5)[26]. We then perform a numerical scan over these bounds for random sets of input parameters and use the allowed sets in the subsequent search for $H^0$ and $A^0$ resonances. For the numerical scan we have written a *python* code with a performance of scanning $10^9$ sets in approximately 4 hours (depending on the performance of the computer used). Moreover, the code also enables to check single points [1].

## 3.1 Parameters

For this study it is more suitable to substitute the input parameters $\lambda_i$ with $i \in [1, 4]$, for the four physical masses of the Higgs bosons, the mixing angles $\alpha$, $\beta$ and the coupling $\lambda_5$. We use these 7 input parameters throughout the work as the free parameters of the model. We thus need to express $\lambda_{1,2,3,4}$ as a function of these 7 parameters. This was done by inverting the expressions for the physical masses of the bosons (1.39),(1.40) and

[1] The code can be ordered from the author via email: leonardobellinato@gmail.com

(1.41), with the help of *Mathematica*. We obtain for the parameters $\lambda_i$

$$\lambda_1 = \frac{1}{v^2 c_\beta^2}\left(c_\alpha^2 m_{H^0}^2 + s_\alpha^2 m_{h^0}^2 - m_{12}^2 \frac{s_\beta}{c_\beta}\right), \tag{3.1}$$

$$\lambda_2 = \frac{1}{v^2 s_\beta^2}\left(s_\alpha^2 m_{H^0}^2 + c_\alpha^2 m_{h^0}^2 - m_{12}^2 \frac{c_\beta}{s_\beta}\right), \tag{3.2}$$

$$\lambda_3 = 2\frac{m_{H^\pm}^2}{v^2} + \frac{s_{2\alpha}(m_{H^0}^2 - m_{h^0}^2)}{v^2 s_{2\beta}} - \frac{m_{12}^2}{v^2 s_\beta c_\beta}, \tag{3.3}$$

$$\lambda_4 = \frac{m_{A^0}^2 - 2m_{H^\pm}^2}{v^2} + \frac{m_{12}^2}{v^2 s_\beta c_\beta}. \tag{3.4}$$

## 3.2 Vacuum stability

In order to guarantee a stable vacuum, the scalar potential $V$ has to be positive for arbitrarily large values of the fields $\Phi_1$ and $\Phi_2$ [11]. The Higgs potential (1.51) with a soft $Z_2$ symmetry breaking term, is given by

$$\begin{aligned} V = {} & m_{11}^2(\Phi_1^\dagger\Phi_1) + m_{22}^2(\Phi_2^\dagger\Phi_2) - m_{12}^2(\Phi_1^\dagger\Phi_2 + h.c.) + \frac{\lambda_1}{2}(\Phi_1^\dagger\Phi_1)^2 + \frac{\lambda_2}{2}(\Phi_2^\dagger\Phi_2)^2 \\ & + \lambda_3(\Phi_1^\dagger\Phi_1)(\Phi_2^\dagger\Phi_2) + \lambda_4(\Phi_1^\dagger\Phi_2)(\Phi_2^\dagger\Phi_1) + \left[\frac{\lambda_5}{2}(\Phi_1^\dagger\Phi_2)^2 + h.c.\right] \end{aligned} \tag{3.5}$$

Note that due to the $Z_2$ symmetry imposed, the $\lambda_6$ and $\lambda_7$ terms disappear. To simplify the derivation of the vacuum stability conditions, we parameterize the fields as

$$\begin{aligned} \Phi_1^\dagger\Phi_1 &= X_1^2, \\ \Phi_2^\dagger\Phi_2 &= X_2^2, \\ \Phi_1^\dagger\Phi_2 &= X_1 X_2 \rho e^{i\theta}, \end{aligned}$$

with $0 \leq \rho \leq 1$. Moreover, for large values of the fields $\Phi_i$, the quadratic terms can be neglected. The remaining quartic terms are

$$V_4 = \frac{\lambda_1}{2}X_1^4 + \frac{\lambda_2}{2}X_2^4 + \lambda_3 X_1^2 X_2^2 + \lambda_4 X_1^2 X_2^2 \rho^2 + \lambda_5 X_1^2 X_2^2 \rho^2 \cos 2\theta. \tag{3.6}$$

Since we are looking for minimum (lower bound on $V$), we can stabilize $\theta$ at the minimum. We obtain the $\theta$-independent part of the potential $V_4$

$$V_{4-\theta-indep.} = \frac{\lambda_1}{2}X_1^4 + \frac{\lambda_2}{2}X_2^4 + \lambda_3 X_1^2 X_2^2 + \lambda_4 X_1^2 X_2^2 \rho^2 - |\lambda_5| X_1^2 X_2^2 \rho^2. \tag{3.7}$$

This potential has two solutions for the minimum, based on the sign of $\lambda_4 - |\lambda_5|$. In particular if $\lambda_4 - |\lambda_5| > 0$, the potential has a minimum at $\rho = 0$:

$$V_{4-\theta-indep.} = \frac{\lambda_1}{2}X_1^4 + \frac{\lambda_2}{2}X_2^4 + \lambda_3 X_1^2 X_2^2. \tag{3.8}$$

The minimum is then given by the partial derivatives of the potential $V_{4-\theta-indep.}$ with respect to the parameterized fields $X_1$ and $X_2$:

$$\frac{\partial V_{4-\theta-indep.}}{\partial X_1} = 2\lambda_1 X_1^3 + 2\lambda_3 X_1 X_2^2 = 0\,, \tag{3.9}$$

$$\frac{\partial V_{4-\theta-indep.}}{\partial X_2} = 2\lambda_2 X_2^3 + 2\lambda_3 X_2 X_1^2 = 0\,. \tag{3.10}$$

The solution of this system of equations, gives three bounds for the parameter $\lambda_1, \lambda_2$ and $\lambda_3$

$$\lambda_1 > 0\,, \tag{3.11}$$

$$\lambda_2 > 0\,, \tag{3.12}$$

$$\lambda_3 + \sqrt{\lambda_1 \lambda_2} > 0\,. \tag{3.13}$$

Inversely, if $\lambda_4 - |\lambda_5| < 0$, the potential has a minimum at $\rho = 1$:

$$V_{4-\theta-indep.} = \frac{\lambda_1}{2} X_1^4 + \frac{\lambda_2}{2} X_2^4 + \lambda_3 X_1^2 X_2^2 + \lambda_4 X_1^2 X_2^2 - |\lambda_5| X_1^2 X_2^2\,. \tag{3.14}$$

Again we find the minimum by computing the partial derivatives with respect to the fields:

$$\frac{\partial V_{4-\theta-indep.}}{\partial X_1} = 2\lambda_1 X_1^3 + 2\lambda_3 X_1 X_2^2 + 2(\lambda_4 - |\lambda_5|) X_1 X_2^2 = 0\,, \tag{3.15}$$

$$\frac{\partial V_{4-\theta-indep.}}{\partial X_2} = 2\lambda_2 X_2^3 + 2\lambda_3 X_2 X_1^2 + 2(\lambda_4 - |\lambda_5|) X_2 X_1^2 = 0\,. \tag{3.16}$$

The solution of this system of equations, gives a fourth bound

$$\lambda_3 + \lambda_4 - |\lambda_5| + \sqrt{\lambda_1 \lambda_2} > 0\,. \tag{3.17}$$

## 3.3 Global minimum

In a THDM it is possible that the vacuum in which we reside is metastable [26, 27]. Differently from the SM the vacuum structure of a THDM is much richer and can even, for certain parameter choices, have a vacuum which spontaneously breaks CP invariance. Historically, this is also one of the main motivations behind Lee's first proposal of this family of models. In other regions of the parameter space it is possible for the vacuum to break the electromagnetic U(1) gauge symmetry (to be avoided at all costs). Moreover, for large regions of parameter values, the vacuum is "normal", i.e. it breaks electroweak gauge invariance and preserves both the electromagnetic and CP symmetries. Lastly, the THDM may in general present two such "normal" minima. In this case, it could be that we do not reside in the "true" vacuum (global minimum), which in turn would mean that there is a second minimum in which the masses of the particles are completely

different from the known values. This would imply that we currently reside in a metastable vacuum. In [26] the authors derive a bound on the THDM parameters that guarantees the considered vacuum to be the global minimum, i.e. not a metastable vacuum. They define the "discriminant"

$$D = m_{12}^2 \left(m_{11}^2 - k^2 m_{22}^2\right)(t_\beta - k) \,, \tag{3.18}$$

where $k = (\lambda_1/\lambda_2)^{\frac{1}{4}}$, and show that if $D > 0$, then our vacuum is the global minimum of the potential (3.5). Therefore, to ensure that we reside in the global minimum of the potential, independent of the number of local minima, requiring $D > 0$ is a necessary and sufficient condition.

## 3.4 Unitarity bounds

### 3.4.1 Partial wave decomposition

At high energies, the scalar-scattering $S_1 S_2 \to S_3 S_4$ respects unitarity [13, 14, 28]. We can write the amplitude $\mathcal{M}$ of a scattering $S_1 S_2 \to S_3 S_4$, in terms of a partial wave decomposition

$$M(s,t,u) = 16\pi \sum_{l=0}^{\infty} (2l+1) P_l(\cos\theta) a_l(s) \,, \tag{3.19}$$

with $P_l$ the Legendre polynomials[2] and $t, u$ dependent on $\cos\theta$. Their orthogonality relation reads

$$\int_{-1}^{1} P_m(x) P_n(x)\, \mathrm{d}x = \frac{2}{2n+1}\delta_{nm} \,, \tag{3.20}$$

with $x = \cos(\theta)$.

For a $2 \to 2$ scattering process the differential cross section is given by [20]

$$\frac{\mathrm{d}\sigma}{\mathrm{d}\Omega} = \frac{1}{64\pi^2 s}|M|^2 \,. \tag{3.21}$$

By using the fact that in our case of a two-particle final state

$$\int \mathrm{d}\Omega = 2\pi \int \mathrm{d}\cos\theta \,, \tag{3.22}$$

and inserting (3.19) in (3.21) we obtain

$$\sigma = \frac{16\pi}{s} \sum_{l=0}^{\infty} (2l+1)|a_l(s)|^2 \,. \tag{3.23}$$

[2] $P_0(x) = 1$, $P_1(x) = x$, $P_2(x) = \frac{1}{2}(3x^2 - 1), \ldots$

By using the optical theorem for cross sections (given in Section 7.3 in [29])

$$2i\,\Im(M(k)) = \frac{i}{2}\underbrace{\int \frac{\mathrm{d}^3p_1}{(2\pi)^3}\frac{1}{2E_1}\frac{\mathrm{d}^3p_2}{(2\pi)^3}\frac{1}{2E_2}(2\pi)^4\delta^{(4)}(p_1+p_2-k)}_{\mathrm{dLips}_2}|M(k)|^2\,, \tag{3.24}$$

and the computed cross section we obtain

$$2i\,\Im(M(k)) = \frac{i}{2}2s\,\sigma \tag{3.25}$$

$$= \frac{i}{2}2s\frac{16\pi}{s}\sum_{l=0}^{\infty}(2l+1)|a_l(s)|^2\,, \tag{3.26}$$

where $2s$ is the flux factor. We insert (3.19) in $\Im(M(k))$ and obtain

$$|a_l|^2 = \Re(a_l)^2 + \Im(a_l)^2 = \Im(a_l)\,. \tag{3.27}$$

This is a so-called Argand circle. The equation is of the form

$$x^2 + y^2 = y\,. \tag{3.28}$$

We can make the substitution $y \to y' + \frac{1}{2}$ and obtain

$$x^2 + y'^2 = \frac{1}{4}\,. \tag{3.29}$$

This is the equation of a circle of radius $\frac{1}{2}$ centered at $y_0 = \frac{1}{2}$. Therefore, we obtain a bound on the partial wave decomposition of the matrix element

$$|\Re(a_l)| < \frac{1}{2} \qquad \text{for all l}\,. \tag{3.30}$$

The equation for the matrix element can be inverted to obtain the partial wave $a_l(s)$. We start from

$$\int_{-1}^{1}\sum_{l=0}^{\infty}P_l(\cos\theta)M(s,t,u)\,\mathrm{d}\cos\theta = \int_{-1}^{1}\sum_{l=0}^{\infty}P_l(\cos\theta)16\pi\sum_{l'=0}^{\infty}(2l'+1)P_{l'}(\cos\theta)a_{l'}(s)\,\mathrm{d}\cos\theta\,, \tag{3.31}$$

where we have inserted on the RHS (3.19). By exploiting the orthogonality relation (3.20) the RHS is trivially integrated. We obtain the final result

$$a_l(s) = \frac{1}{32\pi}\int_{-1}^{1}\mathrm{d}\cos\theta P_l(\cos\theta)M(s,t,u)\,. \tag{3.32}$$

According to the equivalence theorem, in the case of high energies the longitudinal components of the weak gauge boson states can be substituted with the corresponding Nambu-Goldstone boson state $\phi_i^{\pm}$, $h_i$ and $z_i$ $(i = 1, 2)$ [13, 30, 31]. Furthermore, it can be

shown that the dominant contribution to the amplitude of the $2 \to 2$ scattering is the one which is mediated by the quartic coupling. The contributions mediated by the trilinear couplings are shown to be suppressed on dimensional grounds. This in turn implies that if we restrict ourselves to the $J = 0$ case, the s-wave amplitude $a_0(s)$ takes the form

$$a_0(s) = \frac{1}{16\pi} Q \tag{3.33}$$

where $Q$ is the four point vertex for $S_1 S_2 \to S_3 S_4$. By direct insertion in (3.30), we obtain a bound on the quartic couplings

$$|Q(S_1 S_2 S_3 S_4)| \leq 8\pi \,. \tag{3.34}$$

The equivalence theorem states that in the high-energy limit, the amplitudes of a scattering process involving longitudinally polarized gauge bosons $V$ are asymptotically equal to the corresponding scalar amplitudes in which the gauge bosons are substituted by their corresponding Goldstone bosons. This is up to a correction of order $m_V/\sqrt{S}$. Therefore, the $S$ matrix expressed in terms of the mass eigenstate fields, can be transformed into an $S$ matrix for the non-physical fields $\phi_i^{\pm}, h_i$ and $z_i$. Thus, the unitarity constraints (3.34), can be computed by only considering scalar scatterings. All scalar scattering processes $S_1 S_2 \to S_3 S_4$, can be expressed as a $(22 \times 22)$ $S$ matrix. This matrix is in turn composed of 4 submatrices, which do not couple to each other due to CP-invariance and charge conjugation. The elements of these matrices are the quartic couplings which mediate the scattering processes. The eigenvalues of the 4 submatrices are then the quartic couplings $Q$, which must satisfy the bound (3.34).

Moreover, by imposing $|\lambda_i| \leq 4\pi$, we assure the potential (3.5) to be perturbative [13, 14, 17, 18].

### 3.4.2 Feynman rules

To derive the quartic couplings in the THDM, we insert the Two Higgs Doublet fields, in the notation used in [11] [3],

$$\phi_i = \begin{pmatrix} \omega_i^+ \\ v_i + \frac{h_i + i z_i}{\sqrt{2}} \end{pmatrix} , \tag{3.35}$$

directly into the potential

$$\begin{aligned} V = {} & m_{11}^2 (\Phi_1^\dagger \Phi_1) + m_{22}^2 (\Phi_2^\dagger \Phi_2) - m_{12}^2 (\Phi_1^\dagger \Phi_2 + h.c.) + \frac{\lambda_1}{2} (\Phi_1^\dagger \Phi_1)^2 + \frac{\lambda_2}{2} (\Phi_2^\dagger \Phi_2)^2 \\ & + \lambda_3 (\Phi_1^\dagger \Phi_1)(\Phi_2^\dagger \Phi_2) + \lambda_4 (\Phi_1^\dagger \Phi_2)(\Phi_2^\dagger \Phi_1) \\ & + \left[ \frac{\lambda_5}{2} (\Phi_1^\dagger \Phi_2)^2 + \lambda_6 (\Phi_1^\dagger \Phi_1)(\Phi_2^\dagger \Phi_2) + \lambda_7 (\Phi_2^\dagger \Phi_2)(\Phi_1^\dagger \Phi_2) + h.c. \right] . \end{aligned} \tag{3.36}$$

[3] We note that in the literature multiple notations are used for the Higgs doublets. In this work we use two different notations based on the notation used in the corresponding literature. We identify: $\phi_i^{\pm} \equiv \omega_i^{\pm}$, $\phi_i \equiv h_i$ and $a_i \equiv z_i$.

Using the identities

$$\Re(z) = \frac{z+\bar{z}}{2} \quad \text{and} \quad \Im(z) = \frac{z-\bar{z}}{2i}\,, \tag{3.37}$$

we obtain the sought after Feynman rules for the quartic couplings:

$$\begin{aligned}
\omega_1^+\omega_1^-\omega_1^+\omega_1^- &= \frac{\lambda_1}{2} & \omega_1^-\omega_1^+\omega_2^-\omega_2^+ &= \lambda_3+\lambda_4 \\
\omega_2^+\omega_2^-\omega_2^+\omega_2^- &= \frac{\lambda_2}{2} & h_2h_2h_2h_2 &= \frac{\lambda_2}{8} \\
h_1h_1\omega_1^-\omega_1^+ &= \frac{\lambda_1}{2} & h_1h_2\omega_1^+\omega_2^- &= \frac{\lambda_4+\lambda_5}{2} \\
h_1h_2\omega_1^-\omega_2^+ &= \frac{\lambda_4+\lambda_5}{2} & z_2h_1\omega_1^+\omega_2^- &= \frac{i}{2}(\lambda_4-\lambda_5) \\
\omega_1^+\omega_1^+\omega_2^-\omega_2^- &= \frac{\lambda_5}{2} & \omega_1^-\omega_1^-\omega_2^+\omega_2^+ &= \frac{\lambda_5}{2} \\
h_1h_1h_1h_1 &= \frac{\lambda_1}{8} & h_1h_1h_2h_2 &= \frac{1}{4}(\lambda_3+\lambda_4+\lambda_5) \\
h_2h_2\omega_1^-\omega_1^+ &= \frac{\lambda_3}{2} & h_2h_2\omega_2^-\omega_2^+ &= \frac{\lambda_2}{2} \\
h_1h_1\omega_2^-\omega_2^+ &= \frac{\lambda_3}{2} & z_2z_2\omega_1^+\omega_1^- &= \frac{\lambda_3}{2} \\
z_2h_1\omega_1^-\omega_2^+ &= -\frac{i}{2}(\lambda_4-\lambda_5) & z_2z_2h_2h_2 &= \frac{\lambda_2}{4} \\
z_1z_1z_1z_1 &= \frac{\lambda_1}{8} & z_1z_1h_2h_2 &= \frac{1}{4}(\lambda_3+\lambda_4-\lambda_5) \\
h_1h_1z_2z_2 &= \frac{1}{4}(\lambda_3+\lambda_4-\lambda_5) & z_1h_2\omega_1^-\omega_2^+ &= \frac{i}{2}(\lambda_4-\lambda_5) \\
z_1z_1\omega_2^-\omega_2^+ &= \frac{\lambda_3}{2} & z_1z_2\omega_1^+\omega_2^- &= \frac{1}{2}(\lambda_5+\lambda_4) \\
z_2z_2\omega_2^+\omega_2^- &= \frac{\lambda_2}{2} & z_2z_2z_2z_2 &= \frac{\lambda_2}{8} \\
z_2z_2z_1z_1 &= \frac{1}{4}(\lambda_3+\lambda_4+\lambda_5) & h_1h_1z_1z_1 &= \frac{\lambda_1}{4} \\
z_1h_2\omega_1^+\omega_2^- &= -\frac{i}{2}(\lambda_4-\lambda_5) & z_1z_1\omega_1^+\omega_1^- &= \frac{\lambda_1}{2} \\
z_1z_2h_1h_2 &= \lambda_5 & z_1z_2\omega_1^-\omega_2^+ &= \frac{1}{2}(\lambda_5+\lambda_4)
\end{aligned} \tag{3.38}$$

### 3.4.3 $S$ matrix

The first submatrix $\mathcal{M}_1$ contains all scattering processes whose initial and final states are one of the following: ($w_1^+w_2^-$,$w_2^+w_1^-$, $h_1z_2$, $h_2z_1$, $z_1z_2$, $h_1h_2$). Using the derived Feynman rules (3.38) (multiplied by the appropriate symmetry factor) for the quartic couplings,

one can see that by direct insertion

$$\mathcal{M}_1 = \begin{pmatrix} \lambda_{34}^+ & 2\lambda_5 & \frac{\lambda_{45}^+}{2} & i\frac{\lambda_{45}^-}{2} & -i\frac{\lambda_{45}^-}{2} & \frac{\lambda_{45}^+}{2} \\ 2\lambda_5 & \lambda_{34}^+ & \frac{\lambda_{45}^+}{2} & -i\frac{\lambda_{45}^-}{2} & i\frac{\lambda_{45}^-}{2} & \frac{\lambda_{45}^+}{2} \\ \frac{\lambda_{45}^+}{2} & \frac{\lambda_{45}^+}{2} & \lambda_3+\lambda_4+\lambda_5 & 0 & 0 & \lambda_5 \\ -i\frac{\lambda_{45}^-}{2} & i\frac{\lambda_{45}^-}{2} & 0 & \lambda_3+\lambda_4-\lambda_5 & \lambda_5 & 0 \\ i\frac{\lambda_{45}^-}{2} & -i\frac{\lambda_{45}^-}{2} & 0 & \lambda_5 & \lambda_3+\lambda_4-\lambda_5 & 0 \\ \frac{\lambda_{45}^+}{2} & \frac{\lambda_{45}^+}{2} & \lambda_5 & 0 & 0 & \lambda_3+\lambda_4+\lambda_5 \end{pmatrix}, \tag{3.39}$$

where we have used the abbreviation $\lambda_{ij}^{\pm} = \lambda_i \pm \lambda_j$. With the help of Mathematica we compute the eigenvalues (EV) of the $\mathcal{M}_1$ matrix:

$$a_1 = \lambda_3 + \lambda_4\,, \tag{3.40}$$
$$a_2 = \lambda_3 - \lambda_5\,, \tag{3.41}$$
$$a_3 = \lambda_3 + \lambda_5\,, \tag{3.42}$$
$$a_\pm = \lambda_3 + 2\lambda_4 \pm 3\lambda_5\,. \tag{3.43}$$

The second submatrix $\mathcal{M}_2$ corresponds to the scatterings with one of the following initial and final state: $(w_1^+w_1^-,\, w_2^+w_2^-,\, \frac{z_1z_1}{\sqrt{2}},\, \frac{z_2z_2}{\sqrt{2}},\, \frac{h_1h_1}{\sqrt{2}},\, \frac{h_2h_2}{\sqrt{2}})$. The factor $\frac{1}{\sqrt{2}}$ accounts for the statistics of identical particles. Again, by direct insertion of the quartic couplings, we obtain

$$\mathcal{M}_2 = \begin{pmatrix} 2\lambda_1 & \lambda_{34}^+ & \frac{\lambda_1}{\sqrt{2}} & \frac{\lambda_3}{\sqrt{2}} & \frac{\lambda_1}{\sqrt{2}} & \frac{\lambda_3}{\sqrt{2}} \\ \lambda_{34}^+ & 2\lambda_2 & \frac{\lambda_3}{\sqrt{2}} & \frac{\lambda_2}{\sqrt{2}} & \frac{\lambda_3}{\sqrt{2}} & \frac{\lambda_2}{\sqrt{2}} \\ \frac{\lambda_1}{\sqrt{2}} & \frac{\lambda_3}{\sqrt{2}} & \frac{3\lambda_1}{2} & \frac{1}{2}(\lambda_3+\lambda_4+\lambda_5) & \frac{\lambda_1}{2} & \frac{1}{2}(\lambda_3+\lambda_4-\lambda_5) \\ \frac{\lambda_3}{\sqrt{2}} & \frac{\lambda_2}{\sqrt{2}} & \frac{1}{2}(\lambda_3+\lambda_4+\lambda_5) & \frac{3\lambda_2}{2} & \frac{1}{2}(\lambda_3+\lambda_4-\lambda_5) & \frac{\lambda_2}{2} \\ \frac{\lambda_1}{\sqrt{2}} & \frac{\lambda_3}{\sqrt{2}} & \frac{\lambda_1}{2} & \frac{1}{2}(\lambda_3+\lambda_4-\lambda_5) & \frac{3\lambda_1}{2} & \frac{1}{2}(\lambda_3+\lambda_4+\lambda_5) \\ \frac{\lambda_3}{\sqrt{2}} & \frac{\lambda_2}{\sqrt{2}} & \frac{1}{2}(\lambda_3+\lambda_4-\lambda_5) & \frac{\lambda_2}{2} & \frac{1}{2}(\lambda_3+\lambda_4+\lambda_5) & \frac{3\lambda_2}{2} \end{pmatrix}. \tag{3.44}$$

The EV of $\mathcal{M}_2$ are

$$b_1 = \frac{1}{2}\left(3\lambda_1+3\lambda_2+\sqrt{9(\lambda_1-\lambda_2)^2+4(2\lambda_3+\lambda_4)^2}\right), \tag{3.45}$$
$$b_2 = \frac{1}{2}\left(3\lambda_1+3\lambda_2-\sqrt{9(\lambda_1-\lambda_2)^2+4(2\lambda_3+\lambda_4)^2}\right), \tag{3.46}$$
$$b_\pm = \frac{1}{2}\left(\lambda_1+\lambda_2\pm\sqrt{(\lambda_1-\lambda_2)^2+4\lambda_4^2}\right), \tag{3.47}$$
$$f_\pm = \frac{1}{2}\left(\lambda_1+\lambda_2\pm\sqrt{(\lambda_1-\lambda_2)^2+4\lambda_5^2}\right). \tag{3.48}$$

The third submatrix $\mathcal{M}_3$ corresponds to the scatterings with one of the following initial and final state: $(h_1z_1,\, h_2z_2)$. We obtain for the scattering matrix

$$\mathcal{M}_3 = \begin{pmatrix} \lambda_1 & \lambda_5 \\ \lambda_5 & \lambda_2 \end{pmatrix}. \tag{3.49}$$

The two eigenvalues read

$$c_\pm = f_\pm \,. \tag{3.50}$$

The fourth submatrix $\mathcal{M}_4$ corresponds to the scatterings with one of the following initial and final state: $(h_1\omega_1^+,\, z_1\omega_1^+,\, h_2\omega_1^+,\, z_2\omega_1^+,\, h_1\omega_2^+,\, z_1\omega_2^+,\, h_2\omega_2^+,\, z_2\omega_2^+)$. The matrix reads

$$\mathcal{M}_4 = \begin{pmatrix} \lambda_1 & 0 & 0 & 0 & 0 & 0 & \frac{\lambda_{45}^+}{2} & -i\frac{\lambda_{45}^-}{2} \\ 0 & \lambda_1 & 0 & 0 & 0 & 0 & i\frac{\lambda_{45}^-}{2} & \frac{\lambda_{45}^+}{2} \\ 0 & 0 & \lambda_3 & 0 & \frac{\lambda_{45}^+}{2} & i\frac{\lambda_{45}^-}{2} & 0 & 0 \\ 0 & 0 & 0 & \lambda_3 & -i\frac{\lambda_{45}^-}{2} & \frac{\lambda_{45}^+}{2} & 0 & 0 \\ 0 & 0 & \frac{\lambda_{45}^+}{2} & i\frac{\lambda_{45}^-}{2} & \lambda_3 & 0 & 0 & 0 \\ 0 & 0 & -i\frac{\lambda_{45}^-}{2} & \frac{\lambda_{45}^+}{2} & 0 & \lambda_3 & 0 & 0 \\ \frac{\lambda_{45}^+}{2} & -i\frac{\lambda_{45}^-}{2} & 0 & 0 & 0 & 0 & \lambda_2 & 0 \\ i\frac{\lambda_{45}^-}{2} & \frac{\lambda_{45}^+}{2} & 0 & 0 & 0 & 0 & 0 & \lambda_2 \end{pmatrix} , \tag{3.51}$$

The 8 eigenvalues for $\mathcal{M}_4$ are

$$d_1 = a_1 \,, \tag{3.52}$$
$$d_2 = a_2 \,, \tag{3.53}$$
$$d_3 = a_3 \,, \tag{3.54}$$
$$d_\pm = b_\pm \,, \tag{3.55}$$
$$g_\pm = f_\pm \,, \tag{3.56}$$
$$d_6 = \lambda_3 - \lambda_4 \,. \tag{3.57}$$

The fifth and last submatrix $\mathcal{M}_5$ corresponds to the possible scatterings of of the following initial and final states: $(\frac{\omega_1^+\omega_1^+}{\sqrt{2}},\, \frac{\omega_2^+\omega_2^+}{\sqrt{2}},\, \omega_1^+\omega_2^+)$. The matrix reads

$$\mathcal{M}_5 = \begin{pmatrix} \lambda_1 & \lambda_5 & 0 \\ \lambda_5 & \lambda_2 & 0 \\ 0 & 0 & \lambda_{34}^+ \end{pmatrix} , \tag{3.58}$$

and has the following three eigenvalues

$$e_1 = a_1 \,, \tag{3.59}$$
$$e_\pm = f_\pm \,. \tag{3.60}$$

We can now insert the expressions for the parameters $\lambda_{1,2,3,4}$ (3.1) into the eigenvalues (EV) of the five submatrices and check the validity of the bound (3.34),

$$|EV| \leq 8\pi \,. \tag{3.61}$$

## 3.5 Oblique parameters

The so-called oblique parameters have been introduced by Peskin and Takeuchi (1990) [32], as a set of three measurable quantities S, T and U, that parameterize the new physics contributions to electroweak radiative corrections in beyond SM models (BSM). They are defined such that $S = T = U = 0$ corresponds to the SM. The parameter T is closely related to the known $\rho$ parameter[4] in the electroweak theory by $\rho = 1 + \alpha T$. For further insight into the relations between the oblique parameters and SM observables, see Eqs. 3.13 in [32]. The oblique parameters are defined in terms of the transverse part of the gauge boson two-point functions,

$$\bar{\alpha}T := \frac{\Pi^{\text{new}}_{WW}(0)}{m_W^2} - \frac{\Pi^{\text{new}}_{ZZ}(0)}{m_Z^2}\,, \tag{3.62}$$

$$\frac{\bar{\alpha}}{4\bar{s}_Z^2\bar{c}_Z^2}S := \frac{\Pi^{\text{new}}_{ZZ}(m_Z^2) - \Pi^{\text{new}}_{ZZ}(0)}{m_Z^2} - \left(\frac{\bar{c}_w^2 - \bar{s}_w^2}{\bar{c}_w\bar{s}_w}\right)\frac{\Pi^{\text{new}}_{Z\gamma}(m_W^2)}{m_W^2} - \frac{\Pi^{\text{new}}_{\gamma\gamma}(m_Z^2)}{m_Z^2}\,, \tag{3.63}$$

$$\frac{\bar{\alpha}}{4\bar{s}_Z^2\bar{c}_Z^2}(S+U) := \frac{\Pi^{\text{new}}_{WW}(m_W^2) - \Pi^{\text{new}}_{WW}(0)}{m_W^2} - \left(\frac{\bar{c}_w^2}{\bar{s}_w}\right)\frac{\Pi^{\text{new}}_{Z\gamma}(m_W^2)}{m_W^2} - \frac{\Pi^{\text{new}}_{\gamma\gamma}}{m_W^2}\,, \tag{3.64}$$

where we use the definitions $\bar{s}_W := \sin\theta_w(m_Z), \bar{c}_W := \cos\theta_w(m_Z)$ and $\bar{\alpha} := \frac{\bar{g}^2\bar{s}_Z^2}{4\pi}$ defined in the $\overline{\text{MS}}$ scheme evaluated at $m_Z$. The $\Pi^{\text{new}}_{V_aV_b}$ are the new contributions to the one loop vacuum polarization functions. In this work the new contributions stems from the additional Higgs bosons of the THDM. In the case that the new physics energy scale is significantly larger than $m_Z$, we can make a linear approximation of the new one loop contributions [12]

$$\Pi^{\text{new}}_{ij}(q^2) \approx A_{ij}(0) + q^2F_{ij}(q^2)\,. \tag{3.65}$$

Moreover, electromagnetic gauge invariance guarantees

$$A_{\gamma\gamma}(0) = A_{Z\gamma}(0) = 0\,. \tag{3.66}$$

Using this linear approximation we may rewrite (3.62),(3.63), (3.64) as

$$\alpha T = \frac{A_{WW}(0)}{m_W^2} - \frac{A_{ZZ}(0)}{m_Z^2}\,, \tag{3.67}$$

$$\frac{g^2}{16\pi c_w^2}S = F_{ZZ}(m_Z^2) - F_{\gamma\gamma}(m_Z^2) - \left(\frac{c_w^2 - s_w^2}{s_wc_w}\right)F_{Z\gamma}(m_Z^2)\,, \tag{3.68}$$

$$\frac{g^2}{16\pi}(S+U) = F_{WW}(m_W^2) - F_{\gamma\gamma}(m_W^2) - \frac{c_w}{s_w}F_{Z\gamma}(m_W^2)\,. \tag{3.69}$$

Here we have dropped the bars for convenience. To compute the oblique parameter in the THDM we compute the one-loop gauge polarization functions in which the Higgs bosons appear in the loop. We then subtract the contributions of the SM Higgs boson of mass

[4] $\rho = \frac{m_W^2}{m_Z^2\cos\theta_w{}^2}$

$m_{h^0} = 125$ GeV. By closely following [12], we calculate the THDM contributions to $S$, $T$ and $U$. The contributions to S are given by

$$S = \frac{1}{\pi m_Z^2}\Bigg\{ \sum_{k=1}^{3} q_{k1}^2 \Big[\mathcal{B}_{22}(m_Z^2; m_Z^2, m_k^2) - m_Z^2 \mathcal{B}_0(m_Z^2; m_Z^2, m_k^2)\Big] \tag{3.70}$$
$$+ q_{11}^2 \mathcal{B}_{22}(m_Z^2; m_2^2, m_3^2) + q_{21}^2 \mathcal{B}_{22}(m_Z^2; m_1^2, m_3^2) + q_{31}^2 \mathcal{B}_{22}(m_Z^2; m_1^2, m_2^2)$$
$$- \mathcal{B}_{22}(m_Z^2; m_{H^\pm}^2, m_{H^\pm}^2) - \mathcal{B}_{22}(m_Z^2; m_1^2, m_\phi^2) + m_Z^2 \mathcal{B}_0(m_Z^2; m_Z^2, m_\phi^2)\Bigg\},$$

where

$$\mathcal{B}_{22}(q^2; m_1^2, m_2^2) \equiv B_{22}(q^2; m_1^2, m_2^2) - B_{22}(0; m_1^2, m_2^2)\,, \tag{3.71}$$
$$\mathcal{B}_0(q^2; m_1^2, m_2^2) \equiv B_0(q^2; m_1^2, m_2^2) - B_0(0; m_1^2, m_2^2)\,. \tag{3.72}$$

$m_k$ are the masses of the neutral Higgs bosons $h^0$, $H^0$ and $A^0$. The two point loop integrals are defined in [33]. We evaluate the integrals numerically in dimensional regularization using

$$B_{22}(q^2; m_1^2, m_2^2) = \frac{1}{4}(\Delta + 1)\Big[m_1^2 + m_2^2 - \frac{1}{3}q^2\Big] - \frac{1}{2}\int_0^1 dx X \ln\left(X - i\epsilon\right), \tag{3.73}$$

$$B_0(q^2; m_1^2, m_2^2) = \Delta - \int_0^1 dx \ln\left(X - i\epsilon\right), \tag{3.74}$$

with

$$X \equiv m_1^2 x + m_2^2(1-x) - q^2 x(1-x)\,, \tag{3.75}$$

$$\Delta \equiv \frac{2}{4-d} + \ln(4\pi) - \gamma\,, \tag{3.76}$$

in $d$ space-time dimensions. We note that the $B_0$ and $B_{22}$ functions are symmetric in the second and third arguments

$$B_{22}(q^2; m_1^2, m_2^2) = B_{22}(q^2; m_2^2, m_1^2)\,, \tag{3.77}$$
$$B_0(q^2; m_1^2, m_2^2) = B_0(q^2; m_2^2, m_1^2)\,. \tag{3.78}$$

Moreover, we define the function $\mathcal{F}$ as

$$\mathcal{F}(m_1^2, m_2^2) \equiv \frac{1}{2}(m_1^2 + m_2^2) - \frac{m_1^2 m_2^2}{m_1^2 - m_2^2}\ln\left(\frac{m_1^2}{m_2^2}\right), \tag{3.79}$$

and

$$\mathcal{F}(m_1^2, m_2^2) = (m_2^2, m_1^2)\,. \tag{3.80}$$

The THDM contributions to T and U are given by

$$T = \frac{1}{16\pi m_W^2 s_W^2}\Bigg\{ \sum_{k=1}^{3} |q_{k2}|^2 \mathcal{F}(m_{H^\pm}^2, m_k^2) - q_{11}^2 \mathcal{F}(m_2^2, m_3^2) - q_{21}^2 \mathcal{F}(m_1^2, m_3^2) \tag{3.81}$$
$$- q_{31}^2 \mathcal{F}(m_1^2, m_2^2) + \sum_{k=1}^{3} q_{k1}^2 \Big[ \mathcal{F}(m_W^2, m_k^2) - \mathcal{F}(m_Z^2, m_k^2) - 4m_W^2 B_0(0; m_W^2, m_k^2) + 4m_Z^2 B_0(0; m_Z^2, m_k^2) \Big]$$
$$+ \mathcal{F}(m_Z^2, m_\phi^2) - \mathcal{F}(m_W^2, m_\phi^2) + 4m_W^2 B_0(0; m_W^2, m_\phi^2) - 4m_Z^2 B_0(0; m_Z^2, m_\phi^2) \Bigg\},$$

$$U = -S + \frac{1}{\pi m_W^2}\Bigg\{ - \sum_{k=1}^{3} q_{k1}^2 m_W^2 \mathcal{B}_0(m_W^2; m_W^2, m_k^2) + m_W^2 \mathcal{B}_0(m_W^2; m_W^2, m_\phi^2) \tag{3.82}$$
$$- \mathcal{B}_{22}(m_W^2; m_W^2, m_\phi^2) + \sum_{k=1}^{3} \Big[ q_{k1}^2 \mathcal{B}_{22}(m_W^2; m_W^2, m_k^2) + |q_{k2}|^2 \mathcal{B}_{22}(m_W^2; m_{H^\pm}^2, m_k^2) \Big]$$
$$- 2\mathcal{B}_{22}(m_W^2; m_{H^\pm}^2, m_{H^\pm}^2) \Bigg\}.$$

In this study we focus on the CP-conserving THDMs. Therefore, we identify the values of $q_{k1}$ and $q_{k2}$ and the corresponding neutral Higgs boson masses $m_k$ in the CP-conserving limit [34]. Depending on the mass ordering of the Higgs bosons, three cases can be identified [12]. However, the oblique parameters $S$, $T$ and $U$ do not depend on which case is employed to compute the $q_{kl}$. These factors are related to the angles $\alpha$ and $\beta$ as indicated in [12]. By inserting the values for the $q_{kl}$ parameters from any of the three cases in (3.83), (3.71), (3.73), (3.75), (3.77), (3.79) and (3.81), we obtain for the oblique parameters

$$S = \frac{1}{\pi m_Z^2}\Bigg\{ - \mathcal{B}_{22}(m_Z^2; m_{H^\pm}^2, m_{H^\pm}^2) + \sin^2(\beta-\alpha)\mathcal{B}_{22}(m_Z^2; m_{H^0}^2, m_{A^0}^2) \tag{3.83}$$
$$+ \cos^2(\beta-\alpha)\Big[ \mathcal{B}_{22}(m_Z^2; m_{h^0}^2, m_{A^0}^2) + \mathcal{B}_{22}(m_Z^2; m_Z^2, m_{H^0}^2) - \mathcal{B}_{22}(m_Z^2; m_Z^2, m_{h^0}^2)$$
$$- m_Z^2 \mathcal{B}_0(m_Z^2; m_Z^2, m_{H^0}^2) + m_Z^2 \mathcal{B}_0(m_Z^2; m_Z^2, m_{h^0}^2) \Big] \Bigg\},$$

$$T = \frac{1}{16\pi m_W^2 s_W^2}\Bigg\{ \mathcal{F}(m_{H^\pm}^2, m_{A^0}^2) + \sin^2(\beta-\alpha)\Big[ \mathcal{F}(m_{H^\pm}^2, m_{H^0}^2) - \mathcal{F}(m_{A^0}^2, m_{H^0}^2) \Big] \tag{3.84}$$
$$+ \cos^2(\beta-\alpha)\Big[ \mathcal{F}(m_{H^\pm}^2, m_{h^0}^2) - \mathcal{F}(m_{A^0}^2, m_{h^0}^2) + \mathcal{F}(m_W^2, m_{H^0}^2) - \mathcal{F}(m_W^2, m_{h^0}^2) - \mathcal{F}(m_Z^2, m_{H^0}^2)$$
$$+ \mathcal{F}(m_Z^2, m_{h^0}^2) + 4m_Z^2 B_0(0; m_Z^2, m_{H^0}^2) - 4m_Z^2 B_0(0; m_Z^2, m_{h^0}^2) - 4m_W^2 B_0(0; m_W^2, m_{H^0}^2)$$
$$+ 4m_W^2 B_0(0; m_W^2, m_{h^0}^2) \Big] \Bigg\},$$

$$U = -S + \frac{1}{\pi m_W^2}\Bigg\{\mathcal{B}_{22}(m_W^2; m_{H^\pm}^2, m_{A^0}^2) - 2\mathcal{B}_{22}(m_W^2; m_{H^\pm}^2, m_{H^\pm}^2) + \sin^2(\beta-\alpha) \tag{3.85}$$
$$\mathcal{B}_{22}(m_W^2; m_{H^\pm}^2, m_{H^0}^2) + \cos^2(\beta-\alpha)\Big[\mathcal{B}_{22}(m_W^2; m_{h^0}^2, m_{H^\pm}^2) + \mathcal{B}_{22}(m_W^2; m_W^2, m_{H^0}^2)$$
$$- \mathcal{B}_{22}(m_W^2; m_W^2, m_{h^0}^2) - m_W^2\mathcal{B}_0(m_W^2; m_W^2, m_{H^0}^2) - m_W^2\mathcal{B}_0(m_W^2; m_W^2, m_{h^0}^2)\Big]\Bigg\}.$$

We numerically calculate the oblique parameters and compare them with the experimental global fit values

$$S = 0.02 \pm 0.10 \quad , \quad T = 0.07 \pm 0.12 \quad \text{and} \quad U = 0.00 \pm 0.09\,. \tag{3.86}$$

We note that due to the absence of fermions in the THDM contributions to the oblique parameters, these results hold for all THD models.

### 3.5.1 Examples of one-loop polarization functions

We present two explicit derivations of the one-loop polarization functions $W^+ \to h^0 H^\pm \to W^+$ and $\gamma \to H^+H^- \to \gamma$ contributing to $A_{WW}(0)$ and $\Pi_{\gamma\gamma}(m^2_{Z^0})$ respectively. A complete derivation is presented in [12].

#### Loop integrals

We define the loop integrals following the convention given in [35]

$$\int \frac{d^4k}{(2\pi)^4} \frac{1}{k^2 - m^2} = \frac{i}{16\pi^2} A_0(m^2)\,, \tag{3.87}$$

$$\int \frac{d^4k}{(2\pi)^4} \frac{1}{(k^2 - m_1^2)[(k+q)^2 - m_2^2]} = \frac{i}{16\pi^2} B_0(q^2; m_1^2, m_2^2)\,, \tag{3.88}$$

$$\int \frac{d^4k}{(2\pi)^4} \frac{k^\mu k^\nu}{(k^2 - m_1^2)[(k+q)^2 - m_2^2]} = \frac{i}{16\pi^2} g^{\mu\nu} B_{22}(q^2; m_1^2, m_2^2)\,, \tag{3.89}$$

and make use of the following relations and definitions

$$B_0(0; m_1^2, m_2^2) = \frac{A_0(m_1^2) - A_0(m_2^2)}{m_1^2 - m_2^2}\,, \tag{3.90}$$

$$4B_{22}(0; m_1^2, m_2^2) = \mathcal{F}(m_1^2, m_2^2) + A_0(m_1^2) + A_0(m_2^2)\,, \tag{3.91}$$

$$\mathcal{F}(m_1^2, m_2^2) := \frac{1}{2}(m_1^2 + m_2^2) - \frac{m_1^2 m_2^2}{m_1^2 - m_2^2} \ln\left(\frac{m_1^2}{m_2^2}\right). \tag{3.92}$$

We follow the definition of the self-energy coefficients of the vector particles given in [36].

**Example of one-loop contribution to $A_{WW}(0)$: $W^+ \to h^0 H^\pm \to W^+$**

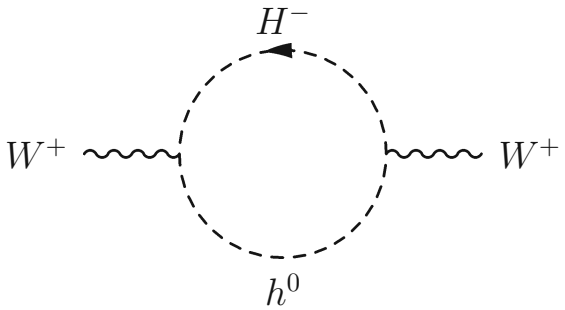


Figure 3.1: Feynman diagram for the $W^+ \to h^0 H^\pm \to W^+$ channel one-loop contribution to $W^+$, in the THDM. All momenta are in time direction from left to right.

We evaluate the matrix element for $W^+ \to h^0 H^\pm \to W^+$ by using the Feynman rule [12]

$$C(W^+, H^\pm, h^0) = -\frac{1}{2} i g q_{12} (p_1 + p_2)^\mu \,, \tag{3.93}$$

where $p_1$ is the momentum of the Higgs boson $H^\pm$ and $p_2$ of $h^0$. Therefore, the one-loop contribution is given by

$$M = -\int \frac{d^4q}{(2\pi)^4} \left( \frac{q_{12}^2}{4} g^2 (p_1 + p_2)_\mu (p_1 + p_2)_\nu \epsilon^{*\mu}(k) \epsilon^\nu(k) \right) \frac{1}{(p_1^2 - m_{H^+}^2)(p_2^2 - m_{h^0}^2)} \,. \tag{3.94}$$

We define the momenta in the loop as $p_1 = k + q$ and $p_2 = q$. After inserting these definitions and using $\epsilon(k)^\mu k_\mu = 0$ we obtain

$$M = -\int \frac{d^4q}{(2\pi)^4} \left( \frac{q_{12}^2}{4} g^2 \right) \epsilon^{*\mu}(k) \epsilon^\nu(k) \frac{q_\mu q_\nu}{[(k+q)^2 - m_{H^\pm}^2][q^2 - m_{h^0}^2]} \,. \tag{3.95}$$

With the loop integral definitions (3.87) we can rewrite (3.95) as

$$M = -g_{\mu\nu} \frac{i}{16\pi^2} g^2 |q_{12}|^2 B_{22}(0; m_{H^\pm}^2, m_{h^0}^2) \epsilon^{*\mu}(k) \epsilon^\nu(k) \,. \tag{3.96}$$

By comparison of the coefficients, see [36] Section 3.2, we get

$$\Pi_{WW}(k^2) = \frac{1}{16\pi^2} g^2 |q_{12}|^2 B_{22}(0; m_{H^\pm}^2, m_{h^0}^2) \,, \tag{3.97}$$

for the loop with $h^0$ and $H^-$.

**Example of one-loop contribution to $\Pi_{\gamma\gamma}(m_{Z^0}^2)$: $\gamma \to H^+ H^- \to \gamma$**

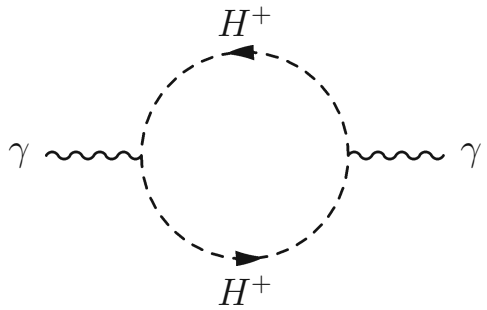


Figure 3.2: Feynman diagram for the $\gamma \to H^+ H^- \to \gamma$ channel one-loop contribution to $\gamma$, in the THDM. All momenta are in time direction from left to right.

Similarly to the first example, we evaluate the matrix element for $\gamma \to H^+H^- \to \gamma$ by using the Feynman rule for the coupling [12],

$$C(\gamma, H^\pm, H^\pm) = igs_W(p_1 + p_2)^\mu \,, \tag{3.98}$$

where $p_1$ and $p_2$ are the momenta of the two Higgs bosons $H^\pm$. Therefore, the one-loop contribution is given by

$$M = -\int \frac{d^4q}{(2\pi)^4} \frac{1}{(p_1^2 - m_{H^\pm}^2)(p_2^2 - m_{H^\pm}^2)} g^2 s_W^2 \epsilon^\mu(k)(p_1 + p_2)_\mu \epsilon^{*\nu}(k)(p_1 + p_2)_\nu \,. \tag{3.99}$$

We define the momenta in the loop as $p_1 = k + q$ and $p_2 = q$. After inserting these definitions and using $\epsilon(k)^\mu k_\mu = 0$ we obtain

$$M = -\int \frac{d^4q}{(2\pi)^4} \left(4g^2 s_W^2\right) \frac{q_\mu q_\nu}{[(k+q)^2 - m_{H^\pm}^2][q^2 - m_{h^0}^2]} \epsilon^\mu(k)\epsilon^{*\nu}(k) \,. \tag{3.100}$$

With the loop integral definitions (3.87) we can rewrite (3.100) as

$$M = -g_{\mu\nu} \frac{i}{4\pi^2} g^2 s_W^2 B_{22}(m_{Z^0}^2; m_{H^\pm}^2, m_{H^\pm}^2) \epsilon^\mu(k)\epsilon^{*\nu}(k) \,, \tag{3.101}$$

where we have evaluated the expression at $q^2 = m_{Z^0}^2$. By comparison of the coefficients, see [36] Section 3.2, we get

$$\Pi_{\gamma\gamma}(k^2) = \frac{1}{4\pi^2} g^2 s_W^2 B_{22}(m_{Z^0}^2; m_{H^\pm}^2, m_{H^\pm}^2) \,, \tag{3.102}$$

for the loop with $h^0$ and $H^-$.

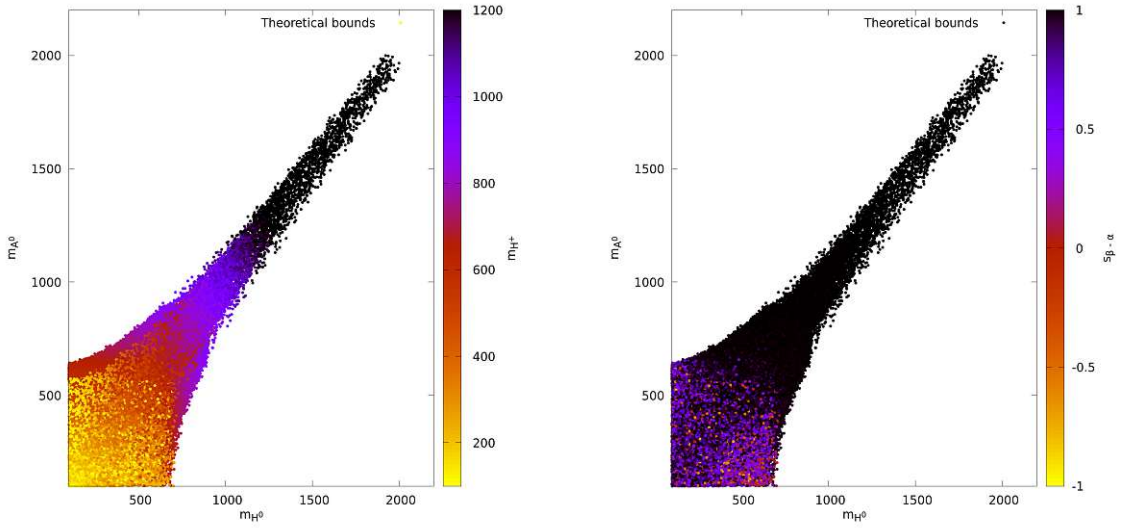


(a) (b)

Figure 3.3: Scatter plots of $m_{A^0}$[GeV] and $m_{H^0}$[GeV] satisfying the constraints of vacuum stability, unitarity, perturbativity, and the oblique parameters for 100 GeV $\leq m_{H^\pm} \leq$ 2000 GeV (a), and $-1 \leq s_{\beta-\alpha} \leq 1$ (b).

## 3.6 Numerical analysis

In this section we present the numerical results obtained for the vacuum stability, global minimum, unitarity and oblique parameters bounds[5]. Due to the complex nature of the obtained bounds on the 7 parameters of the model, we perform a numerical study of the parameter sets allowed by the considered theoretical bounds. We perform the scan using a self-developed *python* code. We scanned $\approx 25 \cdot 10^9$ points of which 270759 points respected all theoretical bounds. We impose a range for the input parameters $(s_\alpha, t_\beta, m_{H^0}, m_{A^0}, m_{H^\pm}, \lambda_5)$, randomly pick a combination of these parameters and then numerically check whether the selected set of parameters respects all bounds. The mixing angles $\alpha$ and $\beta$ can range respectively between $s_\alpha \in [-1.0, 1.0]$ and $t_\beta \in [0.1, 40.0]$. Perturbativity constraints the range of the parameter $\lambda_5$ to $\lambda_5 \in [-4\pi, 4\pi]$. In the literature the perturbativity bound on the parameters $\lambda_i$ is often relaxed to $\lambda_i \in [-8\pi, 8\pi]$ [13, 14]. We perform two parameter scans for both perturbativity constraints. We observe no substantial difference. However, we choose the more theoretically grounded and conservative $4\pi$ bound. For the masses of the neutral Higgs bosons $H^0$ and $A^0$ we impose an upper limit of 3 TeV.

In Fig. 3.3a we observe that the neutral Higgs bosons $H^0$ and $A^0$ cannot simultaneously take values below $\approx 500$ GeV for $m_{H^\pm} \gtrsim 550$ GeV. The highest density of allowed parameter sets is in the region where $100 \lesssim m_{A^0} \lesssim 700$ GeV and $100 \lesssim m_{H^0} \lesssim 700$ GeV.

[5]Historically the oblique parameter bounds are counted as theoretical bounds, even though they depend on experimental measurements.

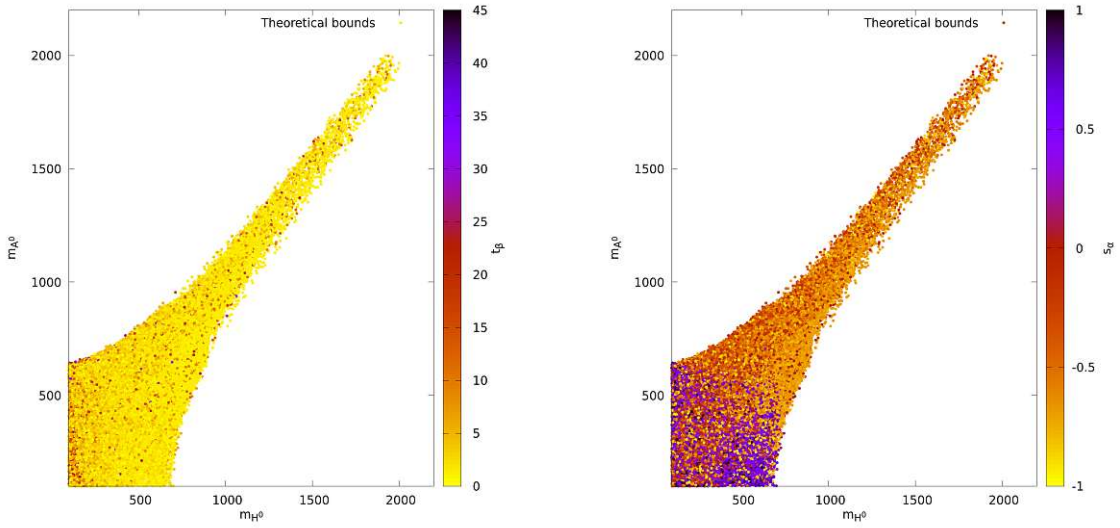


(a) (b)

Figure 3.4: Scatter plots of $m_{A^0}$[GeV] and $m_{H^0}$[GeV] satisfying the constraints of vacuum stability, unitarity, perturbativity, and the oblique parameters for $0 \leq t_\beta \leq 40$ (a) and $-1.0 \leq s_\alpha \leq 1.0$ (b).

Furthermore, we observe an almost linear dependence between the masses of the $A^0$ and $H^0$ Higgs bosons for $m_{A^0} \gtrsim 700$ GeV and $m_{H^0} \gtrsim 700$ GeV, $m_{A^0} \sim m_{H^0}$, as well as a continuous grow of the $H^+$ Higgs boson mass for growing $m_{H^0}$ and $m_{A^0}$. Fig. 3.3b shows that for $m_{A^0} \gtrsim 700$ GeV and $m_{H^0} \gtrsim 700$, $s_{\beta-\alpha}$ is close to 1 for the vast majority of parameter sets [37]. This in turn implies that these sets are close to the alignment limit $s_{\beta-\alpha} = 1$. The parameter sets with $100 \lesssim m_{A^0} \lesssim 700$ GeV and $100 \lesssim m_{H^0} \lesssim 700$ GeV show a significant deviation from the alignment limit. Some parameter sets even show values for $s_{\beta-\alpha}$ close to 0.5. Moreover, for growing $m_{H^0}$ and $m_{A^0}$ we observe a diminishing density of allowed points. Above masses of 2000 GeV for any of the Higgs bosons we do not find any allowed sets. However, we note that it could be possible to observe exotic points in this region of the parameter space. At the same time, the parameter $t_\beta$ shows almost uniformly distributed values between 0.1 and 10.0 for all Higgs boson masses $m_{H^0}$ and $m_{A^0}$, see Fig. 3.4a. For $100 \lesssim m_{A^0} \lesssim 700$ GeV and $100 \lesssim m_{H^0} \lesssim 700$ GeV, we observe that the parameter $s_\alpha$, takes values approx. between 0. and 1.0, whereas for the other allowed regions $s_\alpha$ is for the majority of the allowed points between 0 and -0.7, see Fig. 3.4b. This means that for growing $A^0$ and $H^0$ Higgs boson masses, the mixing angle $s_\alpha$ changes sign for the majority of allowed parameter sets.

When plotting $t_\beta$ and $s_\alpha$ as a function of $\lambda_5$ we observe a sharp peak around $s_\alpha = 0$, see Fig. 3.5a, for all $t_\beta$ values that we scan. The parameter $\lambda_5$ takes values approximately between -5 and 5. Moreover, the scan shows a high density of points for $t_\beta \lesssim 10$ for all $s_\alpha$, that diminishes for growing $t_\beta$, see Fig. 3.5a. The same plot, but with $s_\alpha$ substituted by $s_{\beta-\alpha}$, shows that the vast majority of allowed points have $s_{\beta-\alpha} \approx 1$ (as seen in

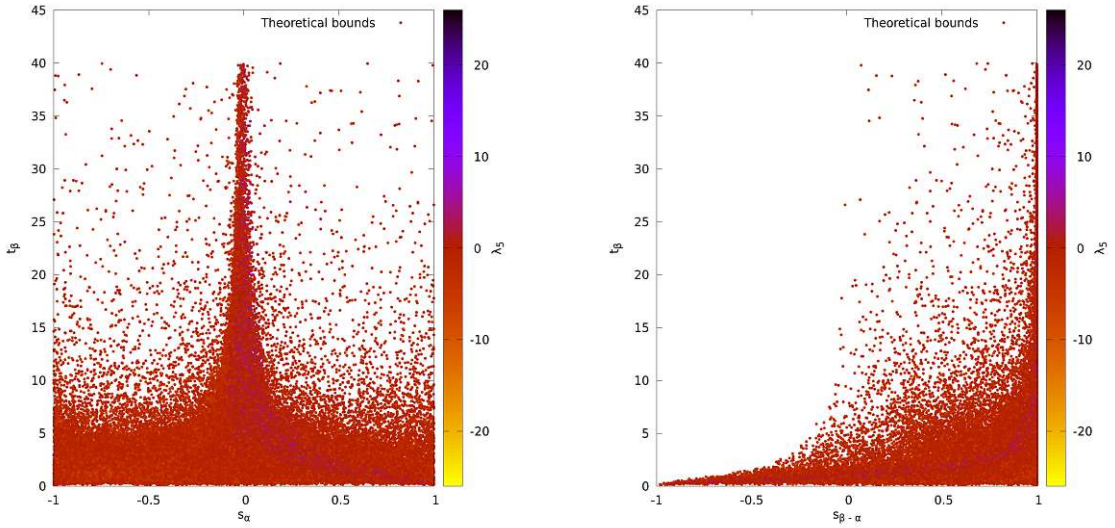


(a) (b)

Figure 3.5: Scatter plots of the parameter sets satisfying the constraints of vacuum stability, global minimum, unitarity, perturbativity, and the oblique parameters. Fig. (a) shows a scatter plot of $t_\beta$ as a function of $s_\alpha$, with $-4\pi \leq \lambda_5 \leq 4\pi$. In Fig. (b) we show a scatter plot of $t_\beta$ as a function of $s_{\beta-\alpha}$ for $-4\pi \leq \lambda_5 \leq 4\pi$.

Fig. 3.3b) and $\lambda_5$ approximately between -5 and 5. Moreover, all sets with $s_{\beta-\alpha} \lesssim 0$ have corresponding $t_\beta$ below 5. Above $s_{\beta-\alpha} \approx 0$ we observe allowed points also for greater values of $t_\beta$. However, the density of allowed points sharply decreases with growing $t_\beta$, except for $s_{\beta-\alpha} \approx 1$, where the density of allowed sets is almost uniformly distributed for $0 \lesssim t_\beta \lesssim 40$, see Fig. 3.5b.

In conclusion, we note that the obtained sets are allowed for all THDMs and that with our code we obtain an average of 1400 allowed points per 1 billion points scanned (computation time is approx. 4h depending on the specifics of the used computer), in the parameter space regions explored (it strongly depends on the specific parameter region explored). We point out that further scans in regions with $m_{H^0}$ and $m_{A^0}$ above 2 TeV might find allowed 'exotic' points. However, this numerical study clearly shows that there is a strong dependency between the masses of the Higgs bosons, the mixing angles $\alpha$ and $\beta$, and the parameter $\lambda_5$, which generate sharp bounds on the allowed parameter sets.

# Chapter 4

# Experimental bounds

In this chapter we present an overview of the current experimental bounds on the THDMs coming e.g. from the LHC at CERN and the LEP experiment. We closely follow [11], [18] and [17]. Furthermore, we present the experimental bounds that we consider throughout the study and emphasize the need for a centralized data bank that stores all experimentally excluded parameter sets. We note that all current experimental bounds can be considered with the help of the *HiggsBounds-5* package [38].

## 4.1 The 125 GeV Higgs boson

In the four types of Two Higgs Doublet Models (THDMs) explored in this work, the neutral Higgs boson Yukawa couplings to fermions (normalized to the SM) can be written as:

$$y_h^{f_i} = [\sin(\beta-\alpha) + \cos(\beta-\alpha)\kappa_f]\,, \tag{4.1}$$
$$y_H^{f_i} = [\cos(\beta-\alpha) - \sin(\beta-\alpha)\kappa_f]\,, \tag{4.2}$$
$$y_A^{f_i} = -i\kappa_f \quad \text{(for up-type quarks)}\,, \tag{4.3}$$
$$y_A^{f_i} = -i\kappa_f \quad \text{(for down-type quarks and leptons)}\,. \tag{4.4}$$

The couplings to the gauge bosons (normalized to the SM) are given by:

$$y_h^V = \sin(\beta-\alpha)\,, \tag{4.5}$$
$$y_H^V = \cos(\beta-\alpha)\,, \tag{4.6}$$

where $V = W^\pm, Z^0$. The analyses performed by the ATLAS and CMS collaborations demonstrate a notable agreement between the coupling strengths of the observed 125 GeV boson and the Higgs boson predicted by the Standard Model (SM). However, direct measurement of the coupling signs remains elusive since they cannot be measured directly. Assuming that the lightest neutral Higgs boson $h^0$ is the discovered 125 GeV Higgs boson,

its couplings have two different cases. In the first case, known as 'SM-like couplings', we have:

$$y_h^{f_i} \times y_h^V > 0\,. \tag{4.7}$$

In the second case, known as "wrong-sign Yukawa couplings," we have:

$$y_h^{f_i} \times y_h^V < 0\,. \tag{4.8}$$

In the first case, the couplings of the 125 GeV $h^0$ Higgs boson are very close to the couplings in the SM, which has an alignment limit. In the alignment limit, the scalar field responsible for electroweak symmetry breaking aligns with the discovered Higgs boson, leading to specific predictions for its properties. In this limit, the coupling strengths of the Higgs boson to fermions and gauge bosons become proportional to their corresponding Standard Model values, effectively mimicking the behavior of the SM Higgs boson. This alignment occurs when the mixing angle between the two Higgs doublets approaches a specific value known as the alignment angle. In the exact alignment [39, 40], namely when $\cos(\beta-\alpha) = 0$, we see from (4.1) and (4.5) that $h^0$ has the same couplings to fermions and gauge bosons as in the SM. The heavier and CP-even Higgs boson $H^0$ has not couplings to the gauge bosons in this limit.

The analyses of the 125 GeV $h^0$ Higgs boson data obtained at the LHC, show that the absolute values of the couplings $y_h^{f_i}$ and $y_h^V$ must be close to 1.0. As shown in [11], this implies that

$$\kappa_f \ll -1\,, \tag{4.9}$$

for $\sin(\beta-\alpha) > 0$ and $\cos(\beta-\alpha) > 0$, and

$$\kappa_f \gg 1\,, \tag{4.10}$$

for $\sin(\beta-\alpha) < 0$ and $\cos(\beta-\alpha) > 0$, with $\kappa_f$ defined in Tab. 1.2. In all four types of THDMs we investigate, the measurement of the branching ratio of the process $b \to s\gamma$ favors $\tan\beta > 1$. This in turn implies that for $\sin(\beta-\alpha) > 0$ and $\cos(\beta-\alpha) > 0$, there may exist wrong-sign Yukawa couplings for the leptons and down-type quarks in the Type-II THDM, for the leptons in the lepton-specific THDM and for the down-type quarks in the flipped THDM. This can be inferred from the definitions of the $\kappa_f$ parameters shown in Table 1.2. L. Wang et al [11] show that in the Type-II THDM the LHC signal data allows $\sin(\beta-\alpha)$ to deviate more significantly from 1 in the wrong-sign Yukawa couplings case compared to the SM-like couplings scenario. Furthermore, in the wrong-sign Yukawa couplings case, for given $\sin(\beta-\alpha)$, $\tan\beta$ has a stringent upper and lower bound.

Run I and II at the LHC have measured the 125 GeV $h^0$ Higgs bosons signal strength via different production channels. In [41] this data is combined to give a 95% confidence limit (C.L.) on the mixing angles $\alpha$ and $\beta$ in the Type-I and Type-II THDMs. In particular, they observe that the alignment limit $\beta-\alpha = \pi/2$ is favoured by the global fit. Moreover, for the Type-I THDM and $\tan\beta \gtrsim 2$, they find that $|\cos(\beta-\alpha)|$ is bounded to be less than 0.4. This limit is envisioned to be further constrained to 0.2 with the high-luminosity LHC runs [42]. In the Type-II THDM, the region around $\tan\beta = 1$ allows for the largest deviations from the alignment limit. In [41] the LHC runs-I and II are said to constrain $\cos(\beta-\alpha)$ approximately in the range $(-0.01, 0.08)$, with $\tan\beta = 1$.

## 4.2 Search for additional scalar particles

The ATLAS and CMS collaborations have conducted extensive searches for an extra scalar particle by examining its decay into various channels of the Standard Model (SM) or through its exotic decays [43–46]. Due to the potential enhancement of Yukawa couplings for down-type quarks and leptons by a factor of $\tan\beta$, the Type-II THDM can face stronger constraints compared to the other three types of models through flavor observables and the additional Higgs searches carried out at the LHC. The gluon-gluon fusion, generated by the exchange of a top quark and a b quark in the loops, is the main production mechanism for the heavy and neutral $H^0$ and $A^0$ Higgs bosons. The loop contributions of the top and bottom quarks may also destructively interfere. Various analyses have been carried out (e.g. using the 2HDMC and SusHi packages to calculate cross sections and branching ratios [47, 48]). E.g. in [49, 50] large numbers of CMS and ATLAS (LHC experiments) analyses at 8 TeV and 13 TeV, have been used to constrain the Type-II THDM. As shown in [11] the couplings $C(A^0, h^0, Z^0)$ and $C(A^0, H^0, Z^0)$ are respectively proportional to $\cos(\beta-\alpha)$ and $\sin(\beta-\alpha)$. In the SM - like coupling scenario, $|\sin(\beta-\alpha)|$ is very close to 1. This implies that the channel $A^0 \to h^0 Z^0$ does not constrain the parameter space, whereas the channel $A^0 \to H^0 Z^0$ is able to exclude a large number of points in the region with $m_{H^0} < 360$ GeV. Furthermore, the $H^0/A^0 \to \tau^+\tau^-$ channels give an upper bound on $\tan\beta$, and a range on the mass of heavy Higgs boson $m_{H^0}$ between 150 and 800 GeV for appropriate $\sin(\beta-\alpha)$ and $\tan\beta$. In the case of the wrong-sign Yukawa type couplings, the LHC data for the 125 GeV Higgs boson requires that $\tan\beta > 5$ and $\sin(\beta-\alpha) > 0.94$. This implies that the cross sections of the $H^0$ and $A^0$ gluon fusion production mechanisms are considerably suppressed. This in turn means that only the $b\bar{b} \to A^0 \to \tau^+\tau^-$ and $A^0 \to h^0 Z^0$ channels can bound the parameter space. Various ranges for the neutral $A^0$ Higgs boson are allowed for appropriate $\tan\beta$ and $\sin(\beta-\alpha)$ (see [11] for a detailed discussion).

Differently from the Type-II THDM, in the Type-I THDM all the Yukawa couplings of $H^0$, $A^0$ and $H^\pm$ can be suppressed by a large $\tan\beta$. This in turn implies that the searches for additional scalar particles at the LHC and measurements of the flavour observables are easily satisfied. Therefore, the additional Higgs bosons are allowed to have broad mass ranges.

In the Type-I THDM, the LHC searches for additional Higgs bosons have excluded the heavy Higgs boson mass ranges of 250 GeV $\lesssim m_H \lesssim$ 350 GeV. These limits are much smaller for the Type-II THDM in the theoretically allowed regions. Moreover, the branching ratio of $b \to s\gamma$ imposes a lower bound on the mass of the charged $H^\pm$ Higgs boson, $m_{H^\pm} > 570$ GeV [51, 52], for the Type-II THDM. This lower bound is relaxed for the Type-I THDM to as low as $100-200$ GeV with $\tan\beta \geqslant 2$. Additionally, a recent analysis shows that $\tan\beta > 2.5$ must be satisfied [53].

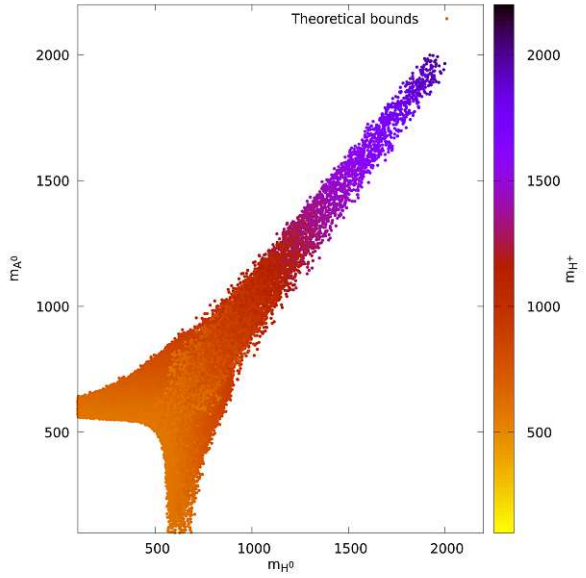


Figure 4.1: Scatter plot of the parameter sets satisfying the constraints of vacuum stability, global minimum, unitarity, perturbativity, and the oblique parameters, with the addition of the experimental bound $m_{H^\pm} \gtrsim 570$ GeV for the Type-II THDM.

## 4.3 General discussion

Due to the fact that the THDM has 7 parameters it is very difficult to have sharp experimental bounds for all parameters. Therefore, in our study we initially only consider the main experimental bounds. We do so by developing a *python* code that has as input all theoretically allowed parameter sets and as output the sets which are also allowed by the current experimental constraints that we consider. The code offers the possibility to choose the specific THDM (Type-I, Type-II, lepton-specific or flipped), since the experimental bounds are model dependent. Moreover, we aim at developing this code to include as many experimental bounds as possible. However, this currently resides outside the scope of this work.

For all THDMs the experimental bounds which we consider are

$$m_{H^\pm} > 100 \text{ GeV} \quad m_{A^0} > 100 \text{ GeV} \quad m_{H^0} > 100 \text{ GeV}\,. \tag{4.11}$$

For the Type-I THDM we also exclude the heavy Higgs region $250 \text{ GeV} \lesssim m_H \lesssim 350$ GeV. Furthermore, for the Type-II THDM we impose the lower bound $m_{H^\pm} \gtrsim 570$ GeV. In Fig. 4.1 we show the full data set of theoretically allowed parameter points which also considers this experimental bound on $m_{H^\pm}$ for the Type-II THDM, see Fig. 3.3a for comparison.

In conclusion, the large amount of experimental data and the lack of a centralized data bank that stores all experimentally excluded parameter sets, does not allow for a comprehensive implementation of all experimental bounds in this work. However, we note

that with the help of the *HiggsBounds-5* package [38], all experimental bounds can be implemented. Even though this currently resides outside the scope of this work, it is of interest for future extensions of the current study.

# Chapter 5

# Total cross sections

In this Chapter, we derive the total cross sections for the production channels $\mu^-\mu^+ \to t\bar{t}$, $\mu^-\mu^+ \to h^0h^0$, $\mu^-\mu^+ \to b\bar{b}$, and $\mu^-\mu^+ \to \tau^-\tau^+$. Furthermore, we develop a Breit-Wigner formula applicable to any scattering process of the form $\mu^-\mu^+ \to H^0/h^0 \to X$. This formula allows us to investigate the $H^0$ and $A^0$ resonant behavior and analyze the corresponding scattering processes in detail. Additionally, we introduce a forward-backward asymmetry formula, which serves as a visualization tool for studying the resonances in angle-dependent cross sections. By utilizing this asymmetry formula, we gain further insights into the characteristics and behavior of the scattering processes under investigation and it should enhance the effect of the resonances.

## 5.1 $\mu^-\mu^+ \to t\bar{t}$ - channel

### 5.1.1 Matrix element

In this Section we derive the matrix elements for the $\mu^-\mu^+ \to t\bar{t}$ scattering and derive an analytical expression for the total cross section. The Feynman graphs for this process are all s-channel scatterings of the form $\mu^-\mu^+ \to Y \to t\bar{t}$, with $Y = h^0, H^0, A^0, \gamma$ and $Z^0$.

With help of the Mandelstam variables we can describe the kinematics of the system in the center of mass frame (CMS)

$$S = (p_1 + p_2)^2 = (p_3 + p_4)^2 \,, \tag{5.1}$$

$$T = (p_1 - p_3)^2 = (p_4 - p_2)^2 \,, \tag{5.2}$$

$$U = (p_1 - p_4)^2 = (p_3 - p_2)^2 \,. \tag{5.3}$$

We evaluate the binomials and solve for the inner products of the momenta $p_i$ and $k_i$. We also have at our disposal one more equation relating the three Mandelstam variables with which we can eliminate $U$ from the computation:

$$S + T + U = 2m_t^2 \,. \tag{5.4}$$

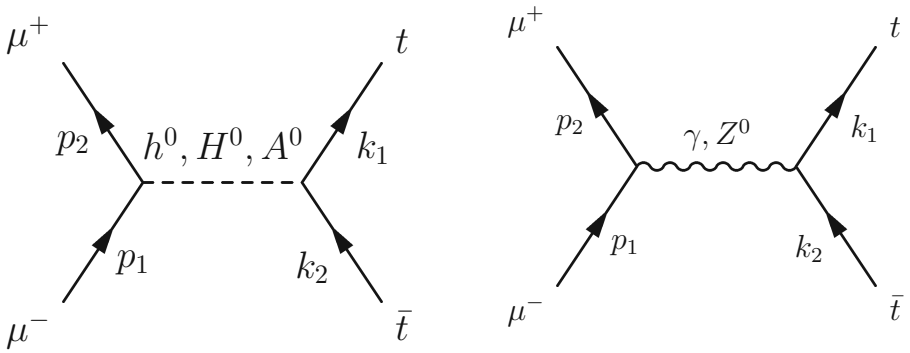


Figure 5.1: $\mu^-\mu^+ \to t\bar{t}$ Feynman diagrams in the THDM. All momenta are in time direction from left to right.

The resulting inner products as a function of the Mandelstam variables $S$ and $T$ are:

$$p_1 \cdot k_1 = p_2 \cdot k_2 = \frac{m_t^2 - T}{2}\,, \tag{5.5}$$

$$k_1 \cdot p_2 = p_1 \cdot k_2 = \frac{-m_t^2 + S + T}{2}\,. \tag{5.6}$$

Momentum conservation is given by: $p_1 + p_2 = k_1 + k_2$. By using the Feynman rules and trace technique in [8, 9, 20, 21] we compute the matrix elements squared for this scattering processes

$$M_{h^0} M_{h^0}^\dagger = -\frac{3\cos\alpha^2 e^4 m_t^2 m_\mu^2 (4m_t^2 - S) S Y_1^2}{4 m_w^4 (m_{h^0}^2 - S)^2 \sin\beta^2 \sin\theta_w{}^4}\,, \tag{5.7}$$

$$M_\gamma M_\gamma^\dagger = \frac{32 e^4 (2m_t^4 + S^2 - 4m_t^2 T + 2ST + 2T^2)}{3S^2}\,, \tag{5.8}$$

$$\begin{aligned} M_{Z^0} M_{Z^0}^\dagger = {} & \frac{1}{12\cos\theta_w{}^2 (m_Z^2 - S)^2 \sin\theta_w{}^2} e^4 [S^2 (9 - 60\sin\theta_w{}^2 \\ & + 148\sin\theta_w{}^4 - 160\sin\theta_w{}^6 + 128\sin\theta_w{}^8) \\ & + m_t^4 (9 - 60\sin\theta_w{}^2 + 200\sin\theta_w{}^4 - 320\sin\theta_w{}^6 + 256\sin\theta_w{}^8) \\ & + 2S(9 - 60\sin\theta_w{}^2 + 148\sin\theta_w{}^4 - 160\sin\theta_w{}^6 + 128\sin\theta_w{}^8) T \\ & + (9 - 60\sin\theta_w{}^2 + 200\sin\theta_w{}^4 - 320\sin\theta_w{}^6 + 256\sin\theta_w{}^8) T^2 \\ & - m_t^2 (S(27 - 180\sin\theta_w{}^2 + 496\sin\theta_w{}^4 - 640\sin\theta_w{}^6 + 512\sin\theta_w{}^8) \\ & + 2(9 - 60\sin\theta_w{}^2 + 200\sin\theta_w{}^4 - 320\sin\theta_w{}^6) + 256\sin\theta_w{}^8) T)]\,, \end{aligned} \tag{5.9}$$

$$M_{H^0} M_{H^0}^\dagger = -\frac{3 Y_2^2 e^4 m_\mu^2 m_t^2 (4m_t^2 - S) S \sin\alpha^2}{4 m_w^4 (m_{H^0}^2 - S)^2 \sin\beta^2 \sin\theta_w{}^4}\,, \tag{5.10}$$

$$M_{A^0} M_{A^0}^\dagger = -\frac{3 e^4 m_\mu^2 m_t^2 S^2 Y_3^2}{4 t_\beta^2 m_w^4 (m_{A^0}^2 - S)^2 \sin\theta_w{}^4}\,, \tag{5.11}$$

$$M_{h^0} M_{H^0}^\dagger = -\frac{3\cos\alpha e^4 m_\mu^2 m_t^2 (4m_t^2 - S) S \sin\alpha Y_1 Y_2}{4m_w^4 (S - m_{h^0}^2)(S - m_{H^0}^2) \sin\beta^2 \sin{\theta_w}^4}\,, \tag{5.12}$$

$$\begin{aligned} M_\gamma M_{Z^0}^\dagger = \frac{2e^4}{3\cos{\theta_w}^2 S(S - m_Z^2)\sin{\theta_w}^2}[S^2 \\ (3 - 10\sin{\theta_w}^2 + 16\sin{\theta_w}^4) + \\ m_t^4(3 - 20\sin{\theta_w}^2 + 32\sin{\theta_w}^4) + \\ 2S(3 - 10\sin{\theta_w}^2 + 16\sin{\theta_w}^4)T + \\ (3 - 20\sin{\theta_w}^2 + 32\sin{\theta_w}^4)T^2 - \\ m_t^2(3S + 2(3 - 20\sin{\theta_w}^2 + 32\sin{\theta_w}^4)T)]\,. \end{aligned} \tag{5.13}$$

We checked the matrix elements with the help of FA/FC [8, 9].

### 5.1.2 Total cross section

For a $2 \to 2$ scattering[1] with incoming $\mu^-\mu^+$, the differential cross section is given by [20]

$$\mathrm{d}\sigma = \frac{1}{4}\frac{1}{2S}|M_{\mathrm{tot}}|^2 \mathrm{dLips}_2(k_1, k_2)\,, \tag{5.14}$$

where

$$\begin{aligned} \mathrm{dLips}_2 &= \frac{1}{(4\pi)^2}\frac{p_{cm}}{\sqrt{S}}\,\mathrm{d}\cos\theta\,\mathrm{d}\varphi \\ &= \frac{1}{32\pi^2 S}\sqrt{\lambda(S, m_t^2, m_t^2)}\,\mathrm{d}\cos\theta\,\mathrm{d}\varphi\,, \end{aligned} \tag{5.15}$$

with the Källén function

$$\lambda(a, b, c) = (a - b - c)^2 - 4bc\,. \tag{5.16}$$

The total cross section is thus given by

$$\sigma_{\mathrm{tot}}[\mathrm{fb}] = \left(3.89 * 10^8\right)\frac{1}{128\pi S}\left(1 - \frac{4m_t^2}{S}\right)^{\frac{1}{2}}\int_{-1}^{1}\mathrm{d}\cos\theta|\overline{M_{\mathrm{tot}}}|^2\,, \tag{5.17}$$

with $3.89 * 10^8$ being the transformation factor from $\mathrm{GeV}^{-2}$ to fbarn. We obtain the total cross section $\sigma_{\mathrm{tot},t\bar{t}}$ by analytically integrating the sum of the matrix elements squared

[1] A head-to-head collision of two massless particles.

(5.7),(5.8), (5.9), (5.10), (5.11), (5.12) and (5.13),

$$\sigma_{\text{tot},t\bar{t}} = \frac{1}{S}53742.4\sqrt{1-\frac{4m_t^2}{S}}\left(\frac{768\pi^2\alpha^2m_t^4}{S^2}+\frac{768\pi^2\alpha^2m_t^2}{S}+256\pi^2\alpha^2+\right.$$
$$\frac{8\pi\alpha e^2\left(12m_t^2Ss_w^2\left(8s_w^2-5\right)+m_t^4\left(96s_w^4-60s_w^2+9\right)+S^2\left(32s_w^4-20s_w^2+3\right)\right)}{c_w^2Ss_w^2\left(S-m_Z^2\right)}+$$
$$\frac{27e^4m_\mu^2m_t^2S^2Y_{3l}^2}{m_W^4s_w^4t_\beta^2\left(\Gamma_{A^0}^2m_{A^0}^2+\left(m_{A^0}^2-S\right)^2\right)}+\frac{54c_\alpha e^4m_\mu^2m_t^2Ss_\alpha Y_{1l}Y_{2l}\left(S-m_{H^0}^2\right)\left(4m_t^2-S\right)}{m_W^4s_\beta^2s_w^4\left(S-m_{h^0}^2\right)\left(\Gamma_{H^0}^2m_{H^0}^2+\left(m_{H^0}^2-S\right)^2\right)}-$$
$$\frac{27e^4m_\mu^2m_t^2Ss_\alpha^2Y_{2l}^2\left(4m_t^2-S\right)}{m_W^4s_\beta^2s_w^4\left(\Gamma_{H^0}^2m_{H^0}^2+\left(m_{H^0}^2-S\right)^2\right)}-\frac{27c_\alpha^2e^4m_\mu^2m_t^2SY_{1l}^2\left(4m_t^2-S\right)}{m_W^4s_\beta^2s_w^4\left(m_{h^0}^2-S\right)^2}+$$
$$\frac{1}{c_w^4s_w^4\left(m_Z^2-S\right)^2}\left(e^4\left(3m_t^2S\left(256s_w^8-320s_w^6+32s_w^4+36s_w^2-9\right)+\right.\right.$$
$$\left.\left.3m_t^4\left(256s_w^8-320s_w^6+200s_w^4-60s_w^2+9\right)+S^2\left(256s_w^8-320s_w^6+200s_w^4-60s_w^2+9\right)\right)\right). \tag{5.18}$$

We verify the total cross section analytically and numerically with FA/FC [8, 9].

## 5.2 $\mu^-\mu^+ \to h^0h^0$ - channel

### 5.2.1 Matrix element

In a manner similar to the $\mu^-\mu^+ \to t\bar{t}$ channel, we proceed to derive the matrix element for the $\mu^-\mu^+ \to h^0h^0$ and obtain an analytical expression for the total cross section. In this particular process, we encounter two s-channel interactions, as well as one t-channel and one u-channel scattering processes. However, the contributions from the t- and u-channels are significantly suppressed compared to the s-channel, rendering them negligible and allowing us to disregard them in our analysis. This is because in the t- and u-channels the muon Yukawa coupling enters quadratically due to the two vertices $\mu^-\mu^+ \to h^0$. Additionally, it is important to note that the neutral $A^0$ Higgs boson does not exhibit any coupling to the SM Higgs boson $h^0$ due to its CP-odd nature. Consequently, we are left with only two permissible Feynman diagrams, namely $\mu^-\mu^+ \to X \to h^0h^0$, where $X$ can represent either $h^0$ or $H^0$.

The matrix element of this process is determined by the vertex couplings involving $\mu^-\mu^+ \to h^0/H^0$ and $h^0/H^0 \to h^0h^0$, in addition to the Higgs boson propagator. In this Chapter, we provide a comprehensive derivation of the matrix elements for the sake of instructive purposes, aiming to offer a detailed example of how to derive such matrix

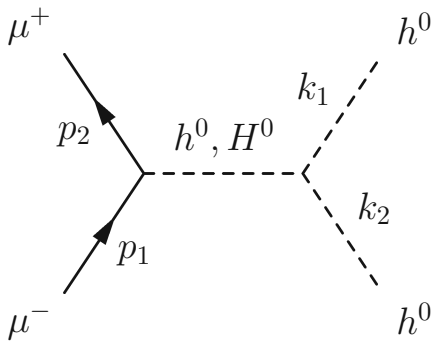


Figure 5.2: s-channel $\mu^-\mu^+ \to h^0h^0$ Feynman diagrams in the THDM. All momenta are in time direction from left to right.

elements. The same techniques apply to all other Feynman diagrams. The Feynman rules read [8, 9]

$$C(\mu^-, \mu^+, h^0) = -i\frac{em_\mu Y_1}{2m_w \sin\theta_w}\,, \tag{5.19}$$

$$C(\mu^-, \mu^+, H^0) = -i\frac{em_\mu Y_2}{2m_w \sin\theta_w}\,, \tag{5.20}$$

$$C(h^0, h^0, h^0) = -\frac{3ie}{2m_w \sin\theta_w \sin 2\beta}((2\cos\alpha + \beta + \sin 2\alpha \sin\beta - \alpha)m_{h^0}^2 - \frac{4\lambda_5 \cos\beta - \alpha^2 m_w^2 \sin\theta_w{}^2}{e^2})\,, \tag{5.21}$$

$$C(h^0, h^0, H^0) = -\frac{ie\cos\beta - \alpha}{2m_w \sin\theta_w \sin 2\beta}(\sin 2\alpha(2m_{h^0}^2 + m_{H^0}^2) - \frac{2\lambda_5(3\sin 2\alpha - \sin 2\beta)m_w^2 \sin\theta_w{}^2}{e^2})\,, \tag{5.22}$$

$$\Delta = \frac{1}{q^2 - m_{h^0/H^0}^2}\,, \tag{5.23}$$

where $\Delta$ is the Higgs boson propagator and $q^2 = (p_1+p_2)^2$, i.e. the transferred momentum. We obtain for the matrix elements

$$M_{h^0} = \bar{v}(p_2)C(\mu^-, \mu^+, h^0)u(p_1)\Delta_{m_{h^0}}C(h^0, h^0, h^0)\,, \tag{5.24}$$

and

$$M_{H^0} = \bar{v}(p_2)C(\mu^-, \mu^+, H^0)u(p_1)\Delta_{m_{H^0}}C(h^0, h^0, H^0)\,. \tag{5.25}$$

By identifying all constants with

$$c_{h^0/H^0} := C(\mu^-, \mu^+, h^0/H^0)\Delta_{m_{h^0/H^0}}C(h^0, h^0, h^0/H^0)\,, \tag{5.26}$$

we can rewrite the matrix element as

$$M_{h^0/H^0} = icT\,, \tag{5.27}$$

with $T = \bar{v}(p_2)v(p_1)$. The matrix elements squared are then given by

$$\begin{aligned}(MM^\dagger)_{h^0/H^0} &= c^2_{h^0/H^0}(\bar{v}(p_2)u(p_1))(\bar{u}(p_1)v(p_2)) \\ &= c^2_{h^0/H^0}\mathrm{Tr}(\not{p}_2\not{p}_1) \\ &= 4c^2_{h^0/H^0}(p_2 \cdot p_1) \\ &= 4c^2_{h^0/H^0}\frac{1}{2}(S - 2m^2_\mu)\,,\end{aligned} \tag{5.28}$$

where we have used the definition of the Mandelstam variables of sec.5.1.1.

### 5.2.2 Total cross section

As in Section 5.1.2 the total cross section is again given by

$$\sigma_{\mathrm{tot}}[\mathrm{fb}] = \left(3.89 * 10^8\right)\frac{1}{256\pi S}\left(1 - \frac{4m^2_{h^0}}{S}\right)^{\frac{1}{2}}\int_{-1}^{1}\mathrm{d}\cos\theta\overline{|M_{\mathrm{tot}}|}^2 \tag{5.29}$$

We note that an extra factor 1/2 is multiplied, in order to account for the fact that the outgoing particles are identical. We analytically integrate the matrix elements squared and obtain for the total cross section

$$\begin{aligned}\sigma_{\mathrm{tot},h^0h^0} = \frac{967364.0}{S}\sqrt{1 - \frac{4m^2_{h^0}}{S}} \\ \left(\frac{c^2_{\beta-\alpha}e^4m^2_\mu SY^2_{2l}\left(s_{2\alpha}\left(2m^2_{h^0} + m^2_{H^0}\right) - \frac{2\lambda_5 m^2_W s^2_w(3s_{2\alpha}-s_{2\beta})}{e^2}\right)^2}{8m^4_W s^2_{2\beta}s^4_w\left(\Gamma^2_{H^0}m^2_{H^0} + \left(S - m^2_{H^0}\right)^2\right)} + \right. \\ \left.\frac{9e^4m^2_\mu SY^2_{1l}\left(m^2_{h^0}(2c_{\beta+\alpha} + s_{2\alpha}s_{\beta-\alpha}) - \frac{4c^2_{\beta-\alpha}c_{\beta+\alpha}\lambda_5 m^2_W s^2_w}{e^2}\right)^2}{8m^4_W s^2_{2\beta}s^4_w\left(S - m^2_{h^0}\right)^2}\right).\end{aligned} \tag{5.30}$$

## 5.3 $\mu^-\mu^+ \to b\bar{b}$ - channel

### 5.3.1 Matrix element

The matrix element for the $\mu^-\mu^+ \to b\bar{b}$ channel is analogous to the $\mu^-\mu^+ \to t\bar{t}$ channel, except for the mass of the quark and the coupling constants. However, the general structure of the matrix elements remains the same. In particular, we have 6 s-channel scattering processes for the $h^0, H^0, A^0, \gamma$ and $Z^0$ bosons, two of which are the interference terms between $\gamma$ and $Z^0$, and $h^0$ and $H^0$.

As in Sec.5.1.1 we work in the center of mass system and describe the kinematics of the system with the Mandelstam variables defined in Eqs. (5.1), (5.2) and (5.3). We

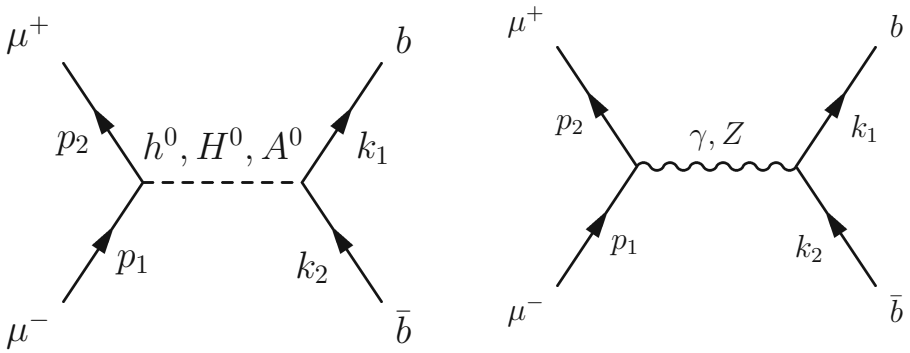


Figure 5.3: s-channel $\mu^-\mu^+ \to b\bar{b}$ Feynman diagrams in the THDM. All momenta are in time direction from left to right.

evaluate the binomials and solve for the inner products of the momenta $p_i$ and $k_i$. We also have at our disposal one more equation relating the three Mandelstam variables with which we can eliminate $U$ from the computation:

$$S + T + U = 2m_b^2 \,. \tag{5.31}$$

The resulting inner products as a function of the Mandelstam variables $S$ and $T$ are:

$$p_1 \cdot k_1 = p_2 \cdot k_2 = \frac{m_b^2 - T}{2} \,, \tag{5.32}$$

$$k_1 \cdot p_2 = p_1 \cdot k_2 = \frac{-m_b^2 + S + T}{2} \,. \tag{5.33}$$

Momentum conservation is again given by: $p_1 + p_2 = k_1 + k_2$. The matrix elements squared for this scattering process are

$$M_{h^0} M_{h^0}^\dagger = -\frac{3e^4 m_b^2 m_\mu^2 (4m_b^2 - S) S Y_1^4}{4m_w^4 (m_{h^0}^2 - S)^2 \sin\beta^2 \sin\theta_w{}^4} \,, \tag{5.34}$$

$$M_\gamma M_\gamma^\dagger = \frac{8\alpha^2\pi^2(2m_b^4 + S^2 - 4m_b^2 T + 2ST + 2T^2)}{3S^2} \,, \tag{5.35}$$

$$\begin{aligned} M_{Z^0} M_{Z^0}^\dagger = \frac{1}{192 \sin\theta_w{}^4 \sin\theta_w{}^4 (m_Z^2 - S)^2} \big(e^4 \big(-2m_b^2 \big(S \left(60 \sin\theta_w{}^4 - 42 \sin\theta_w{}^2 + 9\right) \\ + \left(64 \sin\theta_w{}^8 - 128 \sin\theta_w{}^6 + 128 \sin\theta_w{}^4 - 48 \sin\theta_w{}^2 + 9\right) T\big) + \\ m_b^4 \left(64 \sin\theta_w{}^8 - 128 \sin\theta_w{}^6 + 128 \sin\theta_w{}^4 - 48 \sin\theta_w{}^2 + 9\right) + \\ S^2 \left(32 \sin\theta_w{}^8 - 64 \sin\theta_w{}^6 + 88 \sin\theta_w{}^4 - 48 \sin\theta_w{}^2 + 9\right) + \\ 2S \left(32 \sin\theta_w{}^8 - 64 \sin\theta_w{}^6 + 88 \sin\theta_w{}^4 - 48 \sin\theta_w{}^2 + 9\right) T + \\ \left(64 \sin\theta_w{}^8 - 128 \sin\theta_w{}^6 + 128 \sin\theta_w{}^4 - 48 \sin\theta_w{}^2 + 9\right) T^2\big)\big) \,, \end{aligned} \tag{5.36}$$

$$M_{H^0} M_{H^0}^{\dagger} = -\frac{3Y_2^2 e^4 m_\mu^2 m_b^2 (4m_b^2 - S) S Y_2^2}{4m_w^4 (m_{H^0}^2 - S)^2 \sin\theta_w{}^4}\,, \tag{5.37}$$

$$M_{A^0} M_{A^0}^{\dagger} = \frac{3e^4 m_\mu^2 m_b^2 S^2 Y_3^4}{4m_w^4 (m_{A^0}^2 - S)^2 \sin\theta_w{}^4}\,, \tag{5.38}$$

$$M_{h^0} M_{H^0}^{\dagger} = -\frac{3e^4 m_\mu^2 m_b^2 (4m_b^2 - S) S Y_1^2 Y_2^2}{4m_w^4 (S - m_{h^0}^2)(S - m_{H^0}^2) \sin\theta_w{}^4}\,, \tag{5.39}$$

$$M_\gamma M_{Z^0}^{\dagger} = \frac{1}{6\cos\theta_w{}^2 S \sin\theta_w{}^2 (S - m_Z^2)} \left(\pi\alpha e^2 \left(-m_b^2 \left(3S + 2\left(16\sin\theta_w{}^4 - 16\sin\theta_w{}^2 + 3\right) T\right)\right.\right. \tag{5.40}$$

$$+ m_b^4 \left(16\sin\theta_w{}^4 - 16\sin\theta_w{}^2 + 3\right) + S^2 \left(8\sin\theta_w{}^4 - 8\sin\theta_w{}^2 + 3\right) +$$
$$\left.\left. 2S\left(8\sin\theta_w{}^4 - 8\sin\theta_w{}^2 + 3\right) T + \left(16\sin\theta_w{}^4 - 16\sin\theta_w{}^2 + 3\right) T^2\right)\right)\,,$$

where we use the Feynman rules defined in [8, 9] and the trace technique presented in [20, 21].

### 5.3.2 Total cross section

The total cross section is again given by (as in 5.1.2)

$$\sigma_{\text{tot}}[\text{fb}] = \left(3.89 * 10^8\right) \frac{1}{128\pi S} \left(1 - \frac{4m_b^2}{S}\right)^{\frac{1}{2}} \int_{-1}^{1} \text{dcos}\,\theta |\overline{M_{\text{tot}}}|^2\,. \tag{5.41}$$

We analytically integrate the matrix elements squared and obtain for the total cross section

$$\sigma_{\text{tot},b\bar{b}} = \frac{53742.4}{S}\sqrt{1 - \frac{4m_b^2}{S}} \left(\frac{192\pi^2\alpha^2 m_b^4}{S^2} + \frac{192\pi^2\alpha^2 m_b^2}{S} + 64\pi^2\alpha^2 + \right. \tag{5.42}$$

$$\frac{64\pi\alpha e^2 \left(48 m_b^2 S s_w^2 \left(s_w^2 - 1\right) + m_b^4 \left(48 s_w^4 - 48 s_w^2 + 9\right) + S^2 \left(16 s_w^4 - 16 s_w^2 + 3\right)\right)}{c_w^2 S s_w^2 \left(S - m_Z^2\right)} +$$

$$\frac{27 e^4 m_b^2 m_\mu^2 S^2 Y_{3d}^2 Y_{3l}^2}{m_W^4 s_w^4 \left(\Gamma_{A^0}^2 m_{A^0}^2 + \left(m_{A^0}^2 - S\right)^2\right)} + \frac{54 e^4 m_b^2 m_\mu^2 S Y_{1d} Y_{1l} Y_{2d} Y_{2l} \left(4m_b^2 - S\right)\left(S - m_{H^0}^2\right)}{m_W^4 s_w^4 \left(S - m_{h^0}^2\right)\left(\Gamma_{H^0}^2 m_{H^0}^2 + \left(m_{H^0}^2 - S\right)^2\right)} -$$

$$\frac{27 e^4 m_b^2 m_\mu^2 S Y_{2d}^2 Y_{2l}^2 \left(4m_b^2 - S\right)}{m_W^4 s_w^4 \left(\Gamma_{H^0}^2 m_{H^0}^2 + \left(m_{H^0}^2 - S\right)^2\right)} - \frac{27 e^4 m_b^2 m_\mu^2 S Y_{1d}^2 Y_{1l}^2 \left(4m_b^2 - S\right)}{m_W^4 s_W^4 \left(m_{h^0}^2 - S\right)^2} +$$

$$e^4 \frac{3m_b^2 S \left(64 s_w^8 - 128 s_w^6 + 8 s_w^4 + 36 s_w^2 - 9\right) + 3m_b^4 \left(64 s_w^8 - 128 s_w^6 + 128 s_w^4 - 48 s_w^2 + 9\right)}{c_w^4 s_w^4 \left(m_Z^2 - S\right)^2} +$$

$$\left. e^4 \frac{S^2 \left(64 s_w^8 - 128 s_w^6 + 128 s_w^4 - 48 s_w^2 + 9\right)}{c_w^4 s_w^4 \left(m_Z^2 - S\right)^2}\right)\,.$$

## 5.4 $\mu^-\mu^+ \to \tau^+\tau^-$ - channel

### 5.4.1 Matrix element

Similarly to the top and bottom quark channels, for the $\mu^-\mu^+ \to \tau^+\tau^-$ channel, we have 6 s-channel scattering processes for the $h^0, H^0, A^0, \gamma$ and $Z^0$ bosons, two of which are the interference terms between $\gamma$ and $Z^0$, and $h^0$ and $H^0$.

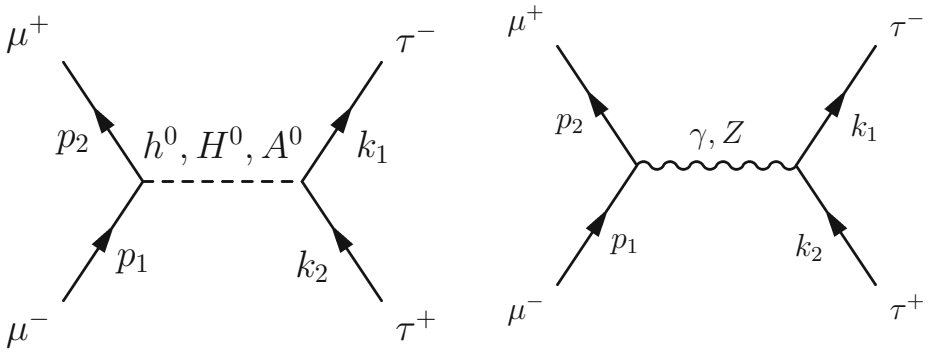


Figure 5.4: s-channel $\mu^-\mu^+ \to \tau^-\tau^+$ Feynman diagrams in the THDM. All momenta are in time direction from left to right.

As in Sec. 5.1.1 we work in the center of mass system and describe the kinematics of the system with the Mandelstam variables defined in Eqs. (5.1), (5.2) and (5.3). We evaluate the binomials and solve for the inner products of the momenta $p_i$ and $k_i$. We also have at our disposal one more equation relating the three Mandelstam variables with which we can eliminate $U$ from the computation:

$$S + T + U = 2m_\tau^2 \,. \tag{5.43}$$

The resulting inner products as a function of the Mandelstam variables $S$ and $T$ are:

$$p_1 \cdot k_1 = p_2 \cdot k_2 = \frac{m_\tau^2 - T}{2} \,, \tag{5.44}$$

$$k_1 \cdot p_2 = p_1 \cdot k_2 = \frac{-m_\tau^2 + S + T}{2} \,. \tag{5.45}$$

Momentum conservation is again given by: $p_1 + p_2 = k_1 + k_2$. The matrix elements squared for this scattering process are

$$MM_\gamma^\dagger = \frac{8\pi^2\alpha^2\left(-4m_\tau^2(S+T) - 4m_\tau^2\left(m_\tau^2 - S\right) + 4m_\tau^4 + 2m_\tau^4 + S^2 + 2ST + 2T^2\right)}{16S^2} \,, \tag{5.46}$$

$$M_{h^0}M_{h^0}^\dagger = \frac{\pi^2\alpha^2 m_\tau^2 m_\mu^2 S Y_{1l}^2 Y_{1l}^2 \left(S - 4m_\tau^2\right)}{4m_W^4 s_w^4 \left(m_{h^0}^2 - S\right)^2} \,, \tag{5.47}$$

$$M_{Z^0}M_{Z^0}^\dagger = \frac{\pi^2\alpha^2}{4c_w^4 s_w^4 \left(m_Z^2 - S\right)^2}\Bigg( -4m_\tau^2\left(32s_w^8 - 32s_w^6 + 24s_w^4 - 8s_w^2 + 1\right)(S+T) + \tag{5.48}$$
$$2m_\tau^2\left(1-4m_\tau^2\right)^2\left(4Ss_w^4 - 2Ss_w^2 + S + T\right) + m_\tau^4\left(8s_w^4 - 4s_w^2 + 1\right)^2 +$$
$$4m_\tau^4\left(32s_w^8 - 32s_w^6 + 24s_w^4 - 8s_w^2 + 1\right) - 4m_\tau^2 m_\tau^2\left(32s_w^8 - 32s_w^6 + 24s_w^4 - 8s_w^2 + 1\right) +$$
$$32S^2s_w^8 - 32S^2s_w^6 + 24S^2s_w^4 - 8S^2s_w^2 + S^2 + 64Ss_w^8T - 64Ss_w^6T + 48Ss_w^4T -$$
$$16Ss_w^2T + 2ST + 64s_w^8T^2 - 64s_w^6T^2 + 32s_w^4T^2 - 8s_w^2T^2 + T^2\Bigg),$$

$$M_{H^0}M_{H^0}^\dagger = \frac{\pi^2\alpha^2 m_\tau^2 m_\mu^2 S Y_{2l}^2 Y_{2l}^2 \left(S - 4m_\tau^2\right)}{4m_W^4\left(s_w^4\left(\Gamma_{H^0}^2 m_{H^0}^2 + \left(m_{H^0}^2 - S\right)^2\right)\right)}, \tag{5.49}$$

$$M_{A^0}M_{A^0}^\dagger = \frac{\pi^2\alpha^2 m_\tau^2 m_\mu^2 S^2 Y_{3l}^2 Y_{3l}^2}{4m_W^4 s_w^4\left(\Gamma_{A^0}^2 m_{A^0}^2 + \left(m_{A^0}^2 - S\right)^2\right)}, \tag{5.50}$$

$$M_{h^0}M_{H^0}^\dagger = -\frac{\left(S - m_{H^0}^2\right)\left(\pi^2\alpha^2 m_\tau^2 m_\mu^2 S\left(4m_\tau^2 - S\right)\left(Y_{1l}^2 Y_{2l}^2 + Y_{1l}^2 Y_{2l}^2\right)\right)}{4m_W^4 s_w^4\left(S - m_{h^0}^2\right)\left(\Gamma_{H^0}^2 m_{H^0}^2 + \left(S - m_{H^0}^2\right)^2\right)}, \tag{5.51}$$

$$M_\gamma M_{Z^0} = \frac{\pi^2\alpha^2}{c_w^2 S s_w^2\left(S - m_Z^2\right)}\Bigg( -4m_\tau^2\left(8s_w^4 - 4s_w^2 + 1\right)(S+T) + \tag{5.52}$$
$$m_\tau^2\left(-4m_\tau^2\left(8s_w^4 - 4s_w^2 + 1\right) + S\left(32s_w^4 - 16s_w^2 + 3\right) + 2T\right) + m_\tau^4\left(1 - 4s_w^2\right)^2 +$$
$$4m_\tau^4\left(8s_w^4 - 4s_w^2 + 1\right) + 8S^2s_w^4 - 4S^2s_w^2 + S^2 + 16Ss_w^4T - 8Ss_w^2T + 2ST +$$
$$16s_w^4T^2 - 8s_w^2T^2 + T^2\Bigg),$$

where we use the Feynman rules defined in [8, 9] and the trace technique presented in [20, 21].

### 5.4.2 Total cross section

The total cross section is again given by (as in 5.1.2)

$$\sigma_{\text{tot}}[\text{fb}] = \left(3.89 * 10^8\right)\frac{1}{128\pi S}\left(1 - \frac{4m_\tau^2}{S}\right)^{\frac{1}{2}}\int_{-1}^{1} \text{dcos}\,\theta|\overline{M_{\text{tot}}}|^2. \tag{5.53}$$

With the help of *Mathematica* we analytically integrate the matrix elements squared and obtain for the total cross section

$$\sigma_{\text{tot},\tau^+\tau^-} = \frac{1.59125 \times 10^6 \alpha^2 \sqrt{1-\frac{4m_\tau^2}{S}}}{S}\left(\frac{3m_\tau^2 m_\mu^2 S^2 Y_{3l}^4}{m_W^4 s_w^4\left(\Gamma_{A^0}^2 m_{A^0}^2+\left(m_{A^0}^2-S\right)^2\right)}+\right. \tag{5.54}$$

$$\frac{12m_\tau^2 m_\mu^2 S Y_{1l}^2 Y_{2l}^2\left(S-m_{H^0}^2\right)\left(4m_\tau^2-S\right)}{m_W^4 s_w^4\left(m_{h^0}^2-S\right)\left(\Gamma_{H^0}^2 m_{H^0}^2+\left(m_{H^0}^2-S\right)^2\right)}+\frac{3m_\tau^2 m_\mu^2 S Y_{1l}^4\left(S-4m_\tau^2\right)}{m_W^4 s_w^4\left(m_{h^0}^2-S\right)^2}+$$

$$\frac{3m_\tau^2 S\left(64s_w^8-64s_w^6+8s_w^4+4s_w^2-1\right)+3m_\tau^4\left(8s_w^4-4s_w^2+1\right)^2+S^2\left(8s_w^4-4s_w^2+1\right)^2}{c_w^4 s_w^4\left(m_Z^2-S\right)^2}+$$

$$\frac{8\left(24m_\tau^2 S s_w^2\left(2s_w^2-1\right)+3m_\tau^4\left(1-4s_w^2\right)^2+S^2\left(1-4s_w^2\right)^2\right)}{c_w^2 S s_w^2\left(S-m_Z^2\right)}+$$

$$\left.\frac{12m_\tau^4}{S^2}+\frac{12m_\tau^2}{S}+4\right).$$

## 5.5 Breit - Wigner formula

In all of the studied scattering processes we have the general structure $A+B \to I \to C+D$. The incoming particles $A + B$ collide to create an unstable intermediate state $I$, which subsequently decays into the final states $C+D$. In the case that the process $A+B \to C+D$ can only occur via the intermediate state $I$, and that the width of the intermediate state is sufficiently small ($\Gamma << E_0$), the total cross section for the scattering process is given by the Breit-Wigner formula in the narrow-width approximation $\Gamma/m \to 0$

$$\sigma_{A+B\to I\to C+D} = \frac{\pi^2}{k^2} \frac{\Gamma_{A+B}\Gamma_{C+D}}{(E-E_0)^2 + \Gamma^2/4}\,, \tag{5.55}$$

where $\Gamma_{A+B}$ and $\Gamma_{C+D}$ are the partial widths, $\Gamma$ is the full width of the resonance, $E_0$ is the rest mass energy of the resonant state, $E$ the center of mass energy of the system and $k = |\vec{k}|$ is the momentum of the incoming particles in the center of mass system. The resulting cross section has a sharp peak for energies $E$ close to the rest mass energy $E_0$ of the intermediate particle. The sharpness of the peak directly depends on the width $\Gamma$.

We emphasize that this formula is only valid for one channel and does not allow for interference terms in the matrix elements. This in turn means that we cannot use this formula to derive the total cross section of the scattering processes we are studying, but we can use it to verify the single scattering channels. The Breit-Wigner formula for the processes we investigate reads

$$\sigma(\mu\bar{\mu} \to Y \to X) = \frac{4\pi\Gamma_Y^2 Br^*(Y \to \mu\bar{\mu}) Br^*(Y \to X)}{(S - m_Y^2)^2 + m_Y^2\Gamma_Y^2} \tag{5.56}$$

where $Y = \{h^0, H^0, A^0\}$ and $Br^*$ are the corresponding branching ratios, with $(*)$ meaning that the decay widths must be computed with the intermediate particle $Y$ off-shell (i.e. with $m_Y^2 \to S$).

### 5.5.1 Derivation of the narrow-widths approximation

The narrow-widths approximation (NWA) is a method used to simplify the calculation of complicated cross sections with unstable particles. The general idea is to treat the unstable particle as a stable one with an infinitely sharp resonance. In this Section we aim to provide a comprehensive derivation of this formula and more broadly of the total cross section in the narrow-widths approximation (we closely follow [54]). The NWA is valid only if the following conditions are satisfied:

- In order for off-shell effects to be negligible, the unstable particle must have a narrow mass peak.
- The propagator must be separable from the matrix element.
- All sub-processes must be kinematically allowed.

- The decay channel must be kinematically allowed and sufficiently large.

To note is that also this approximation does not allow for interference terms. Thus, we have to consider them separately. However, an extension to include interference terms is shown in [54].

## Phase space and matrix element

We can write the general Lorentz-invariant phase space ( $\mathrm{d}\Phi_n \equiv \mathrm{dLips}_n$), characterised by the number $n$ of particles in the final state as

$$\mathrm{d}\Phi_n = (2\pi)^4 \delta^{(4)} \left( P - \sum_{f=1}^{n} p_f \right) \Pi_{f=1}^{n} \frac{\mathrm{d}^3 p_f}{(2\pi)^3 2E_f} \,. \tag{5.57}$$

The NWA only works if the phase space and the matrix element are factorisable into separate sub-processes. By using this, we can rewrite the phase space element $\Phi_n$ as a product of the phase space $\Phi_k$ $(k < n)$ and $\Phi_{n-k+1}$ ,

$$\mathrm{d}\Phi_n = \mathrm{d}\Phi_k \frac{\mathrm{d}q^2}{2\pi} \mathrm{d}\Phi_{n-k+1} \,, \tag{5.58}$$

where $q$ is the momentum of the resonant particle. In our specific case of the Higgs Strahlung, $q$ is the momentum of the $Z^0$ boson that decays into the muon-neutrino pair $\nu_\mu \bar{\nu_\mu}$. In (5.58) we can interpret $\mathrm{d}\Phi_k$ as the production phase space and $\mathrm{d}\Phi_{n-k+1}$ as the phase space of the decay.

Similarly, we can write the matrix element for this process as a product of the production (P) and decay (D) part of the process. We obtain

$$M = M_P \frac{1}{q^2 - m^2 + im\Gamma} M_D \,. \tag{5.59}$$

The amplitude squared is then

$$|M|^2 = |M_P|^2 \frac{1}{(q^2 - m^2)^2 + m^2\Gamma^2} |M_D|^2 \,. \tag{5.60}$$

## Cross section

To calculate the cross section in the NWA, we note that different flux factors must be considered for the production and decay processes. In particular for the production process of the form $1 + 2 \to X$ we use $F = 2\lambda^{1/2}(s, m_1^2, m_2^2)$, where $\lambda$ is the Källén function (5.16), and $F = 2m_1$ for the decay process of the form $1 \to 2 + 3 + ....$ The total cross section is then given by

$$\sigma = \frac{1}{F} \int \mathrm{d}\Phi |M|^2 \,. \tag{5.61}$$

By inserting (5.58) and (5.60) in (5.61), we obtain for the total cross section

$$\sigma = \frac{1}{F}\int \frac{\mathrm{d}q^2}{2\pi}\left(\int \mathrm{d}\Phi_P |M_P|^2\right)\frac{1}{(q^2-m^2)^2+m^2\Gamma^2}\left(\int \mathrm{d}\Phi_D |M_D|^2\right). \tag{5.62}$$

We can now substitute in this equation the off-shell production cross section

$$\sigma_P(q^2) = \frac{1}{F}\int \mathrm{d}\Phi_P |M_P(q^2)|^2\,, \tag{5.63}$$

and the decay width

$$\Gamma_D(q^2) = \frac{1}{F_D}\int \mathrm{d}\Phi_D |M_D(q^2)|^2\,, \tag{5.64}$$

with $F_D = 2\sqrt{q^2}$, and obtain

$$\sigma = \int \frac{\mathrm{d}q^2}{2\pi}\sigma_P(q^2)\frac{2\sqrt{q^2}}{(q^2-m^2)^2+m^2\Gamma^2}\Gamma_D(q^2)\,. \tag{5.65}$$

By using the identity

$$\frac{1}{\pi}\lim_{\epsilon\to 0}\frac{\epsilon}{\eta^2+\epsilon^2} = \delta(\eta)\,, \tag{5.66}$$

and identifying $\epsilon = m\Gamma$, we can simplify the total cross section in the NWA, i.e. for $m\Gamma \to 0$

$$\sigma = \int_{-\infty}^{\infty}\frac{\mathrm{d}q^2}{2\pi}\sigma_P(q^2)2\sqrt{q^2}\delta(q^2-m^2)\frac{\pi}{m\Gamma}\Gamma_D(q^2)\,. \tag{5.67}$$

We have shifted the bounds of integration to $\pm\infty$ in order to integrate over the $\delta$-function. This is allowed because we expect the contributions from outside the narrow resonance region to be small. After integrating (5.67) we obtain the final expression

$$\sigma = \sigma_P(m^2)\frac{\Gamma_D(m^2)}{\Gamma} = \sigma_P \cdot BR\,. \tag{5.68}$$

## 5.6 Forward-Backward asymmetry

The forward-backward asymmetry (FBA) in particle physics is a powerful tool to study resonances in cross sections. It reveals how particles preferentially emit in the forward or backward directions during high-energy collisions, providing valuable insights into resonance properties and underlying physics processes. Its study helps identify and understand complex interactions, offering a gateway to explore fundamental forces and particles at the subatomic level. In our particular case, the FBA might enhance the effect of a resonance for a specific set of model parameters. This in turn means that through the FBA we might be able to observe resonances which might not be otherwise accessible.

Here we give a general formula for the FBA which we use for the cross sections of all allowed parameter sets

$$A_{\mathrm{FB}} = \frac{\sigma_f - \sigma_b}{\sigma_f + \sigma_b}\,, \tag{5.69}$$

where $\sigma_f$ is the total cross section integrated for $\cos(\theta) \in [0, 1]$, i.e. the forward hemisphere, and $\sigma_b$ is the total cross section integrated for $\cos(\theta) \in [-1, 0]$, i.e. the backward hemisphere.

# Chapter 6

# $H^0$ and $A^0$ resonances

In this chapter, we delve into a comprehensive analysis of the resonant behavior exhibited by the two neutral Higgs bosons, $H^0$ and $A^0$, within the context of the THDM. In particular we investigate the Type-I, Type-II, lepton-specific and flipped THDMs. We thoroughly investigate the scattering channels presented in Chapter 5 for each of the four investigated THDMs, recognizing that not all of them may yield observable resonances in a future Muon Collider for a particular model.

Despite this, we emphasize that exploring non-resonant channels still provides valuable insights into the nature of the particle causing the resonance. For instance, if a resonant peak is observed in the experiment for both $H^0$ and $A^0$ Higgs bosons, but it is supposed to be visible only in a specific THDM, for that specific set of parameters, it could indicate the potential validity of that model. In contrast, if the resonance appears across multiple models, it would suggest that further investigation is required to determine which specific model best aligns with nature's reality. Moreover, we make use of the forward-backward asymmetry $A_{FB}$ to enhance the resonance peak in the case of a preferred scattering direction.

In order to numerically investigate the resonances, we make use of the branching ratios ($BR$) and the ratio of mass of the Higgs boson to its total width ($MR$)

$$BR = \frac{\Gamma_{H^0/A^0 \to XY}}{\Gamma_{\text{tot}}}, \quad MR = \frac{m_{H^0/A^0}}{\Gamma_{\text{tot}}}. \tag{6.1}$$

This is in order to discern which parameter sets may yield an observable resonance in the experiment. Furthermore, we observe that the $BRs$ and $MRs$ needed in order to observe a resonant peak, strongly depend on the specific THDM and scattering channel. This directly depends on the Yukawa couplings, see (1.48), of each specific THDM and the masses of the Higgs bosons for the investigated parameter set.

For readability, throughout the chapter we write the parameter sets in the following order $\{s_\alpha, t_\beta, m_{h^0}, m_{H^0}, m_{A^0}, m_{H^\pm}, \lambda_5\}$. Furthermore, we define as 'single' cross section, the cross section that stems from the contribution of only one specific Feynman diagram of the process.

In this analysis we have taken: $m_e = 5.10998928 \times 10^-4$ GeV, $m_\mu = 0.1057$ GeV, $m_\tau = 1.7768$ GeV, $m_t = 173.21$ GeV, $m_b = 4.66$ GeV, $m_s = 9.5 \times 10^{-2}$ GeV, $m_c = 1.275$ GeV,

$m_u = 7.3559 \times 10^{-2}$ GeV, $m_d = 7.3559 \times 10^{-2}$ GeV, $m_W = 80.3850$ GeV, $m_Z = 91.1876$ GeV, $m_{h^0} = 125.0$ GeV, $s_w^2 = 0.2229$ and $\alpha = 1/137.036$.

## 6.1 Type-I THDM

In this Section, we present the numerical results for the $H^0$ and $A^0$ Higgs boson resonant production, within the Type-I THDM and the four channels we investigate ($\mu^-\mu^+ \to t\bar{t}$, $\mu^-\mu^+ \to b\bar{b}$, $\mu^-\mu^+ \to h^0h^0$, $\mu^-\mu^+ \to \tau^-\tau^+$).

To illustrate the overall resonance picture in the Type-I THDM, we compare specific benchmark scenarios. Figs. 6.1a, 6.1b, 6.2a and 6.2b show a comparison of the cross sections for resonant $H^0$ and $A^0$ Higgs bosons in the $\mu^-\mu^+ \to t\bar{t}$ channel. Notably, all four parameter sets (see captions for the exact parameter sets) do not exhibit any resonance at the respective $H^0$ and $A^0$ Higgs boson masses. This is due to the significantly larger cross sections of the $\mu^-\mu^+ \to Z^0/\gamma \to t\bar{t}$ process compared to the $H^0$ and $A^0$ mediated channels (see Fig. 6.5 and Chapter 5).

However, when studying the forward-backward asymmetry for the parameter set in Fig. 6.2a, we observe a tiny peak caused by the resonant $A^0$ Higgs boson, while the second peak caused by the $H^0$ Higgs boson remains invisible. Despite the observability of the $A^0$ resonance peak, the difference in $A_{FB}$ on and off the resonance is only a few percent, making the resonance effectively indiscernible in the experiment. This pattern holds for all other points, indicating that no resonance is visible for the other parameter sets as well. Moreover, this qualitative pattern is sustained by the fact that these benchmark examples all have high $BRs$ and $MRs$ compared to all other allowed parameter sets.

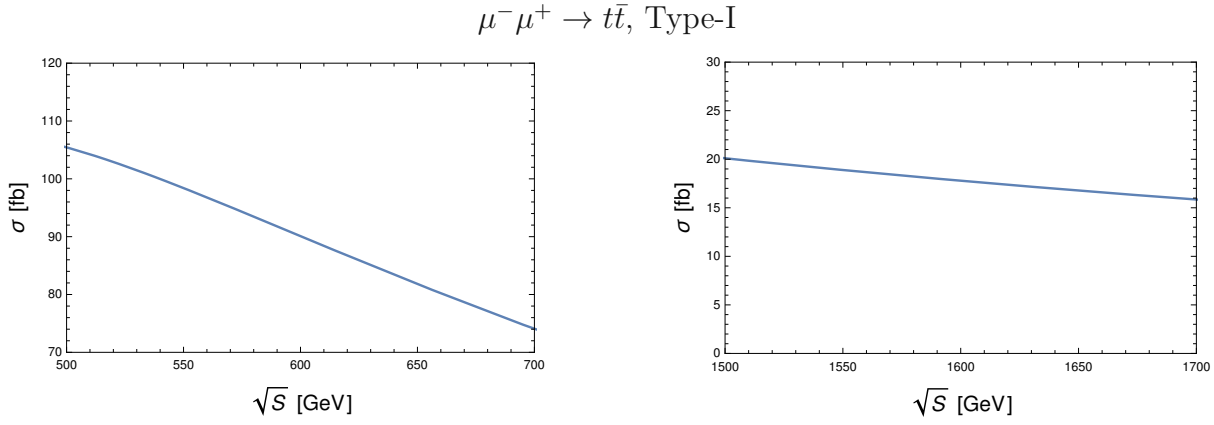


(a) (b)

Figure 6.1:
Cross section $\sigma_{\text{tot},t\bar{t}}$ as a function of $\sqrt{S}$ in the Type-I THDM. The parameters in Fig. (a) are $\{-0.152, 5.631, 125., 609.155, 639.426, 620.667, -0.766\}$ with $\lambda_{1,2,3,4} = \{6.84387, 0.210296, 1.58432, -0.0135054\}$, whereas in Fig. (b) they are $\{-0.065, 15.112, 125., 1639.33, 1643.11, 1684.58, -0.202\}$ with $\lambda_{1,2,3,4} = \{2.5923, 0.242968, 5.70064, -4.59506\}$. The $BRs$ are respectively 0.862 and 0.992, and the $MRs$ are 1134.31 and 4386.82 respectively. Here the $BR$ and $MR$ have been calculated for $m_{H^0}$, i.e. we have looked for a point which maximizes the $H^0$ resonance.

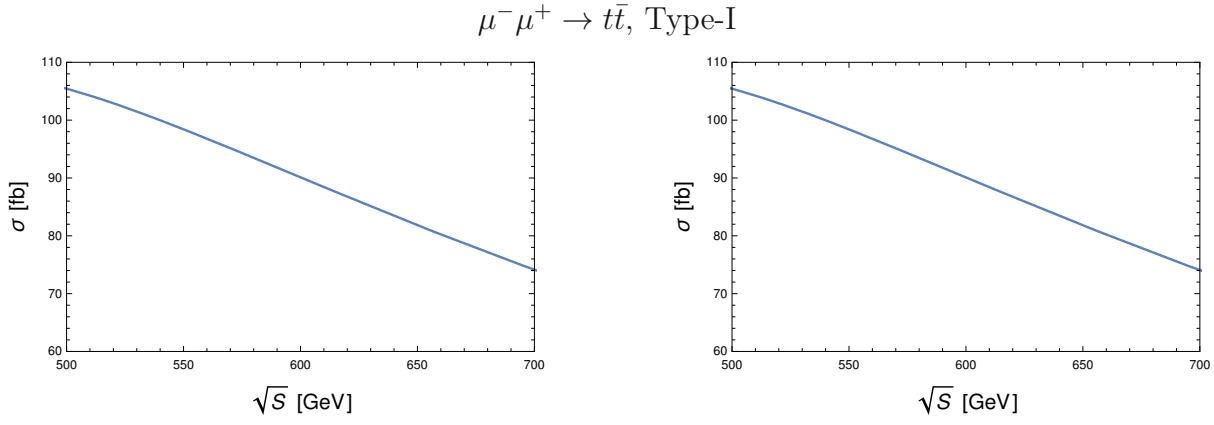


(a) (b)

Figure 6.2:
Cross section $\sigma_{\text{tot},t\bar{t}}$ as a function of $\sqrt{S}$ in the Type-I THDM. The parameters in Fig. (a) are $\{-0.367, 2.268, 125., 601.355, 680.113, 712.633, -1.938\}$ with $\lambda_{1,2,3,4} = \{2.90419, 0.128477, 5.64911, -3.37982\}$, whereas in Fig. (b) they are $\{-0.07, 14.537, 125., 581.538, 659.398, 662.054, -1.547\}$ with $\lambda_{1,2,3,4} = \{1.96678, 0.249727, 3.34316, -1.65873\}$. The $BRs$ are respectively 0.979 and 0.998, and the $MRs$ are 90.854 and 3835.62 respectively. Here the $BR$ and $MR$ have been calculated for $m_{H^0}$, i.e. we have looked for a point which maximizes the $A^0$ resonance.

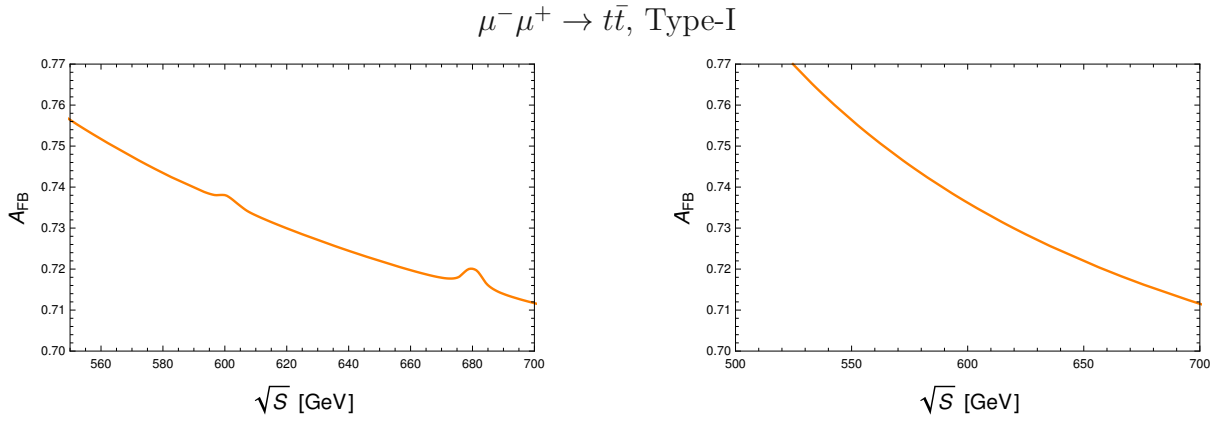


(a) (b)

Figure 6.3:
Forward-backward asymmetry $A_{FB}$ as a function of $\sqrt{S}$ in the Type-I THDM. The parameters in Fig. (a) are $\{-0.367, 2.268, 125., 601.355, 680.113, 712.633, -1.938\}$ whereas in Fig. (b) they are $\{-0.07, 14.537, 125., 581.538, 659.398, 662.054, -1.547\}$. The $BRs$ are respectively 0.979 and 0.998, and the $MRs$ are 90.854 and 3835.62 respectively.

Similarly, in the $\mu^-\mu^+ \to b\bar{b}$ channel, the resonant peaks are not visible, as shown in Fig. 6.4a. Even in the forward-backward asymmetry, no peak is observable. By studying the cross sections of the single Feynman diagrams contributing to this process, we observe that the resonant peaks are not visible due to the much larger cross sections of the $\gamma$ and $Z^0$ channels (see Fig. 6.5 and Chapter 5 for the corresponding Feynman diagrams).

Given these findings, we explore the $\mu^-\mu^+ \to h^0h^0$ channel, featuring only two Feynman diagrams (see Chapter 5): one mediated by the discovered $h^0$ Higgs boson and another by the sought-after $H^0$ Higgs boson. In this case, the $A^0$ Higgs boson and the gauge bosons do not couple to $h^0$, leading to significantly larger resonance peaks for $H^0$. However, this implies that we cannot observe the $A^0$ Higgs boson in this channel for any of the four THDMs. Moreover, due to all particles involved being scalar, there is no preferred scattering direction. Therefore, $A_{FB} = 0$ for all parameter sets. Indeed, as expected, the resonances in the $\mu^-\mu^+ \to h^0h^0$ channel are much larger (see Fig. 6.6a and 6.6b). Various parameter sets exhibit different resonance widths and total cross section magnitudes. However, we observe resonant peaks for a large number of parameter sets, with large enough $BR$ and $MR$. Furthermore, this channel enables the unequivocal identification of the $H^0$ Higgs boson and the mass ordering of the neutral Higgs bosons in the THDM. The fourth channel $\mu^-\mu^+ \to \tau^-\tau^+$ does not show resonances for any parameter set explored. In this production channel the interference terms are very large relative to the contributions to the total cross sections coming from the $\mu^-\mu^+ \to H^0/A^0 \to \tau^-\tau^+$ s-channel processes. This in turn means that the resonances are not visible.

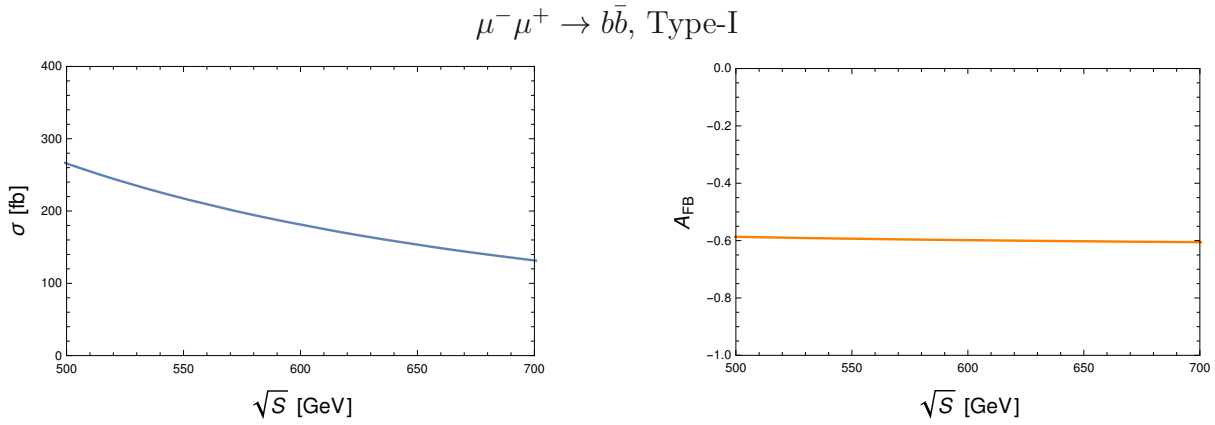


(a) (b)

Figure 6.4:
Fig. (a): total cross section as a function of $\sqrt{S}$ for the channel $\mu^-\mu^+ \to b\bar{b}$ in the Type-I THDM. Fig (b): forward-backward asymmetry $A_{FB}$ as a function of $\sqrt{S}$. The parameters are $\{0.971, 4.067, 125., 106.697, 603.485, 597.127, -5.601\}$, with $\lambda_{1,2,3,4} = \{1.0548, 0.184407, 11.0873, -5.35799\}$, and $BR = 0.743$ and $MR = 18204.6$. Here the $BR$ and $MR$ have been calculated for $m_{H^0}$, i.e. we have looked for a point which maximizes the $H^0$ resonance.

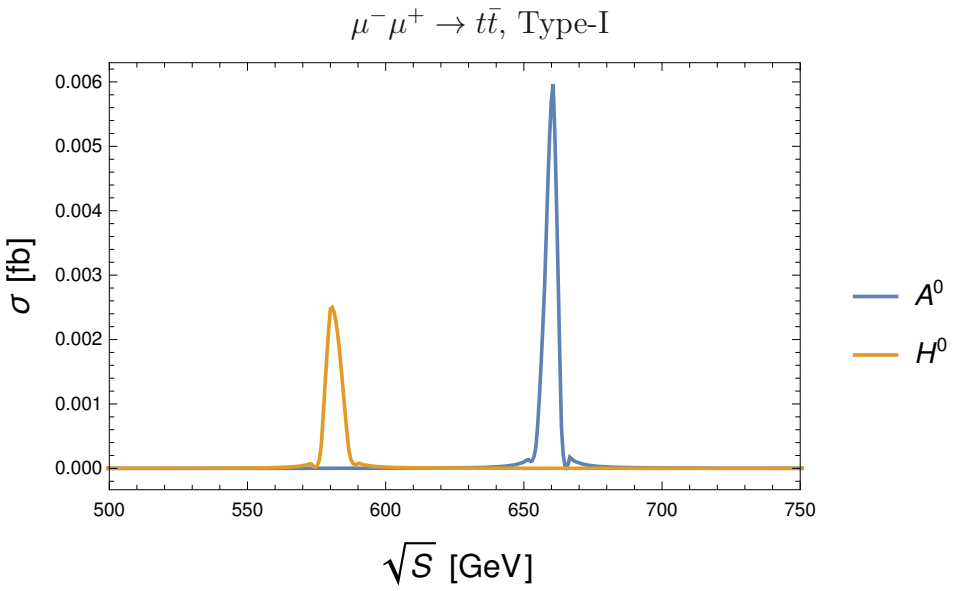


Figure 6.5:
Single cross sections for the channels $\mu^-\mu^+ \to H^0/A^0 \to t\bar{t}$ in the Type-I THDM. The parameters are $\{-0.07, 14.537, 125., 581.538, 659.398, 662.054, -1.547\}$ and the BR and MR are 0.98807 and 6803.85 respectively.

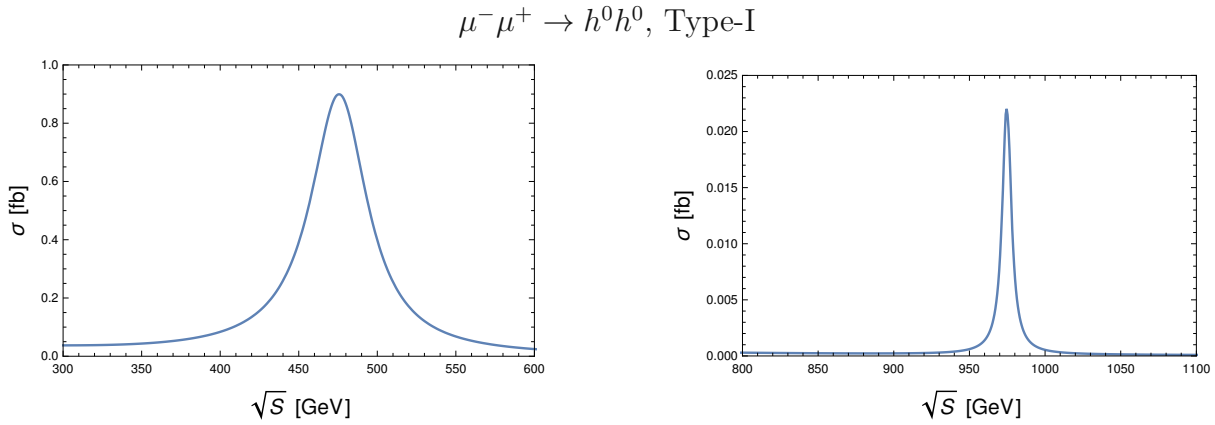


(a) (b)

Figure 6.6:
Cross section $\sigma_{\text{tot},h^0h^0}$ as a function of $\sqrt{S}$ in the Type-I THDM. The parameters in Fig. (a) are $\{-0.762, 1.798, 125., 475.473, 545.115, 570.972, -4.586\}$ with $\lambda_{1,2,3,4} = \{6.53395, 2.82781, 6.34312, -5.50468\}$, whereas in Fig. (b) they are $\{-0.360237, 2.80087, 125., 974.729, 1050.57, 1050.38, -3.20274\}$, with $\lambda_{1,2,3,4} = \{3.9957, 0.625551, 4.97306, -3.19003\}$. The $BRs$ are respectively 0.711374 and 0.0307972, and the $MRs$ are 10.8161 and 136.5 respectively.

## 6.2 Type-II THDM

Similarly to Section 6.1, we present the numerical results for the $H^0$ and $A^0$ Higgs boson resonant production, within the Type-II THDM and the four channels we investigate ($\mu^-\mu^+ \to t\bar{t}$, $\mu^-\mu^+ \to b\bar{b}$, $\mu^-\mu^+ \to h^0h^0$, $\mu^-\mu^+ \to \tau^-\tau^+$).

To illustrate the overall resonance picture in the Type-II THDM, we compare specific benchmark scenarios. In Figs. 6.7a,6.7b and 6.8b we show the total cross sections for the channel $\mu^-\mu^+ \to t\bar{t}$, in the context of a Type-II THDM. Differently from the Type-I THDM (see Section 6.1), we observe large resonances, which would certainly be observable in a future Muon Collider (see Fig. 6.7a and 6.7b). Moreover, both the $H^0$ and $A^0$ resonances are clearly visible. However, we note that the $BR$ and $MR$ for the specific parameter set must be large enough. This is clearly visible when comparing these factors for the three benchmark examples shown. In particular, the set presented in Fig. 6.8b does not show any resonance. This is due to the fact, that even though the $BR$ is very large ($\approx 99.9\%$), the $MR$ is small ($\approx 12.7$) compared to the other two parameter sets. In Fig. 6.8b we show the single cross sections for the the channels $\mu^-\mu^+ \to H^0/A^0 \to t\bar{t}$. The order of magnitude of the single cross sections is much smaller than the order of magnitude of the total cross section. This resonant peak is also not visible in the forward-backward asymmetry $A_{FB}$.

In the $\mu^-\mu^+ \to b\bar{b}$ channel, the resonant peaks are also visible, as shown in Figs. 6.9a and 6.10a. The parameter set in Fig. 6.9a shows two clearly distinct peaks corresponding to the $H^0$ and $A^0$ resonance peaks. Moreover, by observing the single cross sections for the

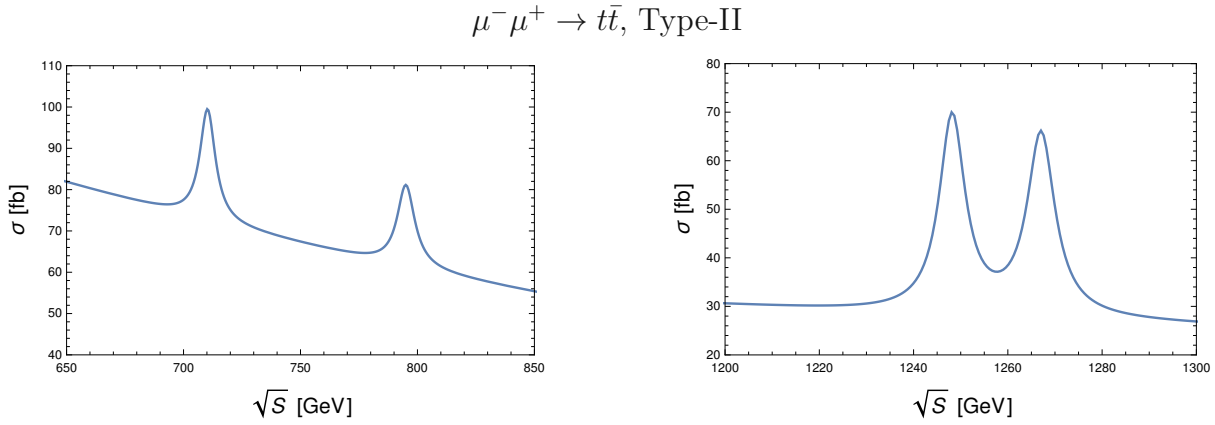


(a) (b)

Figure 6.7:
Cross section $\sigma_{\text{tot},t\bar{t}}$ as a function of $\sqrt{S}$ in the Type-II THDM. The parameters in Fig. (a) are $\{-0.458, 2.142, 125., 794.981, 710.24, 809.274, 0.119\}$ with $\lambda_{1,2,3,4} = \{7.32857, 1.03347, 2.27999, -4.67149\}$, whereas in Fig. (b) they are $\{-0.296, 3.261, 125., 1248.15, 1267.03, 1282.89, -1.288\}$ with $\lambda_{1,2,3,4} = \{5.43307, 0.343379, 3.36632, -2.57542\}$. The $BRs$ are respectively 0.931 and 0.912, and the $MRs$ are 87.753 and 188.452 respectively.

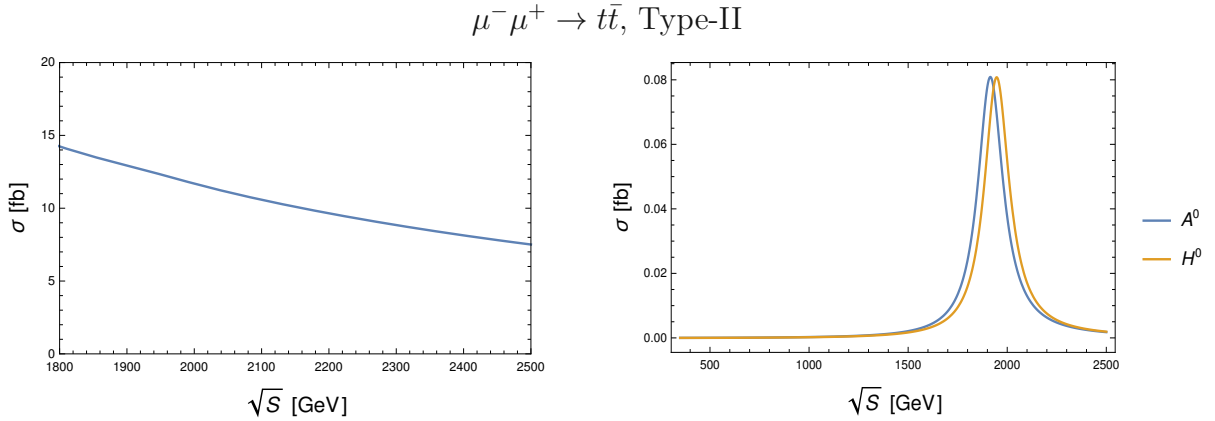


(a) (b)

Figure 6.8:
Fig. (a): cross section $\sigma_{\text{tot},t\bar{t}}$ as a function of $\sqrt{S}$ in the Type-II THDM. Fig. (b): single cross sections for the channels $\mu^-\mu^+ \to H^0/A^0 \to t\bar{t}$. The parameters are $\{-0.769, 0.832, 125., 1943.7, 1911.72, 1915.85, -3.460\}$, with $\lambda_{1,2,3,4} = \{3.95945, 8.14403, 2.25897, -3.96322\}$, and $BR = 0.999$ and $MR = 12.735$.

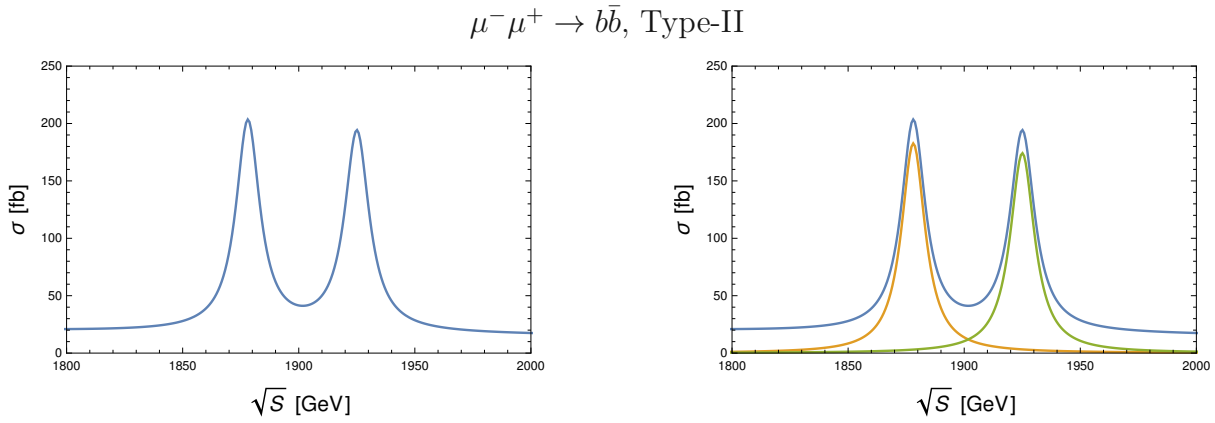


(a) (b)

Figure 6.9:
Fig. (a): cross section $\sigma_{\text{tot},b\bar{b}}$ as a function of $\sqrt{S}$ in the Type-II THDM. Fig. (b): total cross section and single cross sections for the channels $\mu^-\mu^+ \to H^0/A^0 \to b\bar{b}$. The parameters are $\{-0.074, 11.846, 125., 1878.06, 1925.02, 1887.22, -2.765\}$, with $\lambda_{1,2,3,4} = \{1.98774, 0.158098, 7.95201, 1.82236\}$, and $BR = 0.877$ and $MR = 151.229$.

channels $\mu^-\mu^+ \to H^0/A^0 \to t\bar{t}$ we note how the contributions from the $\gamma$ and $Z^0$ mediated Feynman diagrams do not prevail over the Higgs boson mediated channels, thus making the $H^0$ and $A^0$ resonances observable. Furthermore, the distance between the two peaks is large enough to guarantee the observability of the two distinct resonances. This is not the case for the second parameter set we present (see Fig. 6.10a). Here the two peaks are not clearly distinguishable from one another. This is due to the fact that the mass splitting between the $H^0$ and $A^0$ Higgs bosons is only $\approx 4$ GeV. However, the odd shape of the peak does show the presence of a double resonance. In Fig. 6.10b we show the total cross section and the single cross sections for the the channels $\mu^-\mu^+ \to H^0/A^0 \to b\bar{b}$, from which we infer that the contributions from the $\gamma$ and $Z^0$ mediated Feynman diagrams are larger relative to the parameter set in Fig. 6.9a. Both parameter sets have a large $BR > 87\%$ and a $MR > 100$. This ensures the visibility of the resonances. Moreover, if a parameter set has a large $BR$ but $MR$ below 100, the resonance peaks are no longer visible.

Similarly to Section 6.1, the $\mu^-\mu^+ \to h^0h^0$ channel shows resonant peaks for the $H^0$ Higgs boson. Also in this case we make use of the $BR$ and the $MR$ to numerically verify if a resonance can be observed. Depending on the $BR$ and $MR$ we observe different resonant peak widths and heights. In Figs. 6.11a and 6.11b we show the total cross section for the $\mu^-\mu^+ \to h^0h^0$ production process. Similarly to the Type-I and Type-II THDMs, we observe large resonances with different widths and relative heights depending on the corresponding $BR$ and $MR$.

Furthermore, in the Type-II THDM we observe resonances also in the $\mu^-\mu^+ \to \tau^-\tau^+$ production channels (see Figs. 6.12a and 6.12b). We note that even though the branching ratios are small ($\approx 4\%$) the $MRs$ enable the observability of the resonances.

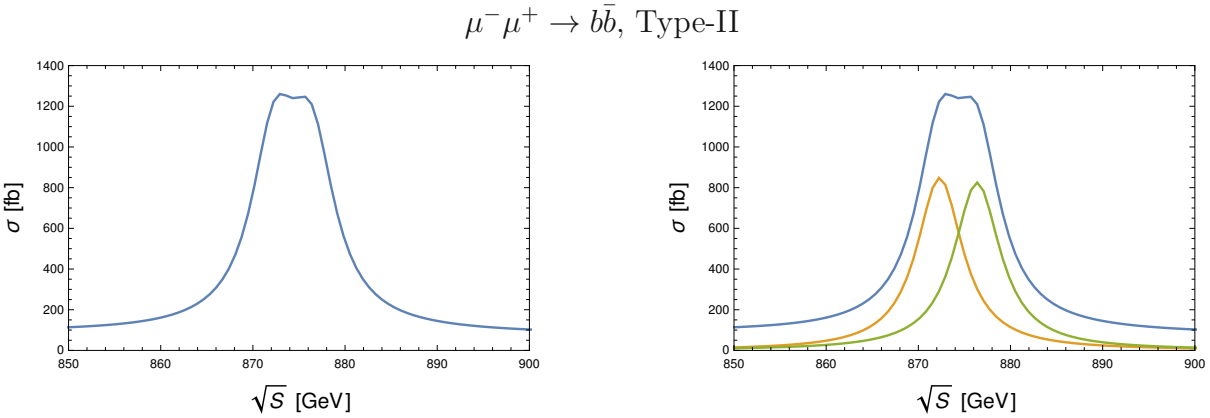


(a) (b)

Figure 6.10:
Fig. (a): cross section $\sigma_{\text{tot},b\bar{b}}$ as a function of $\sqrt{S}$ in the Type-II THDM. Fig. (b): total cross section and single cross sections for the channels $\mu^-\mu^+ \to H^0/A^0 \to b\bar{b}$. The parameters are $\{-0.049, 12.118, 125., 872.292, 876.359, 813.363, -0.108\}$ with $\lambda_{1,2,3,4} = \{7.13693, 0.196562, 1.86059, 3.28059\}$, and $BR = 0.878$ and $MR = 144.326$.

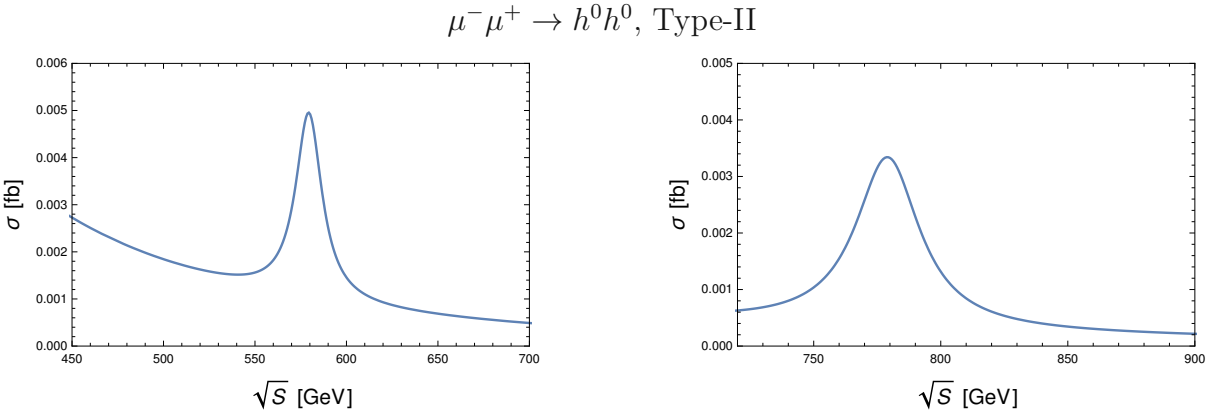


(a) (b)

Figure 6.11:
Cross section $\sigma_{\text{tot},h^0h^0}$ as a function of $\sqrt{S}$ in the Type-II THDM. The parameters in Fig. (a) are $\{-0.631, 1.270, 125., 579.379, 392.601, 575.231, -0.710\}$ with $\lambda_{1,2,3,4} = \{5.84898, 2.60794, 3.65952, -6.33681\}$, whereas in Fig. (b) they are $\{-0.691, 1.103, 125., 779.018, 635.06, 756.278, -0.127\}$ with $\lambda_{1,2,3,4} = \{3.79576, 3.46804, 2.46882, -5.49596\}$. The $BRs$ are respectively 0.995 and 0.996819, and the $MRs$ are 88.337 and 31.118 respectively.

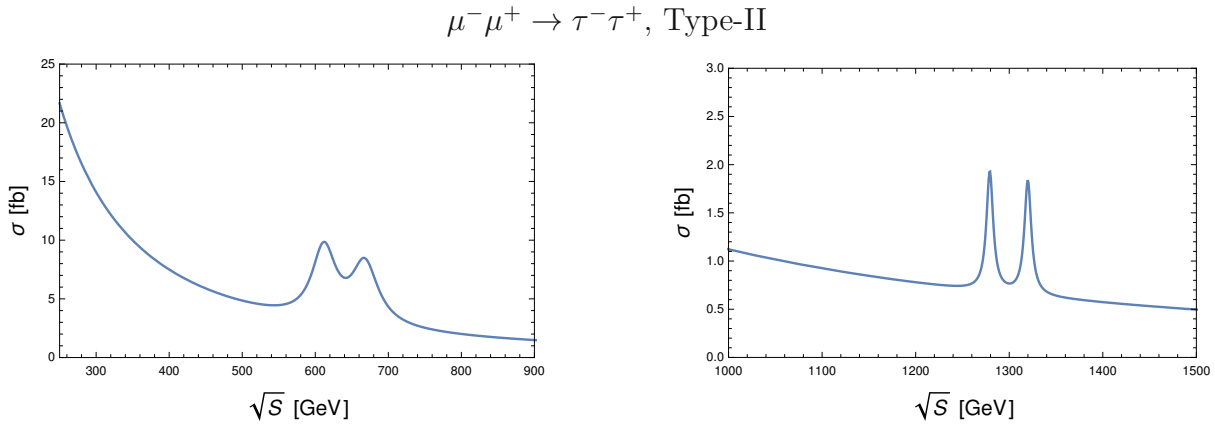


(a) (b)

Figure 6.12:
Cross section $\sigma_{\text{tot},\tau^-\tau^+}$ as a function of $\sqrt{S}$ in the Type-II THDM. The parameters in Fig. (a) are $\{-0.0242, 38.805, 125., 611.191, 667.244, 675.062, -1.142\}$ with $\lambda_{1,2,3,4} = \{3.0057, 0.248259, 3.21046, -1.47607\}$, whereas in Fig. (b) they are $\{-0.073, 12.098, 125., 1319.86, 1279.2, 1358.73, 1.672\}$ with $\lambda_{1,2,3,4} = \{7.62303, 0.20846, 6.68343, -5.00659\}$. The $BRs$ are respectively 0.046 and 0.0437, and the $MRs$ are 15.339 and 149.21 respectively.

## 6.3 Lepton-specific THDM

Here we present the numerical results for the $H^0$ and $A^0$ Higgs boson resonant production, within the lepton-specific THDM and the four channels we investigate ($\mu^-\mu^+ \to t\bar{t}$, $\mu^-\mu^+ \to b\bar{b}$, $\mu^-\mu^+ \to h^0h^0$, $\mu^-\mu^+ \to \tau^-\tau^+$).

To illustrate the overall resonance picture in the lepton-specific THDM, we compare specific benchmark scenarios. Fig. 6.13a and 6.13b show the total cross section in the lepton-specific THDM for the $\mu^-\mu^+ \to t\bar{t}$ channel. We observe two resonances for the $H^0$ and $A^0$ Higgs bosons. Moreover, we note how numerical instabilities cause artifacts at the tails of the two resonant peaks (see Fig. 6.13a). These can be alleviated by increasing the accuracy of integration when calculating the total cross section $\sigma_{\text{tot},t\bar{t}}$. In Fig. 6.13b there are no visible artifacts due to the tenfold increase in the integration accuracy.

Differently from the $\mu^-\mu^+ \to t\bar{t}$ production channel, the $\mu^-\mu^+ \to b\bar{b}$ channel does not show visible resonances. They are suppressed by the Yukawa couplings for bottom-type quarks. These resonant peaks are also not visible in the forward-backward asymmetry.

In Fig. 6.15a we show the total cross section for the $\mu^-\mu^+ \to h^0h^0$ channel. We observe a large resonant peak for the $H^0$ Higgs boson. In Fig. 6.15b we show the single cross sections for the $\mu^-\mu^+ \to h^0/H^0 \to h^0h^0$ channels. We see how the $H^0$ contribution to the total cross section is much larger than the contribution from the SM-like $h^0$ Higgs boson, thus making the $H^0$ resonance clearly visible.

Similarly to the $t\bar{t}$- channel, in the $\mu^-\mu^+ \to \tau^-\tau^+$ production channel we observe large resonant peaks for both the $H^0$ and $A^0$ neutral Higgs bosons.

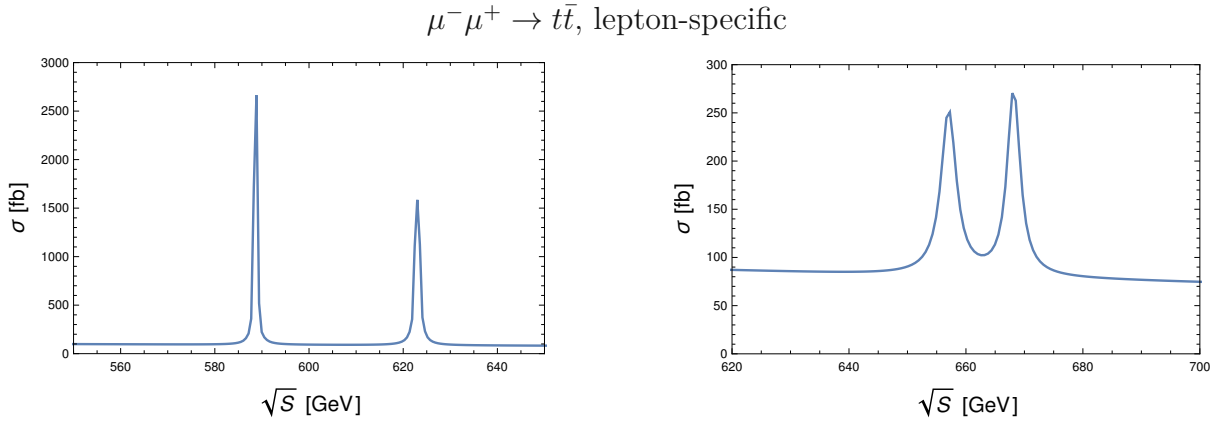


(a) (b)

Figure 6.13:
Cross section $\sigma_{\text{tot},t\bar{t}}$ as a function of $\sqrt{S}$ in the lepton-specific THDM. The parameters in Fig. (a) are $\{-0.176, 5.933, 125., 588.64, 623.004, 628.328, -0.737\}$ with $\lambda_{1,2,3,4} = \{2.2238, 0.268968, 1.55975, -0.94908\}$, whereas in Fig. (b) they are $\{-0.313, 3.211, 125., 668.15, 657.037, 667.835, -0.468\}$ with $\lambda_{1,2,3,4} = \{6.74976, 0.388707, 0.614593, -0.923415\}$. The $BRs$ are respectively 0.909 and 0.973, and the $MRs$ are 948.694 and 254.197 respectively.

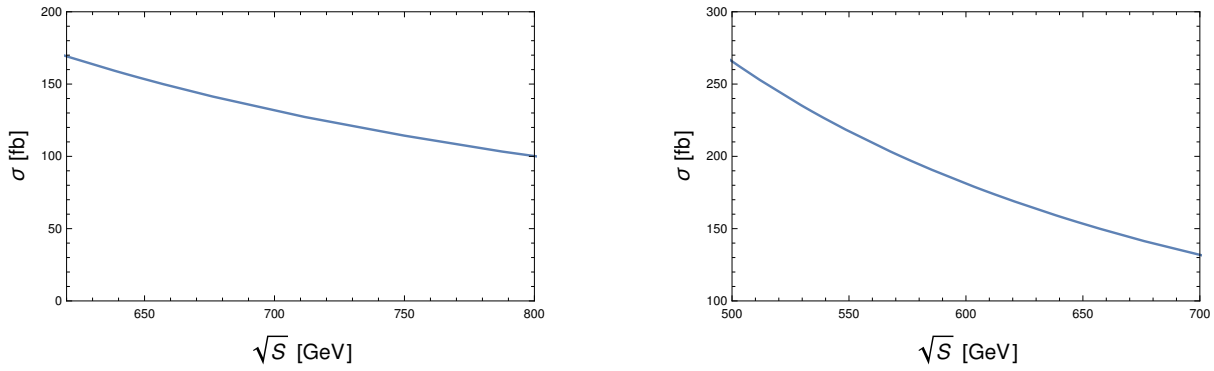


(a) (b)

Figure 6.14:
Cross section $\sigma_{\text{tot},b\bar{b}}$ as a function of $\sqrt{S}$ in the lepton-specific THDM. The parameters in Fig. (a) are $\{-0.085, 10.403, 125., 670.556, 748.066, 664.854, -1.749\}$ with $\lambda_{1,2,3,4} = \{1.57651, 0.235231, 0.770578, 1.99378\}$, whereas in Fig. (b) they are $\{-0.07, 11.381, 125., 615.889, 595.479, 599.964, 0.393\}$ with $\lambda_{1,2,3,4} = \{2.40405, 0.232599, 0.785706, 0.22232\}$. The $BRs$ are respectively 0.832 and 0.981, and the $MRs$ are 1936.8 and 2086.17 respectively.

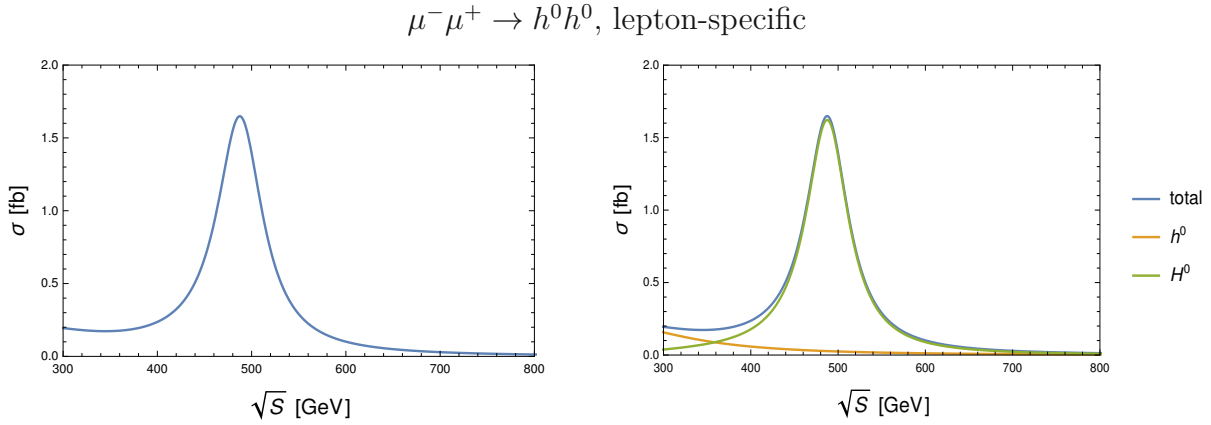


(a) (b)

Figure 6.15:
Fig. (a): cross section $\sigma_{\text{tot},h^0h^0}$ as a function of $\sqrt{S}$ in the lepton-specific THDM. Fig. (b): total cross section and single cross sections for the channels $\mu^-\mu^+ \to H^0/A^0 \to h^0h^0$. The parameters are $\{-0.772, 1.884, 125., 487.205, 594.273, 585.347, -4.929\}$ with $\lambda_{1,2,3,4} = \{5.16173, 2.81989, 6.03283, -4.5938\}$, and $BR = 0.733$ and $MR = 8.278$.

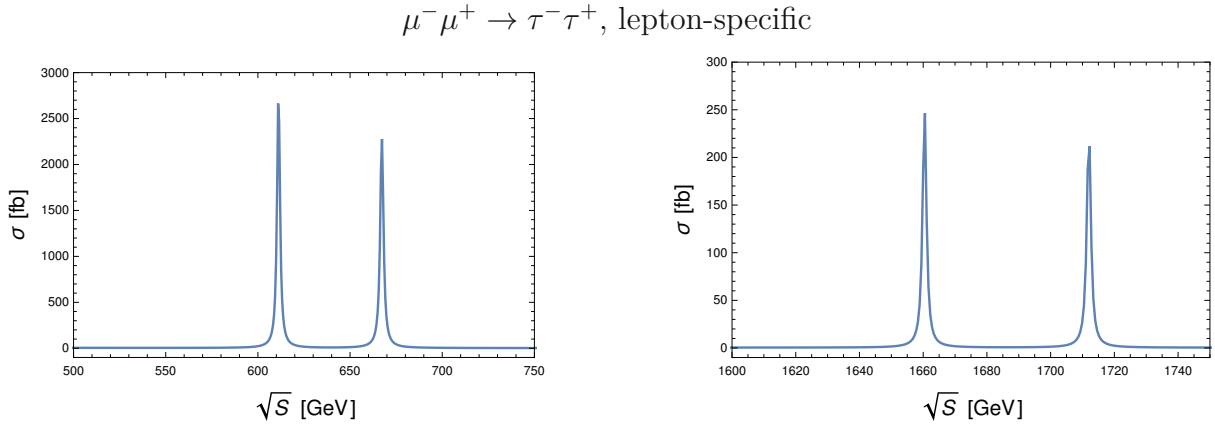


(a) (b)

Figure 6.16:
Figs. (a) and (b): total cross sections $\sigma_{\text{tot},\tau^-\tau^+}$ as a function of $\sqrt{S}$ in the lepton-specific THDM. The parameters are respectively $\{-0.0242, 38.805, 125., 611.191, 667.244, 675.062, -1.142\}$ with $\lambda_{1,2,3,4} = \{3.0057, 0.248259, 3.21046, -1.47607\}$, and with $BR = 0.99$ and $MR = 328.858$, and $\{-0.049, 18.612, 125., 1660.42, 1712., 1655.95, -2.751\}$ with $\lambda_i = \{1.33711, 0.227757, 3.53244, 3.25841\}$ $(i = 1, ..., 4)$, and with $BR = 0.893$ and $MR = 1162.06$.

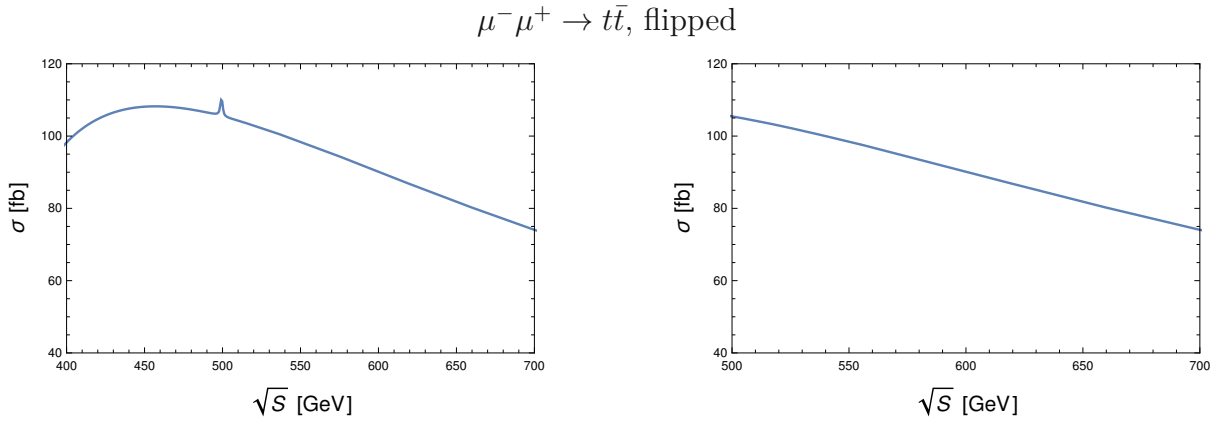


(a) (b)

Figure 6.17:
Figs. (a) and (b): total cross sections $\sigma_{\text{tot},t\bar{t}}$ as a function of $\sqrt{S}$ in the flipped THDM. The parameters are respectively $\{-0.725, 1.934, 125., 490.519, 577.862, 575.914, -4.454\}$ with $\lambda_{1,2,3,4} = \{6.00369, 2.47272, 5.31535, -4.38277\}$, and with $BR = 0.71$ and $MR = 11.9823$, and $\{-0.842, 1.999, 125., 466.549, 638.314, 656.784, -5.858\}$ with $\lambda_{1,2,3,4} = \{3.40234, 3.00647, 9.45549, -6.61916\}$, and with $BR = 0.599$ and $MR = 3.112$.

## 6.4 Flipped THDM

In this Section we present the numerical results for the $H^0$ and $A^0$ Higgs boson resonant production, within the flipped THDM and the four channels we investigate ($\mu^-\mu^+ \to t\bar{t}$, $\mu^-\mu^+ \to b\bar{b}$, $\mu^-\mu^+ \to h^0h^0$, $\mu^-\mu^+ \to \tau^-\tau^+$).

We illustrate the resonant behavior of the $H^0$ and $A^0$ Higgs bosons in the flipped THDM, by comparing specific benchmark scenarios. In Figs. 6.17a and 6.17b we show the total cross section for the production channel $\mu^-\mu^+ \to t\bar{t}$. Similarly to the Type-I THDM we do not have large and thus observable resonant peaks. This is also the case for the production processes $\mu^-\mu^+ \to b\bar{b}$ and $\mu^-\mu^+ \to \tau^-\tau^+$. However, as is the case for all the explored THDMs, the production process $\mu^-\mu^+ \to h^0h^0$ shows large resonances in the flipped THDM (see Figs. 6.18a and 6.18b).

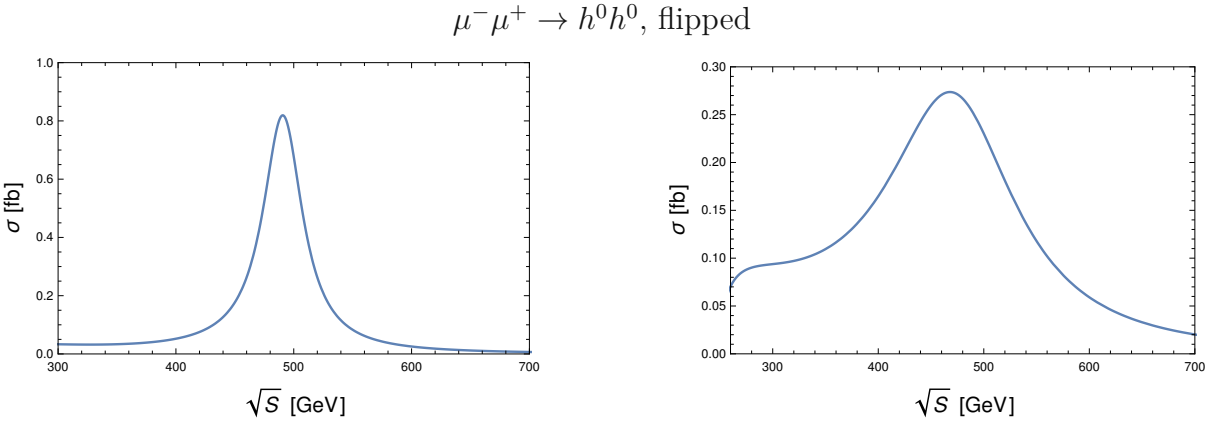


(a) (b)

Figure 6.18:
Figs. (a) and (b): total cross sections $\sigma_{\text{tot},h^0h^0}$ as a function of $\sqrt{S}$ in the flipped THDM. The parameters are respectively $\{-0.0242, 38.805, 125., 611.191, 667.244, 675.062, -1.142\}$ with $\lambda_{1,2,3,4} = \{3.0057, 0.248259, 3.21046, -1.47607\}$, and with $BR = 0.99$ and $MR = 328.858$, and $\{-0.049, 18.612, 125., 1660.42, 1712., 1655.95, -2.751\}$ with $\lambda_{1,2,3,4} = \{1.33711, 0.227757, 3.53244, 3.25841\}$, with $BR = 0.893$ and $MR = 1162.06$.

## 6.5 Discussion

In this Section we discuss the results obtained for the resonances in the four channels explored $\mu^-\mu^+ \to t\bar{t}, b\bar{b}, \tau^-\tau^+, h^0h^0$ and the four THDMs (Type-I, Type-II, lepton-specific and flipped). We show for two different parameter sets the total cross sections for all production channels and THDMs (see Tabs. 6.1 and 6.2).

For the first scenario we pick the parameter set $\{-0.458, 2.142, 125., 794.981, 710.24, 809.274, 0.119\}$. As can be seen in Tab. 6.1, the production channel $\mu^-\mu^+ \to t\bar{t}$ shows resonant peaks for the $H^0$ and $A^0$ Higgs bosons in the Type-II and lepton-specific THDMs, whereas the $\mu^-\mu^+ \to b\bar{b}$ does not show any resonant peak for all four THDMs. As expected from the previous sections, the $\mu^-\mu^+ \to h^0h^0$ channel shows a resonant peak for the $H^0$ Higgs boson in all four THDMs. Similarly to the $\mu^-\mu^+ \to b\bar{b}$ channel, the $\mu^-\mu^+ \to \tau^-\tau^+$ production channel does not show resonant peak for any of the explored THDMs. In conclusion we note that for this specific benchmark scenario, resonant peaks for both the $H^0$ and $A^0$ Higgs bosons could be observed in a future Muon Collider for the Type-II and lepton-specific THDMs. However, only a resonant peak for the $H^0$ Higgs boson could be observed in the Type-I and flipped THDMs.

For the second benchmark case we pick the parameter set $\{-0.074, 11.846, 125., 1878.06, 1925.02, 1887.22, -2.765\}$ (see Tab. 6.2). Similarly to the first case, the $\mu^-\mu^+ \to t\bar{t}$ production channel presents two resonant peaks for the $H^0$ and $A^0$ Higgs bosons in the Type-II and lepton-specific THDMs. However, for the Type-I and flipped THDMs we do not observe any resonant peak for this specific parameter set. However, differently from the first benchmark scenario, the $\mu^-\mu^+ \to b\bar{b}$ production channel does show a "double

peak" for the $H^0$ and $A^0$ Higgs bosons in the Type-II THDM. In the remaining Type-I, lepton-specific and flipped THDMs we do not observe any resonant peak. As expected, also in this case the $\mu^-\mu^+ \to h^0h^0$ channel shows a resonant peak for the $H^0$ Higgs boson in all four THDMs. However, here they vary significantly in width depending on the specific THDM. Differently from the first scenario, the $\mu^-\mu^+ \to \tau^-\tau^+$ production channel shows resonant peaks for both the $H^0$ and $A^0$ Higgs bosons in the Type-II and lepton-specific THDMs.

All results presented in this work are thoroughly checked with various means. In particular, we have extended the FormCalc and FeynArts packages [8, 9] to include not only the Type-I and Type-II THDMs, but also the lepton-specific and flipped THDMs. We do so by deriving the Yukawa couplings in the same form as used by FormCalc for the already implemented THDMs. This enables us to extend the package to four THDMs (for a copy of the package please contact the authors). Furthermore, we make use of the 2HDMC package [10] to verify single total cross section values for a specific THDM and parameter set. Furthermore, we have developed a *python* code that is able to compute the total cross section for the explored processes in any of the four investigated THDMs, and then compute the relative height of the resonant peaks. As input the code takes the theoretically and experimentally allowed parameter sets as well as the relative height deemed necessary to observe a resonant peak in an experiment, in percentage. The code enables one to calculate the percentage of parameter sets that show large enough resonant peaks in any of the four channels and THDMs considered in this study. This in turn gives a quantitative estimate of the parameter space that can be covered in a future Muon Collider, with the aim of proving or disproving the THDM. Furthermore, it gives a direct measure on the research potential of a future Muon Collider in the context of a THDM and more specifically in the search for the additional neutral $H^0$ and $A^0$ Higgs bosons predicted by the THDM. Moreover, due to the fact that the $BRs$ and $MRs$ needed to observe a resonant peak are model and production process dependent, this code also gives the possibility to quantitatively compare production processes for the investigated THDMs. This code can be easily extended to include further production processes and THDMs. E.g. the inert THDM, which can also provide a dark matter candidate.

In conclusion, we argue that the large Yukawa coupling of the muon and the specific structure of the THDM, would enable a future Muon Collider to effectively search for additional scalar and neutral Higgs bosons in the form of resonant peaks in the total cross section of the investigated production channels. Furthermore, the model specific Yukawa couplings suppress or enhance the resonant peaks in the different THDMs for a specific production process. We argue that this would give further insight into the exact nature of the potentially discovered additional Higgs bosons. In particular it would restrict the number of viable THDMs, since e.g. a specific resonant peak should only be observable in the Type-II THDM and not in the remaining three THDMs.

| Model: | Type-I | Type-II | lepton-specific | flipped |
|---|---|---|---|---|
| $t\bar{t}$ | 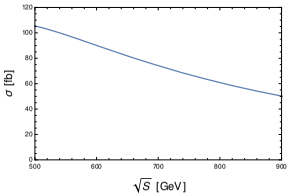 | 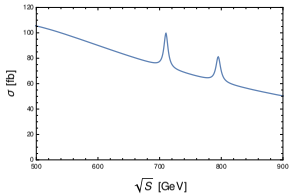 | 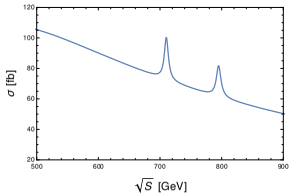 | 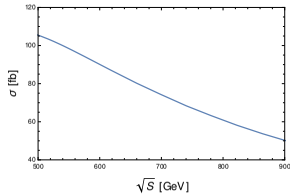 |
| $b\bar{b}$ | 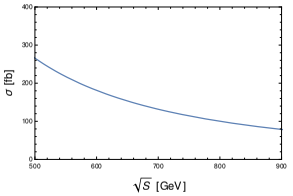 | 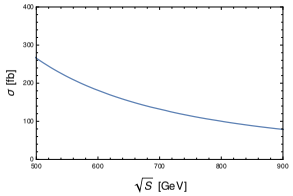 | 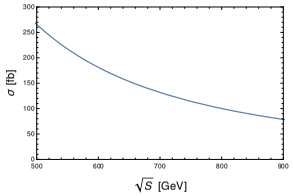 | 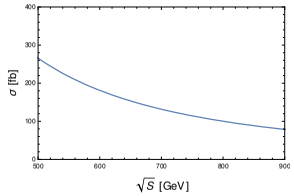 |
| $h^0h^0$ | 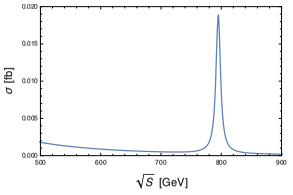 | 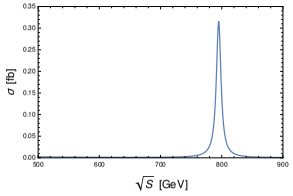 | 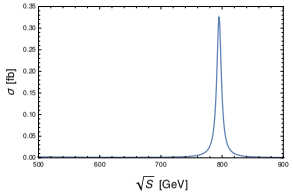 | 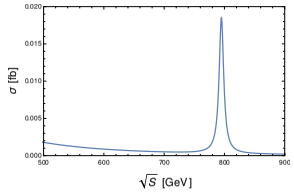 |
| $\tau^-\tau^+$ | 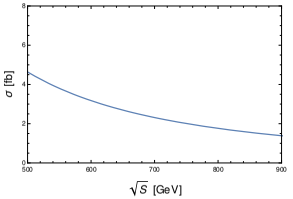 | 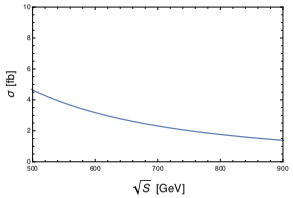 | 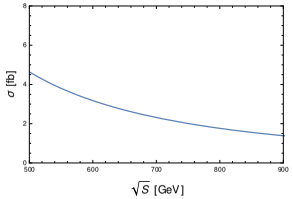 | 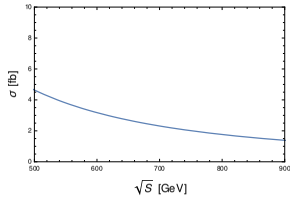 |

Table 6.1: Comparison of the cross sections $\sigma_{\text{tot}}$ as a function of the center of mass energy $\sqrt{S}$ for all investigated channels and THDMs. The parameters are $\{-0.458, 2.142, 125., 794.981, 710.24, 809.274, 0.119\}$. This parameter set has $BR = 0.931$ and $MR = 87.753$ for the $\mu^-\mu^+ \to t\bar{t}$ channel in the Type-II THDM.

| Model: | Type-I | Type-II | lepton-specific | flipped |
|---|---|---|---|---|
| $t\bar{t}$ | 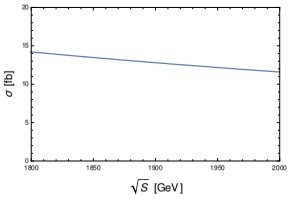 | 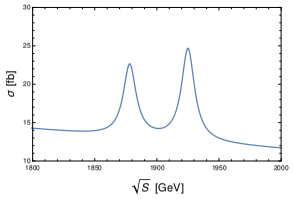 | 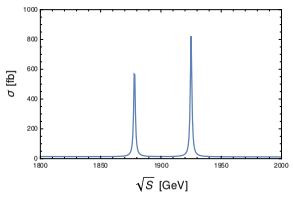 | 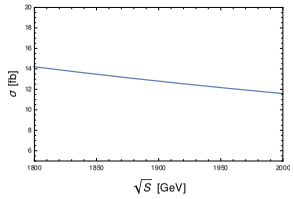 |
| $b\bar{b}$ | 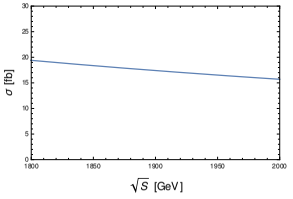 | 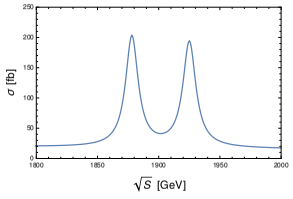 | 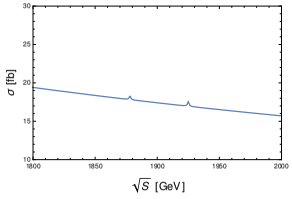 | 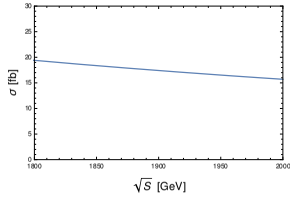 |
| $h^0h^0$ | 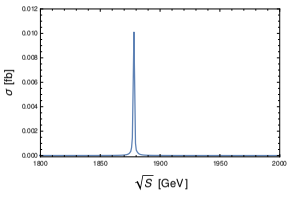 | 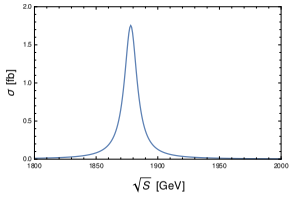 | 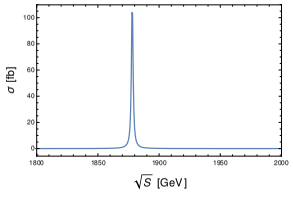 | 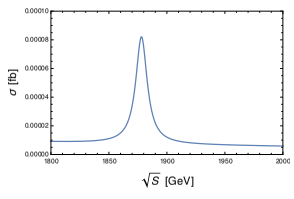 |
| $\tau^-\tau^+$ | 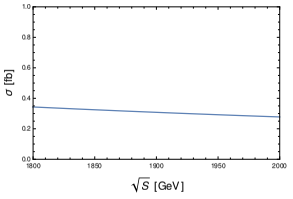 | 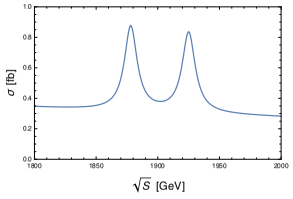 | 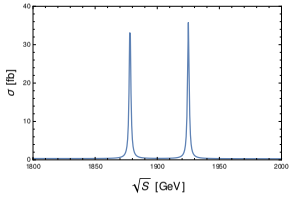 | 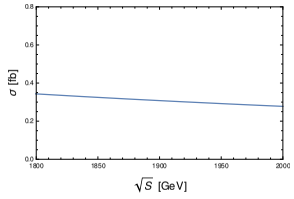 |

Table 6.2: Comparison of the cross sections $\sigma_{\text{tot}}$ as a function of the center of mass energy $\sqrt{S}$ for all investigated channels and THDMs. The parameters are $\{-0.074, 11.846, 125., 1878.06, 1925.02, 1887.22, -2.765\}$. This parameter set has $BR = 0.877$ and $MR = 151.229$ for the $\mu^-\mu^+ \to b\bar{b}$ channel in the Type-II THDM.

# Chapter 7

# Conclusions and outlook

In this work, we have studied the phenomenology of various non-supersymmetric Two Higgs Doublet Models (THDMs) with real parameters for a future Muon Collider. Specifically, we have explored the Type-I, Type-II, lepton-specific, and flipped THDMs by studying the resonant behavior of the predicted neutral $H^0$ and $A^0$ Higgs bosons in the scattering processes: $\mu^-\mu^+ \to t\bar{t}$, $\mu^-\mu^+ \to b\bar{b}$, $\mu^-\mu^+ \to h^0h^0$, and $\mu^-\mu^+ \to \tau^-\tau^+$. We have derived the decay widths of the $H^0$ and $A^0$ Higgs bosons at the tree level to determine their corresponding branching ratios (BRs) and Breit-Wigner propagators.

Furthermore, we have derived from first principles all theoretical bounds, e.g., unitarity, global minimum, vacuum stability, and oblique parameters (S, T, U), as well as explored the relevant experimental bounds. We then performed a comprehensive numerical study of the theoretical bounds by developing a Python code, with which we have calculated the allowed THDM parameter sets: $\{s_\alpha, t_\beta, m_{h^0}, m_{H^0}, m_{A^0}, m_{H^\pm}, \lambda_5\}$. In particular, we have performed a parameter scan of more than 20 billion randomly selected parameter sets and found over 200000 allowed sets.

Using these sets, we have performed a detailed numerical study of the resonant behavior of the $H^0$ and $A^0$ Higgs bosons in the production processes $\mu^-\mu^+ \to t\bar{t}$, $b\bar{b}$, $h^0h^0$, and $\tau^-\tau^+$. We have checked the correctness of our calculations by extending the FA/FC packages [8, 9] to include all four investigated THDMs and by verifying all decay widths for specific parameter sets and center of mass energies using the 2HDMC package [10].

In the Type-I THDM, we find that only the $\mu^-\mu^+ \to h^0h^0$ production channel produces $H^0$ resonances that could be observed at a future Muon Collider. However, due to $A^0$ being CP-odd, no $A^0$ Higgs boson s-channel production channel is present in $\mu^-\mu^+ \to h^0h^0$. All other channels do not show any resonances for the $H^0$ and $A^0$ Higgs bosons. This is due to the large contributions from the $\gamma$ and $Z^0$ mediated s-channel processes, which do not appear in the $\mu^-\mu^+ \to h^0h^0$ production channel. Moreover, in this model all channels are suppressed by the fermion Yukawa couplings $Y_{u,d,l} \backsim 1/t_\beta$ (see Tab. 1.2), which enter quadratically for the channels $\mu^-\mu^+ \to t\bar{t}, b\bar{b}$ and $\tau^-\tau^+$, and linearly for the $\mu^-\mu^+ \to h^0h^0$ production channel. In contrast, the Type-II THDM shows both $H^0$ and $A^0$ resonances in the channels $\mu^-\mu^+ \to t\bar{t}$, $b\bar{b}$ and $\tau^-\tau^+$. This is due to the different Yukawa couplings which enhance the resonant peaks and thus alleviate the suppression

due to the $\gamma$ and $Z^0$ mediated s-channel processes. In particular, the channel $\mu^-\mu^+ \to t\bar{t}$ is not suppressed by $t_\beta$ and the $\mu^-\mu^+ \to b\bar{b}, \tau^-\tau^+$ production channels are quadratically enhanced with $t_\beta^2$ (see Tab. 1.2). In contrast to the Type-I and Type-II THDMs, the lepton-specific THDM shows large resonant peaks for both the $H^0$ and $A^0$ Higgs bosons for the production processes $\mu^-\mu^+ \to t\bar{t}$, $h^0h^0$ and $\tau^-\tau^+$ (note that in the $\mu^-\mu^+ \to h^0h^0$ channel only the $H^0$ Higgs boson can be observed). In this model the $\mu^-\mu^+ \to t\bar{t}, b\bar{b}$ processes are not enhanced by $t_\beta$. However, due to the large top-quark mass, resonant peaks are visible in the $\mu^-\mu^+ \to t\bar{t}$ channel. Furthermore, the $\mu^-\mu^+ \to \tau^-\tau^+$ process is quadratically enhanced with $t_\beta^2$ (see Tab. 1.2), and thus shows large resonant peaks. Similarly to the Type-I THDM the flipped THDM only shows resonant peaks for the $\mu^-\mu^+ \to h^0h^0$ production channel. This is due to the fact that also in this case the $\mu^-\mu^+ \to t\bar{t}, \tau^-\tau^+$ production processes are quadratically suppressed by $t_\beta$, whereas the $\mu^-\mu^+ \to b\bar{b}$ process is not enhanced by $t_\beta$ and the mass of the bottom-quark is not large enough.

In conclusion, we argue that $H^0$ and $A^0$ Higgs boson resonances can be observed for a large number of allowed parameter sets at a future Muon Collider for various THDMs. Moreover, due to the different Yukawa couplings, resonances may be observed in a specific s-channel only in certain THDMs. Even though this could be perceived as a limit, we argue that it actually provides further information on the true nature of the potentially discovered scalar particles. In particular, if a future Muon Collider observes a resonance for a parameter set whose resonance we argue should only be visible e.g. in the Type-I THDM, then we have a strong hint that this model could be the one realized in nature. Its worth to note that even in the case that $H^0$ is already observed in a direct production channel, with the technique discussed in this work, we possibly can measure the total width of $H^0$. Similar arguments hold for $A^0$. Thus, we propose to consider $\sqrt{S}$-scans at a future MC.

This study is only a first step in the exploration of the rich phenomenology offered by various THDMs in the context of such resonances at a future Muon Collider. In particular, unlike an $e^+e^-$ collider, the large muon Yukawa coupling enables an efficient s-channel neutral Higgs boson exchange, making the search for $H^0$ and $A^0$ Higgs boson resonances particularly enticing. Future works could consider an extension to complex as well as supersymmetric THDMs, which is of particular interest since the THDM is not only a natural extension of the SM but also a prerequisite for supersymmetric models (SUSY) (see e.g. [6] for similar work). Furthermore, the less strict theoretical and experimental bounds for a supersymmetric THDM allow the search for $H^0$ and $A^0$ Higgs boson resonances well above 1 TeV. Considering the proposed Muon Collider at CERN operating at around 3 and 10 TeV, this scenario could become particularly interesting.

Moreover, the *python* code we have developed could be expanded to include the current experimental bounds, providing the possibility to perform an up-to-date comprehensive parameter scan of the allowed parameter sets considering both theoretical and experimental bounds.

# Acknowledgements

I am deeply honored to express my heartfelt gratitude to my esteemed thesis advisor, Dr. Helmut Eberl. His unwavering guidance and invaluable insights have illuminated my path throughout the entire research process. His mentorship, marked by constructive feedback and relentless dedication, has played an indisputable role in not only shaping the direction of this work but also in enhancing its caliber.

I extend my utmost and sincere appreciation to the distinguished members of my thesis committee: Prof. Jochen Schieck, Prof. Florian Libisch, and Prof. Josef Pradler. Their erudite contributions and rigorous examination have not only elevated my research but have also fortified its academic integrity. Their thoughtful comments and insightful suggestions have resonated deeply, enriching the depth of my study.

To my treasured colleagues and friends — Malek, Simon, and Tarun — I am profoundly grateful for the stimulating discussions and unwavering support they've provided on this journey. Their collaboration has been a beacon of intellectual camaraderie that has driven this work forward.

My sincere appreciation extends to my dear friends, Gaspare and Francesca, whose unwavering presence has been a constant source of solace and encouragement. Their unwavering belief in my abilities has been a wellspring of strength.

In this endeavor, my family and my extended family have been my bedrock. Their unswerving love and support have not only uplifted me but have also fortified my belief in my capabilities. I wish to extend special recognition to my parents, my sister, and my uncle for being the cornerstones of my journey. Their unwavering support has been the foundation upon which I've been able to pursue my dreams and become the physicist I aspired to be.

In the closing chapter of this phase, I am profoundly appreciative of every person who has played a role, no matter how big or small, in my academic odyssey. Your contributions have been the brushstrokes that have painted this portrait of achievement.

From the depth of my heart, I express my sincere gratitude.

*Grazie*

# Bibliography


1. Galilei, G. *Il Saggiatore* (Giacomo Mascardi, Rome, Italy, 1623).
2. Schulte, D. *et al. Muon Collider. A Path to the Future?* in *Proceedings of European Physical Society Conference on High Energy Physics PoS(EPS-HEP2019)* (2020).
3. Biagini, M. E. & Lucchesi, D. Muon Collider: a window to the future. *IL NUOVO SAGGIATORE BOLLETTINO DELLA SOCIETÀ ITALIANA DI FISICA* (2021).
4. Manuela Boscolo, J.-P. D. & Palmer, M. The Future Prospects of Muon Colliders and Neutrino Factories. *Reviews of Accelerator Science and Technology,* 189–214 (2019).
5. Aime, C. *et al.* Muon Collider Physics Summary. arXiv: `2203.07256 [hep-ph]` (Mar. 2022).
6. Bartl, A., Eberl, H., Kraml, S., Majerotto, W. & Porod, W. Sfermion pair production at mu+ mu- colliders. *Phys. Rev. D* **58,** 115002. arXiv: `hep-ph/9805248` (1998).
7. Eichten, E. & Martin, A. The Muon Collider as a $H/A$ Factory. *Phys. Lett. B* **728,** 125–130. arXiv: `1306.2609 [hep-ph]` (2014).
8. Hahn, T. & Pérez-Victoria, M. Automated one-loop calculations in four and D dimensions. *Computer Physics Communications* **118,** 153–165. ISSN: 0010-4655. `https://www.sciencedirect.com/science/article/pii/S0010465598001738` (1999).
9. Hahn, T. Generating Feynman diagrams and amplitudes with FeynArts 3. *Computer Physics Communications* **140,** 418–431. ISSN: 0010-4655. `https://www.sciencedirect.com/science/article/pii/S0010465501002909` (2001).
10. Eriksson, D., Rathsman, J. & Stal, O. 2HDMC: Two-Higgs-Doublet Model Calculator Physics and Manual. *Comput. Phys. Commun.* **181,** 189–205. arXiv: `0902.0851 [hep-ph]` (2010).
11. Wang, L., Yang, J. M. & Zhang, Y. Two-Higgs-doublet models in light of current experiments: a brief review. *Communications in Theoretical Physics* **74,** 097202. `https://dx.doi.org/10.1088/1572-9494/ac7fe9` (Aug. 2022).
12. Haber, H. E. & O'Neil, D. Basis-independent methods for the two-Higgs-doublet model III: The CP-conserving limit, custodial symmetry, and the oblique parameters S, T, U. *Phys. Rev. D* **83,** 055017. arXiv: `1011.6188 [hep-ph]` (2011).

13. Arhrib, A. *Unitarity constraints on scalar parameters of the standard and two Higgs doublets model* in *Workshop on Noncommutative Geometry, Superstrings and Particle Physics* (Dec. 2000). arXiv: hep-ph/0012353.

14. Arhrib, A., Benbrik, R., El Kacimi, M., Rahili, L. & Semlali, S. Extended Higgs sector of 2HDM with real singlet facing LHC data. *Eur. Phys. J. C* **80,** 13. arXiv: 1811.12431 [hep-ph] (2020).

15. Branco, G. *et al.* Theory and phenomenology of two-Higgs-doublet models. *Physics Reports* **516.** Theory and phenomenology of two-Higgs-doublet models, 1–102. ISSN: 0370-1573. https://www.sciencedirect.com/science/article/pii/S0370157312000695 (2012).

16. Heinemeyer, S. Future perspectives for Higgs physics. *PoS* **ICHEP2022,** 017. arXiv: 2211.12208 [hep-ph] (2022).

17. Celis, A., Ilisie, V. & Pich, A. LHC constraints on two-Higgs doublet models. *JHEP* **07,** 053. arXiv: 1302.4022 [hep-ph] (2013).

18. Celis, A. *LHC phenomenology of two-Higgs-doublet models in the LHC era* PhD thesis (Valencia U., 2014).

19. Thomson, M. in. 1st ed. Chap. 6 (CAMBRIDGE University Press, 2013).

20. Eberl, H. Introduction to the Models of Elementary Particle Physics I - 141.B00 (TU Wien). https://tiss.tuwien.ac.at/course/courseDetails.xhtml?dswid=2399&dsrid=31&courseNr=141B00&semester=2022W (2021).

21. Eberl, H. Introduction to the Models of Elementary Particle Physics II - 141.B02 (TU Wien). https://tiss.tuwien.ac.at/course/courseDetails.xhtml?dswid=2399&dsrid=57&courseNr=141B02&semester=2023S (2022).

22. Branco, G., Grimus, W. & Lavoura, L. Relating the scalar flavour-changing neutral couplings to the CKM matrix. *Physics Letters B* **380,** 119–126. ISSN: 0370-2693. https://www.sciencedirect.com/science/article/pii/0370269396004947 (1996).

23. Ma, E. Verifiable radiative seesaw mechanism of neutrino mass and dark matter. *Phys. Rev. D* **73,** 077301. https://link.aps.org/doi/10.1103/PhysRevD.73.077301 (7 Apr. 2006).

24. Eberl, H. *Strahlungskorrekturen im minimalen supersymmetrischen Standardmodell* PhD thesis (Vienna University of Technology, 1998).

25. Srednicki, M. *Quantum Field Theory* (Cambridge University Press, 2007).

26. Barroso, A., Ferreira, P. M., Ivanov, I. P. & Santos, R. Metastability bounds on the two Higgs doublet model. *JHEP* **06,** 045. arXiv: 1303.5098 [hep-ph] (2013).

27. Chen, N., Du, C., Wu, Y. & Xu, X.-J. Further study of the global minimum constraint on the two-Higgs-doublet models: LHC searches for heavy Higgs bosons. *Phys. Rev. D* **99,** 035011. arXiv: 1810.04689 [hep-ph] (2019).

28. Kanemura, S., Kubota, T. & Takasugi, E. Lee-Quigg-Thacker bounds for Higgs boson masses in a two doublet model. *Phys. Lett. B* **313,** 155–160. arXiv: hep-ph/9303263 (1993).

29. Peskin, M. E. & Schroeder, D. V. *An Introduction to Quantum Field Theory* Reading, USA: Addison-Wesley (1995) 842 p (Westview Press, 1995).

30. Valencia, G. & Willenbrock, S. The Goldstone Boson Equivalence Theorem and the Higgs Resonance. *Phys. Rev. D* **42,** 853–859 (1990).

31. Delahaye, J. P. *et al.* Muon Colliders. arXiv: 1901.06150 [physics.acc-ph] (Jan. 2019).

32. Peskin, M. E. & Takeuchi, T. Estimation of oblique electroweak corrections. *Phys. Rev. D* **46,** 381–409. https://link.aps.org/doi/10.1103/PhysRevD.46.381 (1 July 1992).

33. Passarino, G. & Veltman, M. One-loop corrections for e+e− annihilation into $+-$ in the Weinberg model. *Nuclear Physics B* **160,** 151–207. ISSN: 0550-3213. https://www.sciencedirect.com/science/article/pii/0550321379902347 (1979).

34. Haber, H. E. & O'Neil, D. Basis-independent methods for the two-Higgs-doublet model. II. The significance of tan$\beta$. *Phys. Rev. D* **74,** 015018. https://link.aps.org/doi/10.1103/PhysRevD.74.015018 (1 July 2006).

35. Langacker, P. *Precision Tests of the Standard Electroweak Model* eprint: https://www.worldscientific.com/doi/pdf/10.1142/1927. https://www.worldscientific.com/doi/abs/10.1142/1927 (WORLD SCIENTIFIC, 1995).

36. Denner, A. Techniques for calculation of electroweak radiative corrections at the one loop level and results for W physics at LEP-200. *Fortsch. Phys.* **41,** 307–420. arXiv: 0709.1075 [hep-ph] (1993).

37. Han, X.-F. & Wang, H.-X. Revisiting wrong sign Yukawa coupling of type II two-Higgs-doublet model in light of recent LHC data. *Chin. Phys. C* **44,** 073101. arXiv: 2003.06170 [hep-ph] (2020).

38. Bechtle, P. *et al.* HiggsBounds-5: testing Higgs sectors in the LHC 13 TeV Era. *The European Physical Journal C* **80,** 1211. ISSN: 1434-6052. https://doi.org/10.1140/epjc/s10052-020-08557-9 (Dec. 29, 2020).

39. Bhupal Dev, P. S. & Pilaftsis, A. Maximally symmetric two Higgs doublet model with natural standard model alignment. *Journal of High Energy Physics* **2014,** 24. ISSN: 1029-8479. https://doi.org/10.1007/JHEP12(2014)024 (2014).

40. Bernon, J., Gunion, J. F., Haber, H. E., Jiang, Y. & Kraml, S. Scrutinizing the alignment limit in two-Higgs-doublet models: $m_h = 125$ GeV. *Phys. Rev. D* **92,** 075004. https://link.aps.org/doi/10.1103/PhysRevD.92.075004 (7 Oct. 2015).

41. Chen, N., Du, C., Wu, Y. & Xu, X.-J. Further study of the global minimum constraint on the two-Higgs-doublet models: LHC searches for heavy Higgs bosons. *Phys. Rev. D* **99,** 035011. https://link.aps.org/doi/10.1103/PhysRevD.99.035011 (3 Feb. 2019).

42. Gu, J., Li, H., Liu, Z., Su, S. & Su, W. Learning from Higgs physics at future Higgs factories. *Journal of High Energy Physics* **2017,** 153. ISSN: 1029-8479. https://doi.org/10.1007/JHEP12(2017)153 (2017).

43. Palacino, G. Direct searches for additional scalar Higgs at ATLAS and CMS. http://cds.cern.ch/record/2679590 (2019).

44. Grippo, M. Searches for additional Higgs bosons at CMS. *Nuclear and Particle Physics Proceedings* **300-302.** QCD 18 is the 21st International Conference on Quantum Chromodynamics, 61–66. ISSN: 2405-6014. https://www.sciencedirect.com/science/article/pii/S2405601418301949 (2018).

45. Kundu, A., Le Yaouanc, A., Mondal, P. & Richard, F. *Searches for scalars at LHC and interpretation of the findings* in *2022 ECFA Workshop on e+e- Higgs/EW/Top factories* (Nov. 2022). arXiv: 2211.11723 [hep-ph].

46. Andrean, S. Y. *Search for New Scalar Particles with ATLAS* PhD dissertation (Stockholm University, 2023). https://urn.kb.se/resolve?urn=urn:nbn:se:su:diva-214743.

47. Harlander, R. V., Liebler, S. & Mantler, H. SusHi: A program for the calculation of Higgs production in gluon fusion and bottom-quark annihilation in the Standard Model and the MSSM. *Computer Physics Communications* **184,** 1605–1617. ISSN: 0010-4655. https://www.sciencedirect.com/science/article/pii/S0010465513000507 (2013).

48. Eriksson, D., Rathsman, J. & Stål, O. 2HDMC – two-Higgs-doublet model calculator. *Computer Physics Communications* **181,** 189–205. ISSN: 0010-4655. https://www.sciencedirect.com/science/article/pii/S0010465509003014 (2010).

49. Han, X.-F., Wang, L. & Zhang, Y. Dark matter, electroweak phase transition, and gravitational waves in the type II two-Higgs-doublet model with a singlet scalar field. *Phys. Rev. D* **103,** 035012. https://link.aps.org/doi/10.1103/PhysRevD.103.035012 (3 Feb. 2021).

50. Wang, L., Wang, H.-X. & Han, X.-F. Revisiting wrong sign Yukawa coupling of type II two-Higgs-doublet model in light of recent LHC data *. *Chinese Physics C* **44,** 073101. https://dx.doi.org/10.1088/1674-1137/44/7/073101 (July 2020).

51. Abdesselam, A. *et al. Measurement of the inclusive $B \to X_{s+d}\gamma$ branching fraction, photon energy spectrum and HQE parameters* in *38th International Conference on High Energy Physics* (Aug. 2016). arXiv: 1608.02344 [hep-ex].

52. Misiak, M. & Steinhauser, M. Weak radiative decays of the B meson and bounds on $M_{H^\pm}$ in the Two-Higgs-Doublet Model. *Eur. Phys. J. C* **77,** 201. arXiv: 1702.04571 [hep-ph] (2017).

53. Haller, J. *et al.* Update of the global electroweak fit and constraints on two-Higgs-doublet models. *The European Physical Journal C* **78,** 675. ISSN: 1434-6052. https://doi.org/10.1140/epjc/s10052-018-6131-3 (2018).

54. Fuchs, E., Thewes, S. & Weiglein, G. Interference effects in BSM processes with a generalised narrow-width approximation. *The European Physical Journal C* **75,** 254. ISSN: 1434-6052. https://doi.org/10.1140/epjc/s10052-015-3472-z (June 9, 2015).